Controlling the properties of solid-liquid interfaces in silica nanopores via surface functionalization

by

Dilini Singappuli-Arachchige

A dissertation submitted to the graduate faculty

in partial fulfillment of the requirements for the degree of

DOCTOR OF PHILOSOPHY

Major: Chemistry

Program of Study Committee:
Igor I. Slowing, Major Professor
Wenyu Huang
Marek Pruski
Aaron Sadow
Brett VanVeller

The student author, whose presentation of the scholarship herein was approved by the program of study committee, is solely responsible for the content of this dissertation. The Graduate College will ensure this dissertation is globally accessible and will not permit alterations after a degree is conferred.

Iowa State University

Ames, Iowa

2019

TABLE OF CONTENTS

Page

ACKNOWLEDGMENTS

I would like to thank my advisor, Dr. Igor I. Slowing for making me a part of "Slowing Group" and giving me opportunity to involve in very exciting research. Your guidance, patience, encouragements, and criticisms played a big role in shaping me for who I am today. You have always been very supportive to me throughout all these years both inside and outside lab, and during most of my life challenges. I would also like to thank my committee members, Drs. Wenyu Huang, Marek Pruski, Aaron Sadow and Brett Van-Veller for their guidance and support throughout the course of this research.

I would like to thank past and current members of "Slowing Group" for all the support and good times spent together. I kindly remind Umesh Choudhry for helping me getting familiar with both laboratory and teaching work during the time I started at Iowa State University. Special thanks to Dr. Sebastian Manzano, my brother from another mother for all the support, discussions related to science and life, laughs and fights we had continuously for over five years. In addition, I would like to thank Pruski research group and Smith research group for all the support given in collaborative work.

I want to offer my appreciation to my parents, my loving husband Charith and my darling daughter Sanu for always being there for me and understanding me. Without your love and caring, I wouldn't stand here today. I also want to thank my besties, Kasuni, Himashi and Chamari for all the support and good times spent together at Iowa State University.

I would like to thank the U.S. Department of Energy, Office of Basic Energy Sciences, Division of Chemical Sciences, Geosciences, and Biosciences, through the Ames Laboratory Catalysis Science program at the Ames Laboratory under contract number DEAC02-07CH11358.

ABSTRACT

This dissertation explores how functionalization of mesoporous silicas affects their solid-liquid interfacial properties. The research work is focused on carefully modifying pore surfaces of mesoporous silica with organic functional groups to create local environments that differ from the bulk medium. Chapter 1 is a general introduction to mesoporous silica nanoparticles (MSN) and a literature review of previous attempts to modify silica-water interface for different applications.

Chapter 2 describes an effort to control local polarity at silica-water interface via surface functionalization of MSN. A local polarity scale was created using solvatochromic dye Prodan and interfacial polarity values were assigned to functionalized MSN pores. The effects of pore polarity on quenching of Nile Red fluorescence and on the vibronic band structure of pyrene were also studied. The results showed that the dielectric properties in the pores are different from the bulk water. We found that the catalytic activity of TEMPO for the aerobic oxidation of furfuryl alcohol in water improved when decreasing pore polarity. This work demonstrated that the activity of a nanoconfined catalyst can be modified by controlling the local polarity around it.

Chapter 3 further explores the interfacial control of catalytic activity inside the nanometer pores of MSN. The activity of aminopropyl-functionalized mesoporous silica nanoparticles (AP-MSN) for the aldol condensation can be improved by using either a non-polar solvent or an aqueous media. In this work, a novel AP-MSN based catalytic system with combined action of water and low-local polarity environment is presented. Local polarity was tuned by introducing different surface densities of hexyl groups on AP-MSN. The dielectric constants of the hexyl modified silica-water interfaces were determined using the solvatochromic probe Prodan as discussed in Chapter 1. The activity of hexyl-modified AP-MSN in water increased with

decreasing interfacial dielectric constants. In addition, aldol reactions with substituted substrates, and other C-C bond forming reactions such as Henry and Vinylogous aldol catalyzed by hexyl-modified AP-MSN in water were enhanced compared to those catalyzed by AP-MSN in water. An improved performance of AP-MSN for aldol condensation and similar reactions were achieved by combining the effects of hydrophobic environments and water at the catalyst-solvent interface.

Chapter 4 demonstrates how the orientation and mobility of surface groups affects the strength of non-covalent interactions between a guest molecule and the mesoporous silica surface. In this study, we created different phenyl functionalized mesoporous silica samples with different orientations of phenyl groups relative to the pore surface, i.e. rigid perpendicular, variable orientation derived from a flexible ethylene linker, and rigid co-planar. The release of adsorbed Ibuprofen into simulated body fluid from these phenyl-functionalized silicas was analyzed using an adsorption-diffusion model. All phenyl-bearing materials showed lower Ibuprofen initial release rates than bare MSN. The materials with conformationally locked upright and co-planar phenyl groups had stronger interactions with Ibuprofen than those with mobile groups and bare MSN. The obtained results were consistent with DFT calculations. We demonstrated that we could control the kinetics and extent of Ibuprofen release by tuning the type and geometry of non-covalent interactions at the solid-liquid interface.

Chapter 5 introduces an approach for controlling interfacial acid-based properties inside nanopores. We demonstrated that the silica-water interfacial pH of MSN can be tuned by functionalizing the pores with different acids and bases. To probe the interfacial pH, we grafted a modified pH sensitive dual emission fluorescent probe, SNARF-AP on silica surfaces. The fluorescence intensity ratio (I_{588}/I_{635}) of the probe at different bulk pH served as a calibration to

assign pH values for functionalized mesoporous silica-water interfaces. We showed that interfacial pH varied as a function of the surface groups' pK_a and that it was different from the bulk pH. We attributed the differences to altering protonation/deprotonation equilibria on surface and to the interfacial potential that results from the surface charges. We demonstrated that effective screening of surface charges can be achieved by increasing the ionic strength of the solution. In addition, replacing MSN with a wider pore MSN-10 showed a similar effect. Both these factors affect the proton concentration in the vicinity of surface.

CHAPTER 1. GENERAL INTRODUCTION

This thesis summarizes our attempts to study the local properties inside nanometer sized silica pores by modifying their surfaces with different organic groups. By carefully controlling their surface chemistry distinct local environments can be achieved inside the pores, allowing the production of microenvironments with properties that differ from the bulk medium. The ability to control the local properties of the pores can lead to interesting applications in catalysis, adsorption and drug delivery.

Porous materials are classified depending on their pore width as microporous (smaller than 2 nm diameter), mesoporous (2-50 nm) and macroporous (larger than 50 nm), according to International Union of Pure and Applied Chemistry (IUPAC).[1] Microporous zeolite minerals are a class of naturally occurring crystalline materials with ordered pore structures. Both natural and synthetic zeolites have been used as traditional ion exchangers, adsorbents, catalysts, catalyst supports and hosts for molecular encapsulation.[2-5] However, due to microporosity, the applications of zeolites are limited to small molecules. To overcome this limitation, scientists developed mesoporous materials. Following the emergence of mesoporous silica and its wide use, the family of mesoporous structures has expanded to include other oxides and non-oxides, for example mesoporous carbons.[6-14] This thesis will mainly focus on mesoporous silica materials.

Mesoporous silica materials

Kuroda and co-workers and scientists at the Mobile Oil Company pioneered the discovery of ordered mesoporous materials.[15-17] These materials had well-defined cylindrical pores in the range 2-10 nm and could handle molecules that were too large to fit into traditional zeolites. In addition, they possessed large surface areas (700-1500 m^2/g), high chemical and

thermal stability and their surface could be functionalized. Some common mesoporous materials include MCM-41, MCM-48 and MCM-50 with 2D hexagonal, cubic and lamellar structures respectively (Figure 1).

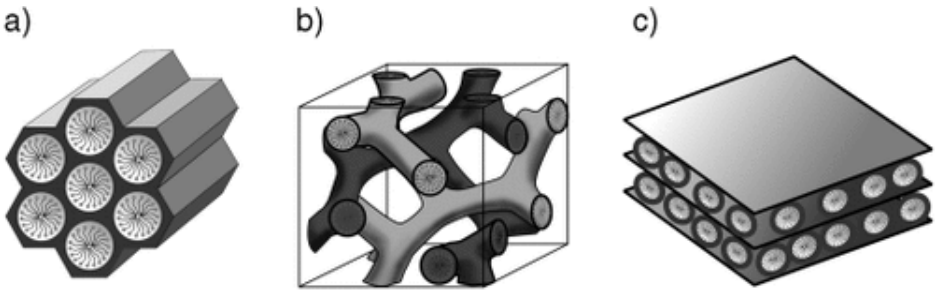

Figure 1. Different structures of ordered mesoporous silica: a) MCM-41 with 2D hexagonal phase, b) MCM-48 with cubic phase, c) MCM-50 with lamellar phase. Reproduced with permission from Ref 7.

Significant research efforts on further controlling pore size and morphology led to appearance of new families of mesoporous silica materials such as SBA[18, 19], MSU[20] and FSM[17] with characteristic porosities and morphologies. For example, SBA-15 silica developed by Stucky and co-workers had a 2D hexagonal array of large uniform pores tunable up to 30 nm.[19] The mesopores of SBA-15 were connected by numerous disordered micropores, in contrast to MCM type mesoporous silicas. Later, our group developed an alternative fast route to MCM-41 that leads to well-defined, uniform nano-sized mesoporous silica nanoparticles (MSN).[21]

A different class of mesostructured materials termed periodic mesoporous organosilicas (PMO) was discovered by three independent research groups in 1999.[17, 22-24] These materials were synthesized by hydrolysis and condensation of bridged organosilane precursors $(R'O)_3Si$-R-$Si(OR')_3$ in presence of a structure directing agent (SDA). Organic groups were incorporated homogeneously within silica walls via two or more covalent bonds. These materials possessed periodically organized pores and narrow pore size distributions.[25] PMO materials have also been

promising candidates in different fields including catalysis, adsorption, drug delivery, chromatography and electronics.[26-28]

Synthesis of mesoporous silica

Ordered mesoporous silicas are synthesized using an SDA, typically a neutral or charged surfactant, in aqueous solution and a silica precursor, typically an ester of orthosilicic acid (e.g.: tetraethylorthosilicate (TEOS), tetramethylorthosilicate (TMOS)). Two different mechanisms have been proposed for the synthesis of mesoporous silica materials, 1. true liquid-crystal template mechanism (TLCT), and 2. cooperative liquid-crystal template mechanism (CLCT) (Figure 2).[16, 29, 30] According to TLCT mechanism, a hexagonal array of SDA is first formed and the condensation of silicate species occurs around them to form the structure.[29] According to CLCT mechanism, silicate species condense on randomly ordered rod like micelles and these composites spontaneously pack into energetically favorable hexagonal arrangement.[16]

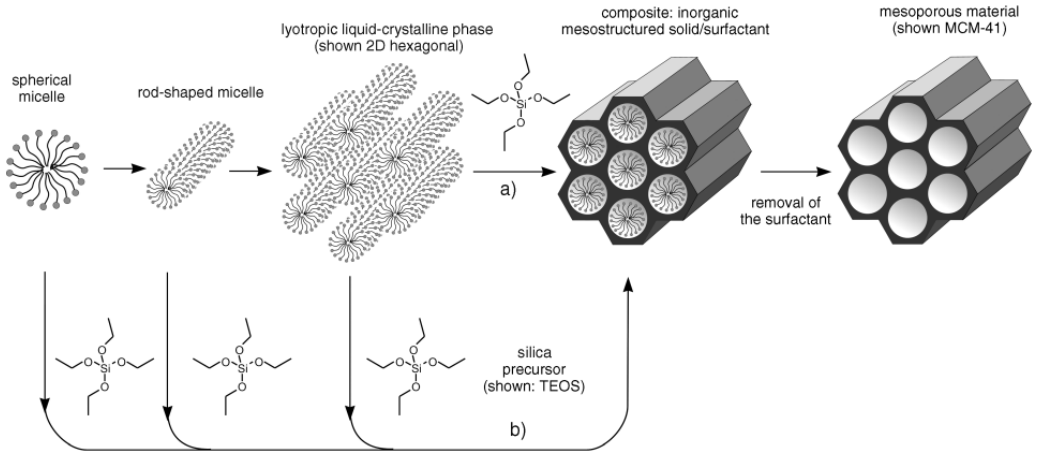

Figure 2. Formation of mesoporous silica materials by different mechanisms: a) TLCT mechanism, b) CLCT mechanism. Reproduced with permission from Ref 7.

The mesostructured SDA-silica transient composites are assembled via different types of interactions between the head groups of the former and the growing silica framework (Figure

3).[7, 31, 32] For example, a) under basic conditions - anionic silica species (I^-) and cationic quaternary ammonium SDA head groups (S^+), b) under acidic conditions – cationic silica species (I^+), mediator ion such as halide (X^-) and cationic SDA (S^+), c) under basic conditions- anionic silica species (I^-), mediator ion (M^+) and anionic long chain alkyl phosphate SDA (S^-), and d) under acidic conditions- cationic silica species (I^+) and anionic long chain alkyl phosphate SDA (S^-) are held together by electrostatic interaction forces. In addition, e) uncharged silica (I^0) and non-ionic SDA (S^0) and f) charged silica-mediator ion pair ($X^- I^+$) and non-ionic SDA (S^0) are held together via H bonds. These interactions ensure that there is no phase separation of SDA in the reaction medium and lead to efficient synthesis of the material of interest.

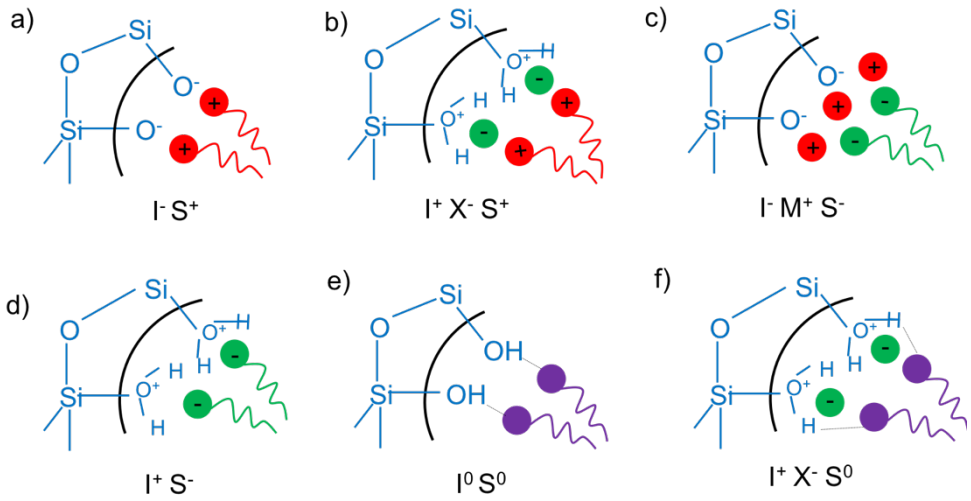

Figure 3. Different types of interactions between inorganic silica framework and head group of SDA.[7]

The particle size and morphology of mesoporous silica materials depend on factors such as reaction temperature, pH, stirring rate, co-solvents and additives.[18, 33, 34] For example, our group has developed several methods to control the morphology, pore size and surface functionalization of MCM-41 type MSN by various adjustments of synthesis conditions.[21, 35-37] It is possible to alter the mesostructure, size and morphology of MSN with a careful control of

hydrolysis and condensation rates of silica. During MSN synthesis, the assembly of the ordered mesophase mainly depends on the interaction between the cationic surfactant cetyltrimethylammonium bromide (CTAB) dissolved in aqueous basic medium and the growing anionic oligomers of tetraethylorthosilicate. The obtained MSN particles are spherical and about 200 nm in size.

Removal of surfactant from the mesostructures after the synthesis is usually performed by either calcination or extraction.[38] Calcination induces further dehydration of surface silanol groups to Si-O-Si bonds and shrinkage of the structures. This method is not suitable for surface functionalized materials. Hot ethanol extraction of non-ionic surfactants, or acid/methanol extraction for cationic surfactants are other alternative methods to remove the template.

Surface functionalization of mesoporous silica

Physical and chemical properties of mesoporous silica can be altered by adding organic groups on the surface. They possess two distinguishable surfaces: 1. internal surface corresponding to the pores and 2. exterior particle surface. Interestingly, it is possible to selectively functionalize either surface with different organic groups.[21, 39] Typically, surface functionalization occurs by binding organosilanes to free silanol groups on silica surface via substitution reactions. There are two methods to functionalize silica surfaces: 1. co-condensation, and 2. post-synthetic grafting.

Co-condensation method is also called “one-pot synthesis”. Tetra-alkoxysilanes (TEOS or TMOS) and tri-alkoxyorganosilanes ($(R'O)_3Si-R$) are reacted in the presence of SDA to obtain mesostructured silica phases.[37, 40] During the templated synthesis the hydrophobic -R groups of tri-alkoxyorganosilanes are believed to intercalate into the hydrophobic region of SDA. This orientation results in the projection of -R groups into the pores.[37] In the final material, organic groups are covalently anchored to the pore walls and become a part of the silica matrix

(Figure 4). Simultaneous anchoring of multiple functional groups on the pore walls of MSN with the ability to tune the relative ratios of different groups of interest is also possible via co-condensation.[41] However, introducing tri-alkoxyorganosilanes can sometimes decrease the degree of mesoscopic order and change the morphology of the material. Generally, the surface functionalization via co-condensation results in uniform distribution of organic groups on surface without blockage of pores.[7, 37]

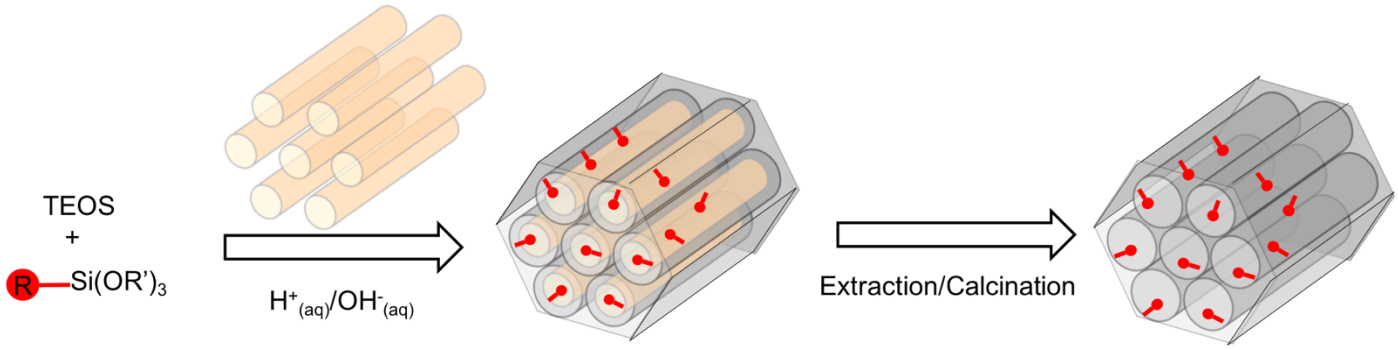

Figure 4. A schematic representation of co-condensation.[7]

Grafting is a post synthetic method. The free silanol groups on the MSN surface are reacted with organoalkoxysilanes $(R'O)_3SiR$, chlorosilanes $ClSiR_3$ or silazanes $HN(SiR_3)_3$ (Figure 5). In this method, the mesostructure of the parent material is retained. However, bulky -R groups and higher degree of functionalization can lead to reduction in pore size and pore blocking. Some studies have suggested that depending on reaction conditions organosilanes can react preferentially at the pore openings or on the external surface leading to inhomogeneous functionalization of pore walls and low grafting efficiency,[37, 42] however other researchers have shown that careful grafting can lead to a homogeneous distribution of organic groups.[43-45]

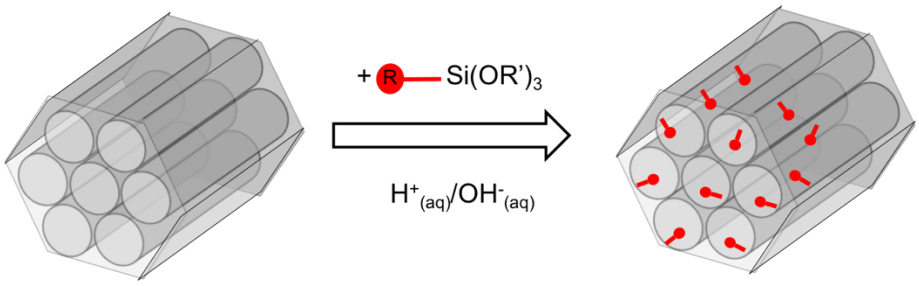

Figure 5. A schematic representation of grafting.[7]

Effects of surface functionalities on the properties of mesoporous silica-water interfaces

Mesoporous silica materials are of great interest in different applications including catalysis, sensors, encapsulation, adsorption, separation, controlled release, and electrochemistry.[25, 46-49] Most of these processes involve water as a solvent and this leads to interesting chemistry happening inside water-filled silica pores. It has been shown that inside pores narrower than ~20 nm, the properties of water are different from bulk water due to confinement effects.[50] Importantly for pores in the range 2-20 nm, where most of the mesoporous materials fall, two regimes of water are proposed: an approximately 0.9 nm layer of water on the pore surface with structural and dynamic properties different from bulk water, and a free bulk-like core of water in the rest of the pore volume.[51, 52] The surface water layer is approximately three monolayers of water and it is believed that it is ordered and less mobile than the rest of the water inside pore.[53, 54] We define the silica-water interface as the region including the silica surface and the ordered layers of water in contact with the surface.[50]

Controlling the properties of the silica-water interface is crucial to maximize performance in most of the applications of mesoporous silicas. Surface functionalization plays an important role in controlling interfacial properties. It decreases the effective pore size, modifies chemical interactions between the surface and adsorbed molecules and alters the wettability by aqueous solutions. This thesis is focused on developing methods to control and characterize the dielectric

properties, acid-base equilibria, and non-covalent interactions at the mesoporous silica-water interface.

Controlling the polarity of mesoporous silica-water interfaces

The polarity at the mesoporous silica-water interface can be adjusted to improve their performances in different applications. For example, cyclodextrin modified mesoporous silica was used as adsorbent for the selective separation of aromatic molecules from water by Bibby *et al*.[55] Hydrophobic cavities of MCM-41 silicas were used to encapsulate a chromofluorogenic probe for selective detection of sulfite.[56] In addition, the performance of silica-based drug delivery systems has been optimized by controlling the hydrophobicity of silica surfaces.[57-59] The hydrocarbon chains on the pore surface strengthened the interactions between the matrix and adsorbed molecules, thereby altering the release rate of loaded drugs. Otsuka *et al*. suggested that the interactions between phytonadione, an oily medicine and silica surface improves by modification of silica matrix with hydrocarbon chains.[57] Kortesuo *et al*. showed that the surface hydrophobicity decreases the degradation rate of silica, which in turn affects the release of dexmedetomidine.[58] Vallet-Regi *et al*. showed the release rates of erythromycin can be controlled using SBA-15 type mesoporous silica functionalized with octadecyl (C_{18}) groups.[59] In this study, the surface wettability was determined by measuring the adsorbed water using thermogravimetric analysis. It was used as a measure of relative hydrophobicity of the material.

The interfacial polarity can be adjusted to improve the activity or selectivity in heterogeneously catalyzed reactions. This approach has been of great interest specifically to perform organic reactions in environmentally friendly, non-toxic and less expensive aqueous solvents. Neumann *et al.* used hydrophobic phenyl functionalized silica surfaces to improve olefin epoxidation in aqueous hydrogen peroxide to avoid use of organic solvents.[60] In a different study, they developed a silica surface with covalently attached polyethers that acted as

solvating or complexing agents for a polyoxometalate alkene oxidation catalyst.[61] The authors suggested that the hydrophilic-hydrophobic balance of the surface must be adjusted to optimize the solubility of organic and aqueous phase reactants. In a related study, a biomimetic, methane monooxygenase enzyme precatalyst was embedded in a silica surface with anchored hydrophilic poly(ethyleneoxide) and hydrophobic poly(propyleneoxide) groups for oxidative activation of C-H bonds of cyclohexane in water.[62] The authors claimed that the balance between hydrophobic and hydrophilic groups on the surface was crucial for maximizing the catalytic activity. Pac *et al.* used a chemically modified hydrophobic mesoporous silica surface to fix tungstophosphate anion and catalyze the selective epoxidation of various alkenes in aqueous hydrogen peroxide, and achieved increased efficiency of the reaction compared to non-functionalized material.[63] A palladium catalyst supported on hydrophilic polyethylene glycol modified SBA-15 type mesoporous silica was prepared by Xiong and co-workers for efficient Suzuki-Miyaura coupling reactions in water.[64] Alizadeh *et al.* obtained good yields in Mannich reaction of different aromatic compounds in water using a hydrophobic, sulfonic acid based SBA-15 type silica.[65] Yang *et al.* encapsulated lipase in silica functionalized with hydrophilic or hydrophobic long chain polymers and found that the lipase entrapped in moderate hydrophobic microenvironments within silica nanochannels had the optimum catalytic activity.[66] In this study, water and benzene adsorption experiments, along with lysozyme adsorption experiments were used to determine the surface hydrophobicity/hydrophilicity. Karimi *et al.* showed that SBA-15 silica functionalized with octyl groups enhanced the selectivity of tungstate catalysts in sulfide oxidation in water (Figure 6).[67] This work nicely demonstrated the influence of hydrophobic/hydrophilic balance in a reaction system (substrate, catalyst and solvent) on the selectivity patterns.

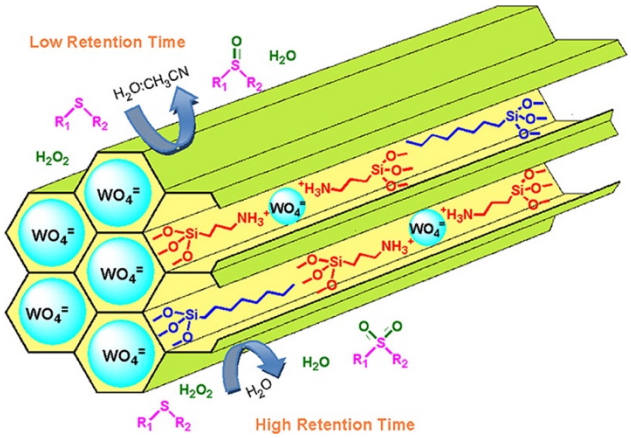

Figure 6. A schematic representation of selective oxidation sulfides to sulfoxides and sulfones in a heterogeneous catalytic system of tungstate immobilized on hydrophobic SBA-15. Reproduced with permission from Ref 67.

In addition, the intrinsic hydrophobicity of PMO due to alkyl bridged structure has been exploited in different applications.[68, 69] Selective adsorption of haloaryls from aqueous solutions was achieved by hydrophobic phenyl modified PMO materials to improve catalytic activity of Ulmann coupling reactions in water by Wan and co-workers.[68] Surface hydrophobicity of the material was evaluated by adsorption isotherms of water and toluene. Kapoor *et al.* demonstrated excellent activity in Friedel-Crafts acylation reactions catalyzed by phenylene bridged mesoporous silica functionalized with sulfonic acid groups.[69]

Despite the importance of hydrophobic/hydrophilic balance on silica surface, little attention has been given to tune and quantify the surface polarity. An effective method for quantification of interfacial polarity of mesoporous silica is reported in Chapter 2 of this thesis. This novel approach is used to design materials with targeted interfacial polarity values. A direct relationship between the interfacial polarity and conversion of organic reactions performed in water is demonstrated.

Chapter 3 presents a design of an effective catalytic system based on amine functionalized silica for aldol type C-C bond forming reactions. The optimum activity is achieved by combining a catalyst surface with low dielectric constant that also allows access of water molecules to the interface. Controlling the interfacial dielectric constant of a catalyst's environment while in water maximizes its activity for this type of conversion.

Controlling non-covalent interactions at the mesoporous silica-water interface

Non-covalent interactions can occur between surface and guest molecules at bare and functionalized silica-water interfaces, and can be employed to facilitate different processes. For example, there are several reports of mesoporous silica based drug delivery systems that utilize different types of non-covalent interactions for controlled activity.[70-72] Vallet-Regi *et al.* reported that coulombic interactions between protonated amine groups on silica surface and carboxylate groups of ibuprofen contributed to lower the drug's release rates.[70] In a computational study of MCM-41 silica based drug delivery system, Ugliengo *et al.* found that London dispersion forces outweigh the H bonding interactions in the adsorption of Ibuprofen to the silica surface.[71, 72] π-π stacking interactions between aromatic guest molecules and aromatic surface functionalities have also been utilized in different applications. Hao *et al.* used a large pore phenyl-bridged PMO for efficient adsorption of benzene vapor via π-π stacking interactions.[73] Sarkar *et al.* immobilized a series of fluorophores onto functionalized MCM-41 type silica materials and used them for the detection of nitroaromatic explosives (Figure 7).[74] A significant quenching of fluorescence signal, in the presence of nitroaromatics was ascribed to π-π stacking interactions between electron-rich fluorophores and electron deficient nitroaromatics.

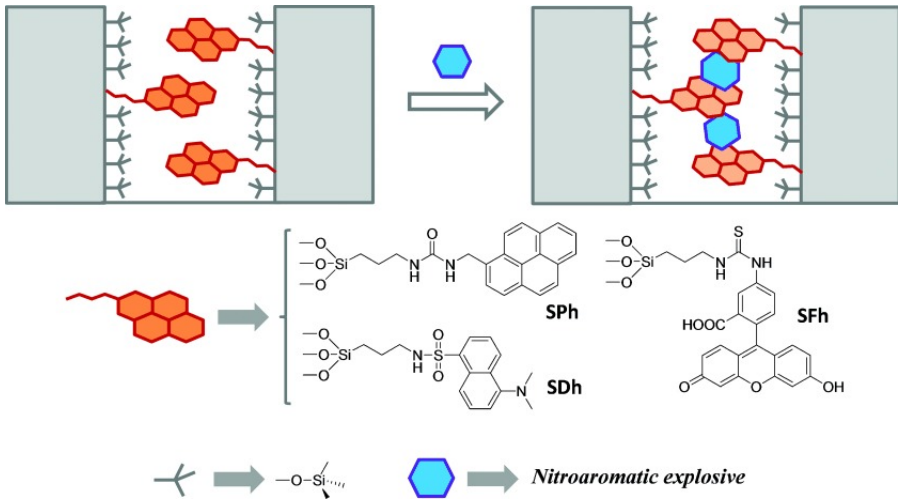

Figure 7. A schematic representation of the π-π stacking sensing protocol between functionalized silica surfaces and nitro aromatics. Reproduced with permission from Ref 74.

Although the importance of non-covalent interactions has been highlighted in previous research, little attention has been paid to the role that the relative position and geometry of the functional groups play on the intensity of these interactions. Chapter 4 of this thesis describes the dependence of π-π interactions between adsorbed guest molecules and functionalized silica surfaces on the orientation and mobility of surface phenyl groups.

Controlling acid-base equilibria at mesoporous silica-water interface

Surface silanol groups play an important role in acid-base reactions at the silica-water interface. Ong *et al.* used second harmonic generation measurements to probe the silica-water interface and reported two types of silanols with different pK_a values.[75] The bimodal distribution of silanols was attributed to different solvation or hydrogen-bonding environments.[76-80] Darligton *et al.* also used second harmonic generation measurements to determine how the starting pH affects the acid-base properties of silica-water interface during titration of silanols.[81] However, they identified three distinct pK_a values at the silica-water interface, and attributed those to silanols in different hydrogen bonding environments, i.e. non hydrogen bonded isolated silanols

(pK_a 3.8), silanols hydrogen bonding with water (pK_a 5.2), and silanols hydrogen bonding with neighbouring silanols (pK_a 9). Rosenholm *et al.* studied the Bronsted acidity of non-functionalized and carboxylic acid functionalized SBA-15 silica by measuring the adsorption isotherms of benzylamine.[82] They demonstrated that geminal silanols largely control the interfacial chemistry of SBA-15 silica in basic aqueous solutions.

The acid-base properties of mesoporous silica have been tailored for different applications. For example, Fattakhova-Rohlfing *et al.* functionalized a thin mesoporous silica layer with amino groups for use as an ion selective separation membrane.[83] By changing the solution pH they were able to control the selectivity and permeability of the membrane to anions, cations and neutral molecules. Zheng *et al.* designed a controllable pH responsive drug delivery system based on electrostatic attraction between negatively charged silanol groups on an ultra-small MSN surface and positively charged drug molecules.[84] Berger and co-workers found a correlation between the pK_a of surface functional groups and the amount of drug released from a mesoporous silica-based system.[85] In addition, Fujita and co-workers reported that the proton conductivity inside the pores of sulfonic acid functionalized mesoporous silica was controlled by pore sizes and acid densities.[86] Gao *et al.* showed that the adsorption of acidic and basic amino acids on SBA-15 type functionalized mesoporous silica depends strongly on pH and surface charge of silica.[87] These and other studies show that by altering the surface charge on silica, the silica-water interface can be adapted for different purposes.

According to the Gouy-Chapman-Stern model, the charged silica surface attracts counterions from the solvent to form a diffuse layer, which results in a surface potential.[88] If the attracted counter ions are protons, there will be an elevated proton concentration at the silica-water interface leading to a local or interfacial pH, which may be different from the bulk pH.

Sen *et al.* analyzed the surface charge of mesoporous silica at different pore sizes, porosities and salt concentrations. They developed a model to predict the average surface charge as a function of pore size, porosity and electric double layer thickness.[89] Several groups have studied the interfacial potential of silica-based systems. For example, Kovaleva *et al.* used pH sensitive nitroxide radicals (NR) as EPR probes to study the potential at hydrated silica surfaces.[90-92] Fast and slow diffusion populations of the probe were assigned to NR inside the channels and at interfaces respectively. The non-protonated fraction of the slow NR was used as the pH sensitive parameter in a model that allowed estimating the local acidity near the surface and the interfacial potential.[90] In a related study, they found that in the channels of mesoporous silica with larger pores such as SBA-15 (8.1 nm), the mobile NR probe is insensitive to surface charges because of the effective screening of surface charges by counter ions, whereas in smaller channels with radii comparable to the Debye length such as MCM-41 (3.2 nm), the probe is sensitive to protonation of surface groups. They suggested that, at basic pH the large negative surface potential developed on MCM-41 silica surface cannot be effectively screened by counter ions, thus it affects the proton activity near surface.[91] Valetti *et al.* proposed a model to predict the charging behavior of mesoporous silica surface as a function of pH and ionic strength.[93] They suggested that the pore surfaces are negatively charged and the rest of the pore volume is filled with counter ions to neutralize the charges at moderate to high pH. These studies suggest that by adjusting the surface charge through surface functionalization, pH dependent processes such as sorption and catalysis can be controlled.

Several groups have attempted to measure the pH at silica-water interface. Shenderovich *et al.* used Pyridine-^{15}N as a mobile NMR sensor for surface acidity in mesoporous silica.[94] They studied the proton donating power of surface silanols and geometry of silanol-pyridine H-bonds

in MCM-41 and SBA-15 type mesoporous silicas. Teramae and co-workers studied the interfacial pH inside a mesoporous silica densely functionalized with amine groups via entrapped fluorescence pH indicator dyes.[95] This study showed that the pH inside the pores and the pH in the bulk have a non-linear relationship and that large changes in bulk pH induce only small changes in pore pH. Olsson and co-workers designed a method to measure pH inside SBA-15 type mesoporous silica particles using a protein-bound fluorescent probe, SNARF-1.[96] They showed that when the protein-dye conjugate was introduced into the material the pH inside the pores was close to 7 regardless of the solution pH, which suggested that the pores contained a buffering agent.

All of these studies suggest that the pH at the mesoporous silica-water interface is different from the bulk pH. However, a systematic study to tune the interfacial pH is still lacking. Chapter 5 of this thesis describes a system to measure and adjust the pH of the mesoporous silica-water interface at values different from the bulk pH. This capability can lead to potential applications in protecting enzymes and chemical species from sudden changes in the pH of the medium.

References

1. Sing, K. S. W., Reporting physisorption data for gas/solid systems with special reference to the determination of surface area and porosity (Recommendations 1984). In *Pure and Applied Chemistry*, 1985; Vol. 57, p 603.

2. Larsen, S. C., Nanocrystalline Zeolites and Zeolite Structures: Synthesis, Characterization, and Applications. *The Journal of Physical Chemistry C* **2007,** *111* (50), 18464-18474.

3. Young, G. W.; Kiovsky, J. R.; Koradia, P. B., Liquid Phase Drying Applications of Zeolites. In *Adsorption and Ion Exchange with Synthetic Zeolites*, AMERICAN CHEMICAL SOCIETY: 1980; Vol. 135, pp 201-219.

4. Song, W.; Li, G.; Grassian, V. H.; Larsen, S. C., Development of Improved Materials for Environmental Applications: Nanocrystalline NaY Zeolites. *Environmental Science & Technology* **2005,** *39* (5), 1214-1220.

5. Jensen, N. K.; Rufford, T. E.; Watson, G.; Zhang, D. K.; Chan, K. I.; May, E. F., Screening Zeolites for Gas Separation Applications Involving Methane, Nitrogen, and Carbon Dioxide. *Journal of Chemical & Engineering Data* **2012,** *57* (1), 106-113.

6. Schüth, F., Non-siliceous Mesostructured and Mesoporous Materials. *Chemistry of Materials* **2001,** *13* (10), 3184-3195.

7. Hoffmann, F.; Cornelius, M.; Morell, J.; Fröba, M., Silica-Based Mesoporous Organic–Inorganic Hybrid Materials. *Angewandte Chemie International Edition* **2006,** *45* (20), 3216-3251.

8. Sayari, A.; Hamoudi, S., Periodic Mesoporous Silica-Based Organic−Inorganic Nanocomposite Materials. *Chemistry of Materials* **2001,** *13* (10), 3151-3168.

9. Kondo, J. N.; Domen, K., Crystallization of Mesoporous Metal Oxides. *Chemistry of Materials* **2008,** *20* (3), 835-847.

10. Benzigar, M. R.; Talapaneni, S. N.; Joseph, S.; Ramadass, K.; Singh, G.; Scaranto, J.; Ravon, U.; Al-Bahily, K.; Vinu, A., Recent advances in functionalized micro and mesoporous carbon materials: synthesis and applications. *Chemical Society Reviews* **2018,** *47* (8), 2680-2721.

11. Eftekhari, A.; Fan, Z., Ordered mesoporous carbon and its applications for electrochemical energy storage and conversion. *Materials Chemistry Frontiers* **2017,** *1* (6), 1001-1027.

12. Liang, C.; Li, Z.; Dai, S., Mesoporous Carbon Materials: Synthesis and Modification. *Angewandte Chemie International Edition* **2008,** *47* (20), 3696-3717.

13. Slowing, I. I.; Vivero-Escoto, J. L.; Trewyn, B. G.; Lin, V. S.-Y., Mesoporous silica nanoparticles: structural design and applications. *Journal of Materials Chemistry* **2010,** *20* (37), 7924 - 7937.

14. Trewyn, B. G.; Slowing, I. I.; Giri, S.; Chen, H.-T.; Lin, V. S. Y., Synthesis and Functionalization of a Mesoporous Silica Nanoparticle Based on the Sol–Gel Process and Applications in Controlled Release. *Accounts of Chemical Research* **2007,** *40* (9), 846-853.

15. Kresge, C. T.; Leonowicz, M. E.; Roth, W. J.; Vartuli, J. C.; Beck, J. S., Ordered mesoporous molecular sieves synthesized by a liquid-crystal template mechanism. *Nature* **1992,** *359* (6397), 710-712.

16. Beck, J. S.; Vartuli, J. C.; Roth, W. J.; Leonowicz, M. E.; Kresge, C. T.; Schmitt, K. D.; Chu, C. T. W.; Olson, D. H.; Sheppard, E. W.; McCullen, S. B.; Higgins, J. B.; Schlenker, J. L., A new family of mesoporous molecular sieves prepared with liquid crystal templates. *Journal of the American Chemical Society* **1992,** *114* (27), 10834-10843.

17. Inagaki, S.; Fukushima, Y.; Kuroda, K., Synthesis of highly ordered mesoporous materials from a layered polysilicate. *Journal of the Chemical Society, Chemical Communications* **1993,** (8), 680-682.

18. Huo, Q.; Margolese, D. I.; Stucky, G. D., Surfactant Control of Phases in the Synthesis of Mesoporous Silica-Based Materials. *Chemistry of Materials* **1996,** *8* (5), 1147-1160.

19. Zhao, D.; Feng, J.; Huo, Q.; Melosh, N.; Fredrickson, G. H.; Chmelka, B. F.; Stucky, G. D., Triblock Copolymer Syntheses of Mesoporous Silica with Periodic 50 to 300 Angstrom Pores. *Science* **1998,** *279* (5350), 548.

20. Bagshaw, S. A.; Prouzet, E.; Pinnavaia, T. J., Templating of Mesoporous Molecular Sieves by Nonionic Polyethylene Oxide Surfactants. *Science* **1995,** *269* (5228), 1242.

21. Radu, D. R.; Lai, C.-Y.; Jeftinija, K.; Rowe, E. W.; Jeftinija, S.; Lin, V. S. Y., A Polyamidoamine Dendrimer-Capped Mesoporous Silica Nanosphere-Based Gene Transfection Reagent. *Journal of the American Chemical Society* **2004,** *126* (41), 13216-13217.

22. Melde, B. J.; Holland, B. T.; Blanford, C. F.; Stein, A., Mesoporous Sieves with Unified Hybrid Inorganic/Organic Frameworks. *Chemistry of Materials* **1999,** *11* (11), 3302-3308.

23. Asefa, T.; MacLachlan, M. J.; Coombs, N.; Ozin, G. A., Periodic mesoporous organosilicas with organic groups inside the channel walls. *Nature* **1999,** *402* (6764), 867-871.

24. Inagaki, S.; Guan, S.; Fukushima, Y.; Ohsuna, T.; Terasaki, O., Novel Mesoporous Materials with a Uniform Distribution of Organic Groups and Inorganic Oxide in Their Frameworks. *Journal of the American Chemical Society* **1999,** *121* (41), 9611-9614.

25. Loy, D. A.; Shea, K. J., Bridged Polysilsesquioxanes. Highly Porous Hybrid Organic-Inorganic Materials. *Chemical Reviews* **1995,** *95* (5), 1431-1442.

26. Van Der Voort, P.; Esquivel, D.; De Canck, E.; Goethals, F.; Van Driessche, I.; Romero-Salguero, F. J., Periodic Mesoporous Organosilicas: from simple to complex bridges; a comprehensive overview of functions, morphologies and applications. *Chemical Society Reviews* **2013,** *42* (9), 3913-3955.

27. Hatton, B.; Landskron, K.; Whitnall, W.; Perovic, D.; Ozin, G. A., Past, Present, and Future of Periodic Mesoporous OrganosilicasThe PMOs. *Accounts of Chemical Research* **2005,** *38* (4), 305-312.

28. Mizoshita, N.; Tani, T.; Inagaki, S., Syntheses, properties and applications of periodic mesoporous organosilicas prepared from bridged organosilane precursors. *Chemical Society Reviews* **2011,** *40* (2), 789-800.

29. Attard, G. S.; Glyde, J. C.; Göltner, C. G., Liquid-crystalline phases as templates for the synthesis of mesoporous silica. *Nature* **1995,** *378* (6555), 366-368.

30. Chen, C.-Y.; Burkett, S. L.; Li, H.-X.; Davis, M. E., Studies on mesoporous materials II. Synthesis mechanism of MCM-41. *Microporous Materials* **1993,** *2* (1), 27-34.

31. Huo, Q.; Margolese, D. I.; Ciesla, U.; Feng, P.; Gier, T. E.; Sieger, P.; Leon, R.; Petroff, P. M.; Schüth, F.; Stucky, G. D., Generalized synthesis of periodic surfactant/inorganic composite materials. *Nature* **1994,** *368* (6469), 317-321.

32. Huo, Q.; Margolese, D. I.; Ciesla, U.; Demuth, D. G.; Feng, P.; Gier, T. E.; Sieger, P.; Firouzi, A.; Chmelka, B. F., Organization of Organic Molecules with Inorganic Molecular Species into Nanocomposite Biphase Arrays. *Chemistry of Materials* **1994,** *6* (8), 1176-1191.

33. Monnier, A.; Schüth, F.; Huo, Q.; Kumar, D.; Margolese, D.; Maxwell, R. S.; Stucky, G. D.; Krishnamurty, M.; Petroff, P.; Firouzi, A.; Janicke, M.; Chmelka, B. F., Cooperative Formation of Inorganic-Organic Interfaces in the Synthesis of Silicate Mesostructures. *Science* **1993,** *261* (5126), 1299.

34. Zhao, D.; Sun, J.; Li, Q.; Stucky, G. D., Morphological Control of Highly Ordered Mesoporous Silica SBA-15. *Chemistry of Materials* **2000,** *12* (2), 275-279.

35. Lai, C.-Y.; Trewyn, B. G.; Jeftinija, D. M.; Jeftinija, K.; Xu, S.; Jeftinija, S.; Lin, V. S. Y., A Mesoporous Silica Nanosphere-Based Carrier System with Chemically Removable CdS Nanoparticle Caps for Stimuli-Responsive Controlled Release of Neurotransmitters and Drug Molecules. *Journal of the American Chemical Society* **2003,** *125* (15), 4451-4459.

36. Slowing, I. I.; Vivero-Escoto, J. L.; Wu, C.-W.; Lin, V. S. Y., Mesoporous silica nanoparticles as controlled release drug delivery and gene transfection carriers. *Advanced Drug Delivery Reviews* **2008,** *60* (11), 1278-1288.

37. Huh, S.; Wiench, J. W.; Yoo, J.-C.; Pruski, M.; Lin, V. S. Y., Organic Functionalization and Morphology Control of Mesoporous Silicas via a Co-Condensation Synthesis Method. *Chemistry of Materials* **2003,** *15* (22), 4247-4256.

38. Wu, S.-H.; Mou, C.-Y.; Lin, H.-P., Synthesis of mesoporous silica nanoparticles. *Chemical Society Reviews* **2013,** *42* (9), 3862-3875.

39. de Juan, F.; Ruiz-Hitzky, E., Selective Functionalization of Mesoporous Silica. *Advanced Materials* **2000,** *12* (6), 430-432.

40. Burkett, S. L.; Sims, S. D.; Mann, S., Synthesis of hybrid inorganic–organic mesoporous silica by co-condensation of siloxane and organosiloxane precursors. *Chemical Communications* **1996,** (11), 1367-1368.

41. Huh, S.; Wiench, J. W.; Trewyn, B. G.; Song, S.; Pruski, M.; Lin, V. S. Y., Tuning of particle morphology and pore properties in mesoporous silicas with multiple organic functional groups. *Chemical Communications* **2003,** (18), 2364-2365.

42. Lim, M. H.; Stein, A., Comparative Studies of Grafting and Direct Syntheses of Inorganic−Organic Hybrid Mesoporous Materials. *Chemistry of Materials* **1999,** *11* (11), 3285-3295.

43. Kobayashi, T.; Singappuli-Arachchige, D.; Wang, Z.; Slowing, I. I.; Pruski, M., Spatial distribution of organic functional groups supported on mesoporous silica nanoparticles: a study by conventional and DNP-enhanced 29Si solid-state NMR. *Physical Chemistry Chemical Physics* **2017,** *19* (3), 1781-1789.

44. Iliade, P.; Miletto, I.; Coluccia, S.; Berlier, G., Functionalization of mesoporous MCM-41 with aminopropyl groups by co-condensation and grafting: a physico-chemical characterization. *Research on Chemical Intermediates* **2012,** *38* (3), 785-794.

45. Rosenholm, J. M.; Lindén, M., Wet-Chemical Analysis of Surface Concentration of Accessible Groups on Different Amino-Functionalized Mesoporous SBA-15 Silicas. *Chemistry of Materials* **2007,** *19* (20), 5023-5034.

46. Prieto, G.; Tüysüz, H.; Duyckaerts, N.; Knossalla, J.; Wang, G.-H.; Schüth, F., Hollow Nano- and Microstructures as Catalysts. *Chemical Reviews* **2016,** *116* (22), 14056-14119.

47. Wu, D.; Xu, F.; Sun, B.; Fu, R.; He, H.; Matyjaszewski, K., Design and Preparation of Porous Polymers. *Chemical Reviews* **2012,** *112* (7), 3959-4015.

48. Lee, W.; Park, S.-J., Porous Anodic Aluminum Oxide: Anodization and Templated Synthesis of Functional Nanostructures. *Chemical Reviews* **2014,** *114* (15), 7487-7556.

49. Valtchev, V.; Tosheva, L., Porous Nanosized Particles: Preparation, Properties, and Applications. *Chemical Reviews* **2013,** *113* (8), 6734-6760.

50. Bourg, I. C.; Steefel, C. I., Molecular Dynamics Simulations of Water Structure and Diffusion in Silica Nanopores. *The Journal of Physical Chemistry C* **2012,** *116* (21), 11556-11564.

51. Bourg, I. C.; Sposito, G., Molecular dynamics simulations of the electrical double layer on smectite surfaces contacting concentrated mixed electrolyte (NaCl–CaCl2) solutions. *Journal of Colloid and Interface Science* **2011,** *360* (2), 701-715.

52. Kerisit, S.; Liu, C., Molecular Simulations of Water and Ion Diffusion in Nanosized Mineral Fractures. *Environmental Science & Technology* **2009,** *43* (3), 777-782.

53. Mancinelli, R.; Bruni, F.; Ricci, M. A., Structural studies of confined liquids: The case of water confined in MCM-41. *Journal of Molecular Liquids* **2011,** *159* (1), 42-46.

54. Lerbret, A.; Lelong, G.; Mason, P. E.; Saboungi, M.-L.; Brady, J. W., Water Confined in Cylindrical Pores: A Molecular Dynamics Study. *Food biophysics* **2011,** *6* (2), 233-240.

55. Bibby, A.; Mercier, L., Adsorption and separation of water-soluble aromatic molecules by cyclodextrin-functionalized mesoporous silica. *Green Chemistry* **2003,** *5* (1), 15-19.

56. Santos-Figueroa, L. E.; Giménez, C.; Agostini, A.; Aznar, E.; Marcos, M. D.; Sancenón, F.; Martínez-Máñez, R.; Amorós, P., Selective and Sensitive Chromofluorogenic Detection of the Sulfite Anion in Water Using Hydrophobic Hybrid Organic–Inorganic Silica Nanoparticles. *Angewandte Chemie International Edition* **2013,** *52* (51), 13712-13716.

57. Otsuka, M.; Tokumitsu, K.; Matsuda, Y., Solid dosage form preparations from oily medicines and their drug release. Effect of degree of surface-modification of silica gel on the drug release from phytonadione-loaded silica gels. *Journal of Controlled Release* **2000,** *67* (2), 369-384.

58. Kortesuo, P.; Ahola, M.; Kangas, M.; Leino, T.; Laakso, S.; Vuorilehto, L.; Yli-Urpo, A.; Kiesvaara, J.; Marvola, M., Alkyl-substituted silica gel as a carrier in the controlled release of dexmedetomidine. *Journal of Controlled Release* **2001,** *76* (3), 227-238.

59. Doadrio, J. C.; Sousa, E. M. B.; Izquierdo-Barba, I.; Doadrio, A. L.; Perez-Pariente, J.; Vallet-Regi, M., Functionalization of mesoporous materials with long alkyl chains as a strategy for controlling drug delivery pattern. *Journal of Materials Chemistry* **2006,** *16* (5), 462-466.

60. Neumann, R.; Miller, H., Alkene oxidation in water using hydrophobic silica particles derivatized with polyoxometalates as catalysts. *Journal of the Chemical Society, Chemical Communications* **1995,** (22), 2277-2278.

61. Neumann, R.; Cohen, M., Solvent-Anchored Supported Liquid Phase Catalysis: Polyoxometalate-Catalyzed Oxidations. *Angewandte Chemie International Edition in English* **1997,** *36* (16), 1738-1740.

62. Neimann, K.; Neumann, R.; Rabion, A.; Buchanan, R. M.; Fish, R. H., Biomimetic Oxidation Studies. 11. Alkane Functionalization in Aqueous Solution Utilizing in Situ Formed [Fe2O(η1-H2O)(η1-OAc)(TPA)2]3+, as an MMO Model Precatalyst, Embedded in Surface-Derivatized Silica and Contained in Micelles. *Inorganic Chemistry* **1999,** *38* (15), 3575-3580.

63. Sakamoto, T.; Pac, C., Selective epoxidation of olefins by hydrogen peroxide in water using a polyoxometalate catalyst supported on chemically modified hydrophobic mesoporous silica gel. *Tetrahedron Letters* **2000,** *41* (51), 10009-10012.

64. Yang, Q.; Ma, S.; Li, J.; Xiao, F.; Xiong, H., A water-compatible, highly active and reusable PEG-coated mesoporous silica-supported palladium complex and its application in Suzuki coupling reactions. *Chemical Communications* **2006,** (23), 2495-2497.

65. Zareyee, D.; Alizadeh, H., One-pot three-component Mannich reaction in water catalyzed by eco-friendly, hydrophobic and recyclable sulfonic acid based nanosilica (SBA-15-Ph-PrSO3H). *RSC Advances* **2014,** *4* (71), 37941-37946.

66. Liu, J.; Bai, S. Y.; Jin, Q. R.; Zhong, H.; Li, C.; Yang, Q. H., Improved Catalytic Performance of Lipase Accommodated in the Mesoporous Silicas with Polymer-Modified Microenvironment. *Langmuir* **2012,** *28* (25), 9788-9796.

67. Karimi, B.; Khorasani, M., Selectivity Adjustment of SBA-15 Based Tungstate Catalyst in Oxidation of Sulfides by Incorporating a Hydrophobic Organic Group inside the Mesochannels. *Acs Catalysis* **2013,** *3* (7), 1657-1664.

68. Wan, Y.; Chen, J.; Zhang, D.; Li, H., Ullmann coupling reaction in aqueous conditions over the Ph-MCM-41 supported Pd catalyst. *Journal of Molecular Catalysis A: Chemical* **2006,** *258* (1), 89-94.

69. Kapoor, M. P.; Kasama, Y.; Yanagi, M.; Yokoyama, T.; Inagaki, S.; Shimada, T.; Nanbu, H.; Juneja, L. R., Cubic phenylene bridged mesoporous hybrids from allylorganosilane precursors and their applications in Friedel–Crafts acylation reaction. *Microporous and Mesoporous Materials* **2007,** *101* (1), 231-239.

70. Muñoz, B.; Rámila, A.; Pérez-Pariente, J.; Díaz, I.; Vallet-Regí, M., MCM-41 Organic Modification as Drug Delivery Rate Regulator. *Chemistry of Materials* **2003,** *15* (2), 500-503.

71. Delle Piane, M.; Vaccari, S.; Corno, M.; Ugliengo, P., Silica-Based Materials as Drug Adsorbents: First Principle Investigation on the Role of Water Microsolvation on Ibuprofen Adsorption. *The Journal of Physical Chemistry A* **2014,** *118* (31), 5801-5807.

72. Delle Piane, M.; Corno, M.; Pedone, A.; Dovesi, R.; Ugliengo, P., Large-Scale B3LYP Simulations of Ibuprofen Adsorbed in MCM-41 Mesoporous Silica as Drug Delivery System. *The Journal of Physical Chemistry C* **2014,** *118* (46), 26737-26749.

73. Hao, N.; Yang, Y.; Wang, H.; Webley, P. A.; Zhao, D., Synthesis of large-pore phenyl-bridged mesoporous organosilica with thick walls by evaporation-induced self-assembly for efficient benzene adsorption. *Journal of Colloid and Interface Science* **2010,** *346* (2), 429-435.

74. Sarkar, K.; Salinas, Y.; Campos, I.; Martínez-Máñez, R.; Marcos, M. D.; Sancenón, F.; Amorós, P., Organic–Inorganic Hybrid Mesoporous Materials as Regenerable Sensing Systems for the Recognition of Nitroaromatic Explosives. *ChemPlusChem* **2013,** *78* (7), 684-694.

75. Ong, S.; Zhao, X.; Eisenthal, K. B., Polarization of water molecules at a charged interface: second harmonic studies of the silica/water interface. *Chemical Physics Letters* **1992,** *191* (3), 327-335.

76. Dong, Y.; Pappu, S. V.; Xu, Z., Detection of Local Density Distribution of Isolated Silanol Groups on Planar Silica Surfaces Using Nonlinear Optical Molecular Probes. *Analytical Chemistry* **1998,** *70* (22), 4730-4735.

77. Lorenz, C. D.; Crozier, P. S.; Anderson, J. A.; Travesset, A., Molecular Dynamics of Ionic Transport and Electrokinetic Effects in Realistic Silica Channels. *The Journal of Physical Chemistry C* **2008,** *112* (27), 10222-10232.

78. Ostroverkhov, V.; Waychunas, G. A.; Shen, Y. R., Vibrational spectra of water at water/α-quartz (0001) interface. *Chemical Physics Letters* **2004,** *386* (1), 144-148.

79. Leung, K.; Nielsen, I. M. B.; Criscenti, L. J., Elucidating the Bimodal Acid−Base Behavior of the Water−Silica Interface from First Principles. *Journal of the American Chemical Society* **2009,** *131* (51), 18358-18365.

80. Sulpizi, M.; Gaigeot, M.-P.; Sprik, M., The Silica–Water Interface: How the Silanols Determine the Surface Acidity and Modulate the Water Properties. *Journal of Chemical Theory and Computation* **2012,** *8* (3), 1037-1047.

81. Darlington, A. M.; Gibbs-Davis, J. M., Bimodal or Trimodal? The Influence of Starting pH on Site Identity and Distribution at the Low Salt Aqueous/Silica Interface. *The Journal of Physical Chemistry C* **2015,** *119* (29), 16560-16567.

82. Rosenholm, J. M.; Czuryszkiewicz, T.; Kleitz, F.; Rosenholm, J. B.; Lindén, M., On the Nature of the Brønsted Acidic Groups on Native and Functionalized Mesoporous Siliceous SBA-15 as Studied by Benzylamine Adsorption from Solution. *Langmuir* **2007,** *23* (8), 4315-4323.

83. Fattakhova-Rohlfing, D.; Wark, M.; Rathouský, J., Ion-Permselective pH-Switchable Mesoporous Silica Thin Layers. *Chemistry of Materials* **2007,** *19* (7), 1640-1647.

84. Zheng, H.; Tai, C.-W.; Su, J.; Zou, X.; Gao, F., Ultra-small mesoporous silica nanoparticles as efficient carriers for pH responsive releases of anti-cancer drugs. *Dalton Transactions* **2015,** *44* (46), 20186-20192.

85. Mitran, R.-A.; Matei, C.; Berger, D., Correlation of Mesoporous Silica Structural and Morphological Features with Theoretical Three-Parameter Model for Drug Release Kinetics. *The Journal of Physical Chemistry C* **2016,** *120* (51), 29202-29209.

86. Fujita, S.; Koiwai, A.; Kawasumi, M.; Inagaki, S., Enhancement of Proton Transport by High Densification of Sulfonic Acid Groups in Highly Ordered Mesoporous Silica. *Chemistry of Materials* **2013,** *25* (9), 1584-1591.

87. Gao, Q.; Xu, W.; Xu, Y.; Wu, D.; Sun, Y.; Deng, F.; Shen, W., Amino Acid Adsorption on Mesoporous Materials: Influence of Types of Amino Acids, Modification of Mesoporous Materials, and Solution Conditions. *The Journal of Physical Chemistry B* **2008,** *112* (7), 2261-2267.

88. O'Reilly, J. P.; Butts, C. P.; I'Anso, I. A.; Shaw, A. M., Interfacial pH at an Isolated Silica−Water Surface. *Journal of the American Chemical Society* **2005,** *127* (6), 1632-1633.

89. Sen, T.; Barisik, M., Internal surface electric charge characterization of mesoporous silica. *Scientific Reports* **2019,** *9* (1), 137.

90. Kovaleva, E. G.; Molochnikov, L. S.; Golovkina, E. L.; Hartmann, M.; Kirilyuk, I. A.; Grigoriev, I. A., Electrical potential near hydrated surface of ordered mesoporous molecular sieves assessed by EPR of molecular pH-probes. *Microporous and Mesoporous Materials* **2015,** *203*, 1-7.

91. Kovaleva, E. G.; Molochnikov, L. S.; Antonov, D. O.; Tambasova Stepanova, D. P.; Hartmann, M.; Tsmokalyuk, A. N.; Marek, A.; Smirnov, A. I., Proton Activity in Nanochannels Revealed by Electron Paramagnetic Resonance of Ionizable Nitroxides: A Test of the Poisson–Boltzmann Double Layer Theory. *The Journal of Physical Chemistry C* **2018,** *122* (35), 20527-20538.

92. Kovaleva, E. G.; Molochnikov, L. S.; Golovkina, E. L.; Hartmann, M.; A. Kirilyuk, I.; A. Grigor'ev, I., Dynamics of pH-sensitive nitroxide radicals in water adsorbed in ordered mesoporous molecular sieves by EPR Spectroscopy. *Microporous and Mesoporous Materials* **2013,** *179*, 258-264.

93. Valetti, S.; Feiler, A.; Trulsson, M., Bare and Effective Charge of Mesoporous Silica Particles. *Langmuir* **2017,** *33* (29), 7343-7351.

94. Shenderovich, I. G.; Buntkowsky, G.; Schreiber, A.; Gedat, E.; Sharif, S.; Albrecht, J.; Golubev, N. S.; Findenegg, G. H.; Limbach, H.-H., Pyridine-15N A Mobile NMR Sensor for Surface Acidity and Surface Defects of Mesoporous Silica. *The Journal of Physical Chemistry B* **2003,** *107* (43), 11924-11939.

95. Yamaguchi, A.; Namekawa, M.; Kamijo, T.; Itoh, T.; Teramae, N., Acid−Base Equilibria inside Amine-Functionalized Mesoporous Silica. *Analytical Chemistry* **2011,** *83* (8), 2939-2946.

96. Thörn, C.; Carlsson, N.; Gustafsson, H.; Holmberg, K.; Åkerman, B.; Olsson, L., A method to measure pH inside mesoporous particles using protein-bound SNARF1 fluorescent probe. *Microporous and Mesoporous Materials* **2013,** *165*, 240-246.

CHAPTER 2. POLARITY CONTROL AT INTERFACES: QUANTIFYING PSEUDO-SOLVENT EFFECTS IN NANOCONFINED SYSTEMS

Reprinted with permission from *ChemPhysChem* **2016,** *17* (19), 2982-2986.

Dilini Singappuli-Arachchige[1,2], J. Sebastian Manzano[1,2], Lindy M. Sherman[2], Igor I. Slowing[1,2]

[1]US DOE Ames Laboratory, Ames, Iowa 50011, United States

[2]Department of Chemistry, Iowa State University, Ames, Iowa 50011, United States

Abstract

Surface functionalization controls local environments and induces solvent-like effects at liquid–solid interfaces. We explored structure–property relationships between organic groups bound to pore surfaces of mesoporous silica nanoparticles and Stokes shifts of the adsorbed solvatochromic dye Prodan. Correlating shifts of the dye on the surfaces with its shifts in solvents resulted in a local polarity scale for functionalized pores. The scale was validated by studying the effects of pore polarity on quenching of Nile Red fluorescence and on the vibronic band structure of pyrene. Measurements were done in aqueous suspensions of porous particles, proving that the dielectric properties in the pores are different from the bulk solvent. The precise control of pore polarity was used to enhance the catalytic activity of TEMPO in the aerobic oxidation of furfuryl alcohol in water. An inverse relationship was found between pore polarity and activity of TEMPO in the pores, demonstrating that controlling the local polarity around an active site allows modulating the activity of nanoconfined catalysts.

Introduction

Chemical processes at liquid–solid interfaces are ubiquitous in nature and technology. Porous materials like zeolites, MOFs, mesoporous oxides or carbons have high surface areas and are extensively used in processes involving liquid–solid interfaces. These surfaces are frequently modified with organic groups to enhance performance in several applications, including catalysis, separations, drug delivery, and sensing.[1] For example Vallet-Regí found that modifying mesoporous silica pores with alkyl chains allowed controlling drug release rates,[2] Martínez-Máñez attached hydrophobic groups to pore surfaces to facilitate sulfite detection by chromogenic probes,[3] Karimi showed that binding octyl groups to SBA-15 enhanced selectivity of tungstates in the oxidation of sulfides in water.[4] In these and similar cases,[5] the effect of organic groups has been ascribed to creation of hydrophobic environments at the surface, in spite of the materials being suspended in water. This assumption implies that the liquid–solid interface has different dielectric properties than the bulk solvent, and that these properties depend on the immobilized groups.[6] Thus, surface organic groups may be considered as solvent-like species that affect the behavior of diffusing molecules by mechanisms similar to classic solvent effects.[7] Following this idea, this work explores the relationship between surface functionalization of mesoporous silica and interface polarity, to provide a tool for better understanding previous literature data and improving materials design for rational control of chemical processes at liquid-solid interfaces.

Results and Discussion

We produced a set of surface functionalized mesoporous silica nanoparticles (MSNs) by co-condensing organosilanes with tetraethyl orthosilicate.[8] The organosilanes were chosen based on their DFT calculated dipole moments (Scheme 1). Successful incorporation of the groups was verified by FTIR and combustion analysis. Characterization by XRD, TEM and nitrogen

physisorption confirmed all materials correspond to ordered MCM-41 silicas with similar surface areas and pore widths (Table S1, Figures S 1-4).

To determine the polarity at the interface of the pores, the solvatochromic dye Prodan was adsorbed to the particles.[9] The dye-loaded MSNs were suspended in water and analysed by fluorescence spectroscopy. The Stokes shift of Prodan depends on stabilization of its excited state by the environment.[10] In a polar medium, the zwitterionic excited state is stabilized via organization of surrounding solvent dipoles. This organization also destabilizes the less polar ground state, resulting in a smaller energy gap that corresponds to emission of long wavelengths (Figure 1a). Conversely, lower solvent polarities lead to larger energy gaps, and therefore smaller Stokes shifts. As expected, the shifts of aqueous suspensions of Prodan loaded MSNs were smaller than the shift of the free dye in water (187 nm), and increased with the polarity of the bound organic groups (Figures 1b,c, S5). The supernatants obtained upon centrifugation were non-fluorescent. Redispersion of the solids in fresh water led to fluorescent suspensions emitting at the original λ_{max}, confirming the probe remained adsorbed to the MSNs.

A scale of local pore polarity was then produced by correlating the Stokes shifts of Prodan loaded materials with the shifts of the free dye in several solvents (Figure S6).[7b] Relative polarities of the materials ranged from 0.69 to 1.01 (Table S3). Increasing the surface density of the organic groups enhances their effect on the probe molecules: a linear correlation was observed between the surface density of 3-methoxyproyl groups and the Stokes shifts of the loaded dye (Figures 2, S7).

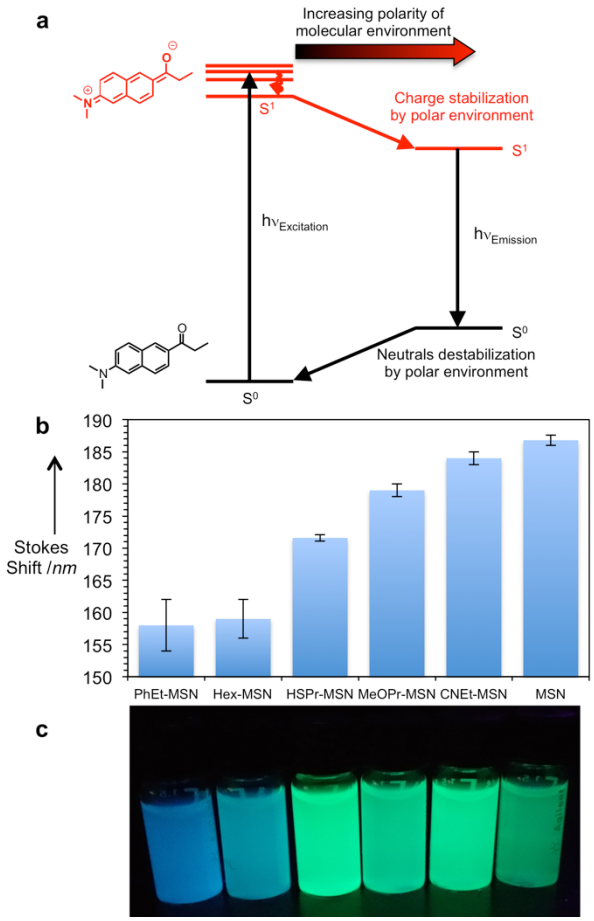

Figure 1. a) Jablonski diagram showing the dependence of Prodan fluorescence on the environmental stabilization of its excited state. b) Variation of Prodan Stokes shifts with the organic groups in functionalized MSNs, and c) picture of the aqueous suspensions of the materials under UV lamp (left to right: phenethyl-, hexyl-, 3-mercaptopropyl-, 3-methoxypropyl-, 2-cyanoethyl- and non-functionalized MSNs).

These results suggest that even if the tethered organic groups are not entirely mobile they can still participate in guest solvation, and therefore may be considered as pseudo-solvents at the interface. This implies that molecules inside the pores experience a unique mode of heterogeneous solvation involving fixed organic groups, mobile solvent molecules, and surface silanols of the support. The combination of all these species ultimately defines the dielectric properties and molecular environment at the interface.

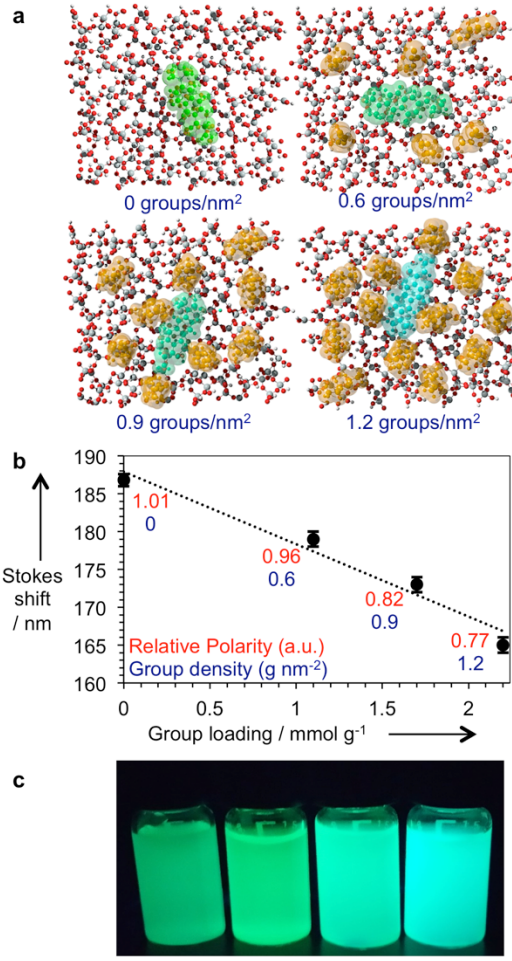

Figure 2. a) Molecular models of Prodan on the surface of MSNs with increasing surface densities of 3-methoxypropyl groups, based on Ugliengo's model[11] and optimized with SIMOMM;[12] b) Stokes shifts of Prodan loaded MSNs with varying surface densities of 3-methoxypropyl groups, and c) appearance of their suspensions under UV light (densities increasing left to right).

Co-immobilizing more than one organic group on the material enables further tuning of pore polarity. Analogous to mixing solvents, binding two groups with different polarities leads to pores with dielectric properties in between those of the monofunctional materials. For example, an MSN containing both phenethyl- and 2-cyanoethyl- groups displayed a relative polarity of 0.82 ± 0.02 (Stokes shift 173 ± 2nm) right between those of the original monofunctional MSNs (0.70 ± 0.03 and 0.98 ± 0.01, Figure S8). Importantly, this unique approach may allow combining species that

could be immiscible in liquid phase, and produce pseudo-solvent mixtures that have no homogeneous analogue.

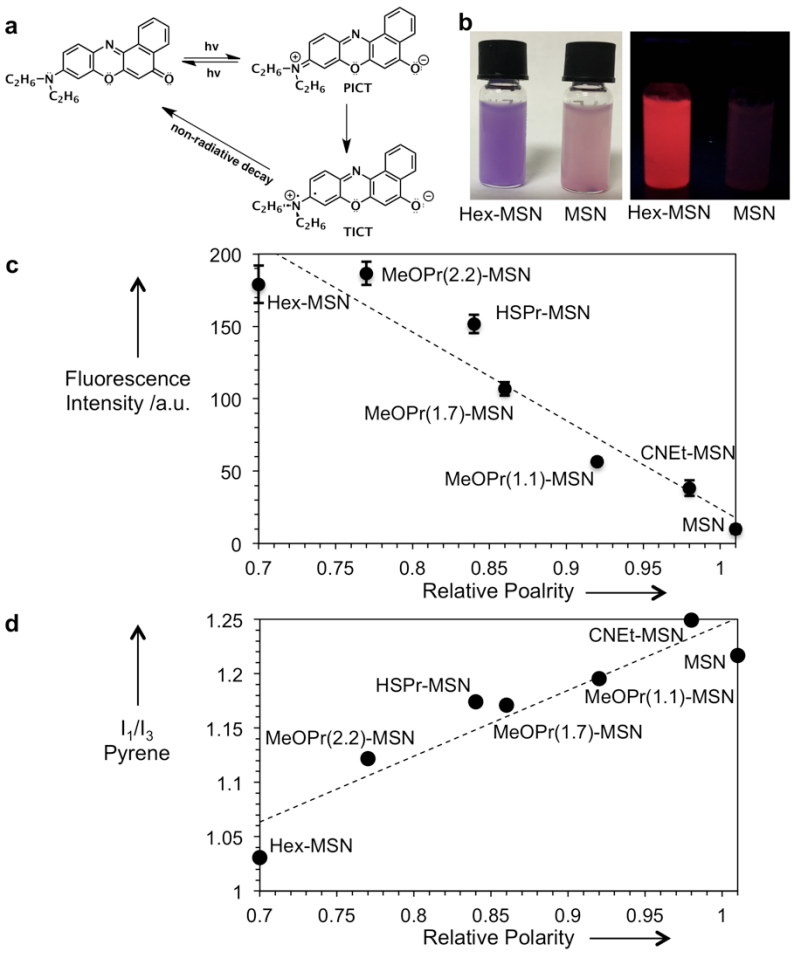

Figure 3. a) Excitation of Nile Red produces a planar intramolecular charge transfer state that turns into a non-emissive twisted state in polar environments. b) Aqueous suspensions of Nile Red loaded in Hex-MSN and non-functionalized MSN under visible light (left) and UV irradiation (right). c) Fluorescence intensity of Nile Red and d) ratio between first and third vibronic bands of pyrene in MSNs as a function of pore polarity.

To evaluate the local polarity scale of functionalized MSNs, we examined whether the pore environments could control the relaxation pathways of Nile Red's excited state. Excitation of Nile Red leads to a planar charge transfer (PICT) state that emits at 645 nm. However, its emission quantum yield sharply decreases with increasing solvent polarity. This behavior has been ascribed

to a geometry change into a twisted intramolecular charge transfer (TICT) state with higher dipole moment that undergoes non-radiative decay (Figure 3a).[13] As expected, the aqueous suspensions of Nile Red loaded MSNs displayed a linear trend of decreasing fluorescence intensities with increasing pore polarity (Figures 3c, S9). For example, while Hex-MSN (polarity index 0.70) gave a bright suspension, the fluorescence was completely quenched in non-functionalized MSN (polarity index 1.01, Figure 3b).

We also evaluated the effects of pore polarity on the vibronic band structure of pyrene, which is strongly affected by its immediate molecular environment.[14] While the first vibronic band is enhanced by dipolar coupling with the solvent, the other bands are barely perturbed by their environment. Thus, the ratio of band intensities (373 and 383 nm, I_1/I_3) is used as indicator of environmental polarity.[14d] The fluorescence spectra of pyrene loaded MSNs revealed that indeed, the I_1/I_3 ratios vary linearly with the calculated pore polarities (Figures 3d, S10). Importantly, the main contributor to I_1 enhancement is dipolar coupling with solvent molecules rather than bulk solvent effects.[14a] Therefore, these results suggest solvation-like interactions between the supported groups and pyrene.

Finally, we used the MSNs with known polarities as nanoreactors in water to control the aerobic oxidation of furfuryl alcohol catalyzed by TEMPO (Figure 4a).[15] Han reported that this oxidation is enhanced by decreasing solvent polarity,[16] likely due to a drop in the activation barrier of rate-limiting α-hydride abstraction.[17] In the transition state, the charge of the oxoammonium intermediate is dispersed over its complex with the alcohol (Figure 4b). According to the Hughes-Ingold postulates, non polar solvents reduce the activation energy of a reaction when the charge density of the transition state is smaller than the reactant (Figure 4c).[18] Indeed, the oxidation of furfuryl alcohol gave higher furfural yields in heptane than in water (72 ± 6 % versus 20 ± 2 %,

no MSN added). However the reaction in heptane was limited by the solubility of $FeCl_3$ co-catalyst, and required addition of excess salt. In contrast, impregnation of TEMPO and $FeCl_3$ into Hex-MSN (relative polarity 0.70) allowed performing the reaction in water, did not require excess salt, and resulted in a superior performance (100 % yield) (Figure 4d). Importantly, no TEMPO was detected in solution by GC/MS, indicating the catalyst does not leach and the oxidation happens inside of the pores. This result provides further evidence that the pores provide local environments with lower polarity than the bulk solvent.

Furthermore, when using different MSNs for the reaction, we observed a quasi-linear relationship between pore polarity and aldehyde yield (Figure 4e). This result suggests that the catalytic behaviour of the active site is not affected by the polarity of the bulk solvent, but is exclusively controlled by the dielectric properties of its local environment. This type of interfacial solvent effect has been previously proposed for zeolites and other confined systems,[19] and suggests that controlling the solvation properties in the immediacy of the active sites may be as critical to the stabilization of transition states as controlling the sterics and charge distribution (i.e. molecular recognition) at the site.[20]

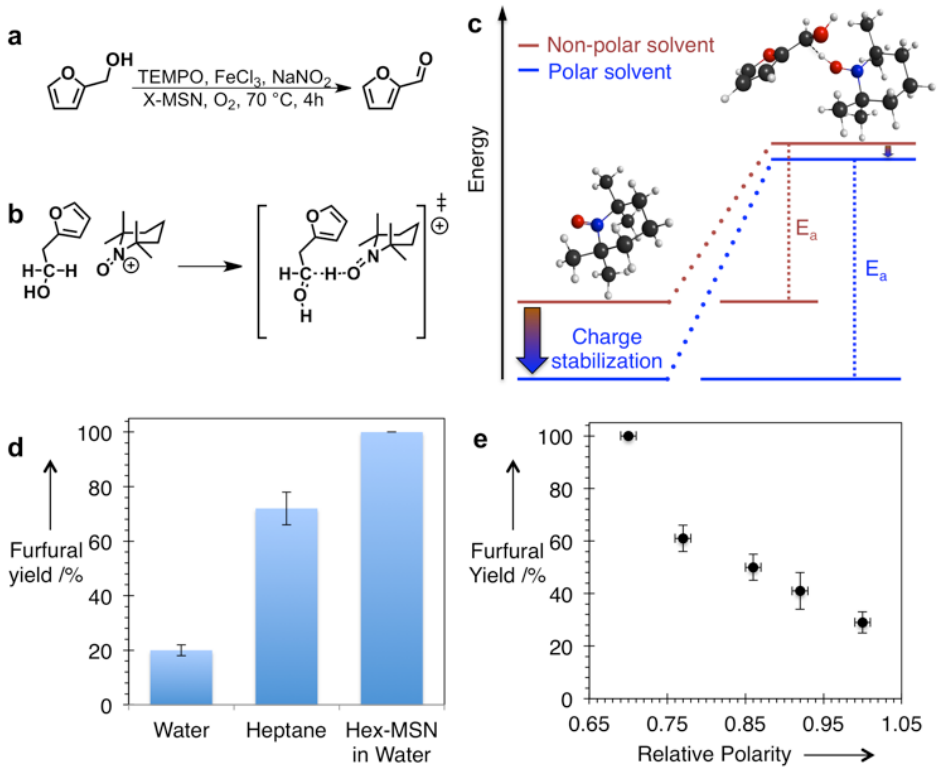

Figure 4. a) Selective TEMPO catalyzed aerobic oxidation of furfuryl alcohol. b) Transition state of the rate determining step, and c) its stabilization relative to the densely charged intermediate by non-polar solvents. d) Furfural yields for the reaction in water, heptane and aqueous Hex-MSN. e) Furfural yields as a function of pore polarity for aqueous suspensions of MSNs.

Materials and Methods

Materials

Hexadecyltrimethylammonium bromide (CTAB), methanol, Nile Red, pyrene, TEMPO, furfuryl alcohol and furfural were purchased from Sigma-Aldrich. Tetraethylorthosilicate (TEOS), hexyltrimethoxysilane, phenethyltrimethoxysilane, 3-methoxypropyltrimethoxysilane, 3-mercaptopropyltrimethoxysilane, and 3-cyanoethyl-triethoxysilane were purchased from Gelest, Inc. NaOH, HCl, glycerol, 1-propanol, 2-propanol, 1-butanol, 1-pentanol, acetone, FeCl3.6H2O, and NaNO2 were purchased from Fisher Scientific. Ethanol was purchased from

Decon Laboratories, and Prodan from Anapec, Inc. All reagents were used as received without further purification.

Synthesis of MSNs

CTAB (1.0 g, 2.74 mmol) was dissolved in deionized water (480 mL, 18 MΩ.cm) in a round bottom flask followed by NaOH (2M, 3.5 mL, 7.0 mmol). The solution was stirred for 1 h at 80 °C. Tetraethylorthosilicate (TEOS, 5.0 mL, 22.6 mmol) was then added dropwise over 5 min to the solution, followed by dropwise addition (1 min) of an organosilane according to Table S2. Stirring was continued for additional 2 h at 80 °C. The solution was filtered, washed with abundant water and methanol, and vacuum dried overnight. CTAB template was removed by refluxing 1.0 g of dry solid with methanol solution (100 mL) of concentrated HCl (0.8 mL, 9.7 mmol) for 6 h. The surfactant-free sample was then filtered, washed with abundant methanol and water and vacuum dried overnight. Three different batches were prepared of each material to ensure reproducibility and obtain statistical data.

Characterization

XRD patterns were recorded on a Rigaku-Ultima 4 X–ray diffractometer equipped with Cu Kα radiation (40 kV, 44 mA) over the range of 1–5 2θ degrees. Nitrogen sorption isotherms were measured on a Micromeritics Tristar surface area and porosity analyzer. The surface areas and pore size distributions were calculated by the Brunauer Emmett Teller (BET) and Barrett Joyner Halenda (BJH) methods respectively. Elemental analyses of the dry samples were done by triplicate on a Perkin Elmer 2100 series II CHNS analyzer, using acetanilide as calibration standard and combustion and reduction temperatures of 925 °C and 640 °C respectively. Transmission Electron Microscopy (TEM) images were obtained using a FEI Tecnai G2 F20 working at 200 kV. TEM samples were prepared by placing 2-3 drops of dilute methanol suspensions onto a carbon-coated copper grid. Diffuse Reflectance Infrared Fourier Transform

(DRIFT) measurements were made on a Bruker Vertex 80 FT-IR spectrometer equipped with a HeNe laser and photovoltaic MCT detector and OPUS software.

Probe impregnation

Prodan (2.5 mg, 0.01 mmol), Nile Red (2.0 mg, 0.01 mmol) and Pyrene (3.0 mg, 0.01 mmol) were dissolved in acetone (10.0 mL) separately. The freshly prepared dye solutions (10 μL each) were added to MSN samples (10.0 mg each) separately, grinded and let to dry. Probe loadings were 1.0 μmol g-1.

Fluorescence measurements

Probe loaded samples (10.0 mg) were suspended in water (2.0 mL). The suspensions were then excited at the corresponding wavelength of each probe (prodan-337 nm, nile red-557 nm, pyrene-330 nm) in a Cary Eclipse Fluorescence Spectrophotometer. Fluorescence emission was scanned with both excitation and emission slit widths set at 5 nm.

Calibration series of alcohols

Prodan (2.5 mg, 0.011 mmol) was dissolved in water, glycerol, methanol, ethanol, 1-propanol, 2-propanol, 1-butanol, and 1-pentanol (10.0 mL each). Each solution was then diluted 1,000-fold with the corresponding solvent to obtain final concentrations similar to those used in MSN samples, and analyzed using the same parameters as MSN samples. Fluorescence λmax was plotted against the literature values of relative polarities of the solvents.

Catalytic oxidation of furfuryl alcohol

TEMPO (75.0 mg, 0.48 mmol) and FeCl3•6H2O (50.0 mg, 0.18 mmol) were dissolved in acetone (0.25 mL). The freshly prepared solution (0.030 mL, TEMPO - 0.058 mmol, FeCl3•6H2O - 0.022 mmol) was grinded with MSN samples (30 mg each) and let dry. Each sample was added to water (2mL), stirred at 550 rpm for 1 min, followed by addition of furfuryl alcohol (0.050 mL, 0.58 mmol) and NaNO2 (7.0 mg, 0.10 mmol). The final mole % of each reagent in the

reaction were: TEMPO -10 mol%, FeCl3•6H2O- 10 mol%, NaNO2 – 18 mol%. O2 gas was purged for 1 min (26 mL min-1 rate), the vials were sealed and heated at 70 °C for 4 h. For the homogeneous reactions run in absence of MSN the reagents and furfuryl alcohol (0.050 mL, 0.58 mmol) were dissolved in each of the test solvents (water and heptane), followed by purging for 1 min with O2 (26 mL min-1), sealing the vials and heating at 70 °C for 4 h. Because of limited solubility of FeCl3 in heptane, this reagent was added in a 2.5-fold excess for the reaction in this solvent (16.1 mg, 0.058 mmol). The reaction mixtures were centrifuged, an aliquot (100 μL) of the supernatant was diluted with ethanol (1 mL) analyzed in an Agilent GC-MS instrument (7890A, 5975C) with a HP-5MS column to quantify furfuryl alcohol and furfural.

Computational details

All calculations were performed within the Density Functional Theory (DFT) implementing the Becke, 3 parameters, Lee-Yang-Parr (B3LYP)[20] hybrid functional and the all electron 6-311++G(d,p) basis set. GAMESS[21] (General Atomic and Molecular Electronic Structure System) program was used for all of the computations.

The method used for calculating reaction pathway involved: (i) geometry optimization and vibrational frequency calculations, and (ii) single point free energy calculations. Surface models (10 nm2, 4 atomic layers deep) were generated using the model developed by Ugliengo.[11] The organic groups were added at random and optimized using the hybrid quantum/molecular mechanics method SIMOMM.[12]

Conclusions

In summary, this work shows that it is possible to produce local environments in confined domains with precisely controlled dielectric properties, and that these properties are distinct from the bulk environment. The dielectric properties at liquid-solid interfaces are controlled by the nature and density of groups on the surface and their interaction with the solvent. The local polarity

at the interfaces can be quantified using solvatochromic probes even in the presence of bulk solvent. An important implication of these findings is that the design of advanced catalysts (e.g. enzyme mimics) requires controlling not only steric and charge distribution factors but also the local dielectric properties around the site. We envision that the quantitative relationships between surface functionalization and interface polarity established in this work will provide additional insights into previous and future studies of chemical processes at interfaces. We also expect pore polarity tuning to become a useful tool for the rational design of materials that control chemical processes at liquid-solid interfaces.

Acknowledgements

This research is supported by the U.S. Department of Energy, Office of Basic Energy Sciences, Division of Chemical Sciences, Geosciences, and Biosciences, through the Ames Laboratory Catalysis Science program. The Ames Laboratory is operated for the U.S. Department of Energy by Iowa State University under Contract No. DE-AC02-07CH11358.

Supplemental Tables and Figures

Table S1. Surface properties and functional group loading of different MSN samples.

Sample	SA_{BET} ($m^2\ g^{-1}$)	W_{BJH} (nm)	Group Loading (mmol g^{-1})
MSN	1231	2.9	-
Hex-MSN	1238	2.4	1.4
PhEt-MSN	1224	2.7	1.0
HSPr-MSN	1169	2.7	1.1
CNEt-MSN	1098	2.9	1.2
MeOPr-MSN	1147	2.7	1.1
MeOPr(1.7)-MSN	1129	2.6	1.7
MeOPr(2.2)-MSN	1128	2.4	2.2
PhEt/CNEt-MSN	1196	2.6	-

Table S2. Amounts of organosilanes used in the synthesis of functionalized MSN samples.

Sample	Ligand	Volume (mL)
MSN	-	-
Hex-MSN	hexyltrimethoxysilane	0.22
PhEt-MSN	phenethyltrimethoxysilane	0.22
HSPr-MSN	3-mercaptopropyltrimethoxysilane	0.19
CNEt-MSN	3-cyanoethyltriethoxysilane	0.22
MeOPr-MSN	3-methoxypropyltrimethoxysilane	0.19
MeOPr(1.7)-MSN	3-methoxypropyltrimethoxysilane	0.59
MeOPr(2.2)-MSN	3-methoxypropyltrimethoxysilane	0.97
PhEt/CNEt-MSN	phenethyltrimethoxysilane 3-cyanoethyltriethoxysilane	0.11 0.11

Table S3. Relative polarities of organofunctionalized MSNs.

Material	Prodan λmax (nm)[a]	Stokes Shift (nm)[a]	Relative Polarity[b]
PhEt-MSN	495 ± 4	158 ± 4	0.69 ± 0.04
Hex-MSN	496 ± 3	159 ± 3	0.70 ± 0.03
HSP-MSN	509 ± 1	172 ± 1	0.84 ± 0.01
MeOP-MSN	516 ± 1	179 ± 1	0.92 ± 0.01
CNEt-MSN	521 ± 1	184 ± 1	0.98 ± 0.01
MSN	524 + 1	187 + 1	1.01 + 0.01

[a] Averages obtained over measurement of three different batches of each material.
[b] Relative polarities corresponding to scale in reference 7b. (Reichardt, C.; Welton, T. In Solvents and Solvent Effects in Organic Chemistry, Wiley-VCH Verlag GmbH & Co. KGaA: 2010)

Table S4. Atomic charge distributions of the initial weakly bound complex between the oxoammonium form of TEMPO and Furfuryl alcohol (left), and of the activated complex (transition state). Highlighted at the bottom right of each complex is the difference in overall charge between oxoammonium and the alcohol.

INITIAL COMPLEX				TRANSITION STATE			
$TEMPO^+$ (T^+)		Furfuryl Alcohol (FA)		$TEMPO^+$ (T^+)		Furfuryl Alcohol (FA)	
Atom	Charge	Atom	Charge	Atom	Charge	Atom	Charge
C	-0.02	C	-0.1841	C	0.0566	C	-0.0848
C	-0.1883	C	0.3069	C	-0.2811	C	0.338
C	-0.1784	O	-0.2334	C	-0.3033	O	-0.2521
C	0.2687	C	-0.2803	C	0.6626	C	-0.3239
N	0.5196	C	0.0014	N	-0.1913	C	0.1217
C	0.2809	C	-0.1559	C	0.5419	C	-0.0497
O	-0.2123	O	-0.5418	O	-0.228	O	-0.54
C	-0.4779	H	0.1522	C	-0.506	H	0.1898
C	-0.419	H	0.2066	C	-0.7075	H	0.2294
C	-0.5611	H	0.1826	C	-0.5025	H	0.1802
C	-0.5414	H	0.1461	C	-0.4915	H	0.1708
H	0.0804	H	0.1421	H	0.0659	H	0.4878
H	0.0303	H	0.3901	H	0.0081	**Sum**	**0.4672**
H	0.1032	**Sum**	**0.1325**	H	0.0988		
H	0.0754			H	0.0818		
H	0.0752			H	0.0904		
H	0.1006			H	0.0972		
H	0.1491			H	0.0957		
H	0.1522			H	0.148		
H	0.162			H	0.1653		
H	0.0957			H	0.1863		
H	0.1547			H	0.1892		
H	0.1479			H	0.1906		
H	0.2013			H	0.1448		
H	0.1719			H	0.143		
H	0.1696			H	0.15		
H	0.166			H	0.1507		
H	0.1603			H	0.1488		
H	0.2008			H	0.1459		
Sum	**0.8674**		**Δq (T^+-FA)**	H	0.1825		**Δq (T^+-FA)**
			0.73	**Sum**	**0.5329**		**0.07**

Table S5. Coordinates of the initial weakly bound complex between the oxoammonium form of TEMPO and Furfuryl alcohol (left), and of the activated complex (transition state).

INITIAL COMPLEX					TRANSITION STATE				
C	6	-0.052422776	0.141923821	-0.216943555	**C**	6	0.074843765	-0.583548625	-0.581398421
C	6	-1.477144867	0.257059064	-0.753407081	**C**	6	-1.324431166	-0.2105875	-1.068224837
C	6	-0.079785228	-0.217081015	1.268196518	**C**	6	0.16474147	-0.365919922	0.92768524
C	6	-0.805193974	-1.539504742	1.595065346	**C**	6	-0.848311432	-1.193799555	1.741837141
N	7	-2.126000426	-1.599389474	0.803117132	**N**	7	-2.204273749	-1.115856829	1.078390146
C	6	-2.312826479	-1.032634171	-0.619559988	**C**	6	-2.453641153	-1.027364645	-0.410276572
O	8	-3.049570438	-2.166128343	1.30200468	**O**	8	-3.190462879	-1.570646151	1.774815686
C	6	-3.804190383	-0.756555789	-0.819229481	**C**	6	-3.801620895	-0.332330605	-0.650040581
C	6	-1.151163267	-1.636330706	3.082685653	**C**	6	-0.958231268	-0.622509508	3.164231876
C	6	0.011479787	-2.783875879	1.162600502	**C**	6	-0.436775234	-2.682595407	1.827222148
C	6	-1.845802062	-2.146113687	-1.589651947	**C**	6	-2.526375238	-2.465726177	-0.975883894
H	1	0.454160615	1.101968969	-0.342869094	**H**	1	0.814283266	0.043359143	-1.085918723
H	1	0.531427167	-0.582774911	-0.791527621	**H**	1	0.321519154	-1.616117821	-0.84578112
H	1	-1.479957088	0.519991573	-1.814539884	**H**	1	-1.412337138	-0.343109152	-2.149931188
H	1	-2.0003418	1.060151894	-0.225657887	**H**	1	-1.494851468	0.853585292	-0.868495388
H	1	-0.566843509	0.588018613	1.826487648	**H**	1	0.008003474	0.69689607	1.143940623
H	1	0.933515028	-0.31064108	1.667657443	**H**	1	1.162303453	-0.615497582	1.29876395
H	1	-4.183096972	-0.084496533	-0.048286779	**H**	1	-3.794961559	0.692228078	-0.265638237
H	1	-4.399477685	-1.669708894	-0.827101452	**H**	1	-4.633798227	-0.887277928	-0.215702308
H	1	-3.917798234	-0.270580181	-1.790534407	**H**	1	-3.973204343	-0.265410518	-1.725983997
H	1	-1.836315564	-0.840912916	3.379446004	**H**	1	-1.320299919	0.40708184	3.148092192
H	1	-0.221230197	-1.519295302	3.642718922	**H**	1	0.038140416	-0.625748329	3.61100823
H	1	-1.584565701	-2.60130371	3.344060016	**H**	1	-1.609247278	-1.228519304	3.795320403
H	1	0.861260076	-2.854256303	1.84458933	**H**	1	0.480196835	-2.761234582	2.415858646
H	1	0.399614772	-2.712719258	0.148785579	**H**	1	-0.243056566	-3.118684718	0.847318196
H	1	-0.577934473	-3.697196751	1.261483794	**H**	1	-1.213943931	-3.267072775	2.322657362
H	1	-2.35872195	-3.08760152	-1.384421478	**H**	1	-3.265287428	-3.056308692	-0.431563454
H	1	-0.770507885	-2.308664335	-1.57279532	**H**	1	-1.565870362	-2.977330709	-0.926341664
H	1	-2.122774369	-1.823394522	-2.595526524	**H**	1	-2.826333474	-2.420177643	-2.025410135
C	6	-3.833028342	0.742696531	5.402748162	**C**	6	-3.902731246	0.531589597	5.391454864
C	6	-4.714493094	0.141045493	4.550443276	**C**	6	-4.566518518	0.047121609	4.278484517
O	8	-5.772404157	-0.359131068	5.249044639	**O**	8	-5.445397313	-0.936299162	4.655929937
C	6	-4.388560592	0.607347202	6.715859235	**C**	6	-4.417390059	-0.178379539	6.499124907
C	6	-5.55790331	-0.069476547	6.566459046	**C**	6	-5.344893502	-1.056152031	5.996589493
C	6	-4.750028559	-0.075590841	3.075850183	**C**	6	-4.494894479	0.323652188	2.880805739
O	8	-3.751902667	0.679575126	2.385711655	**O**	8	-3.704650625	1.3741766	2.527155461
H	1	-2.907728791	1.227765359	5.135780807	**H**	1	-3.163454533	1.316538027	5.393975685

Table S5 continued

INITIAL COMPLEX					TRANSITION STATE				
H	1	-3.973484871	0.96922108	7.642996211	**H**	1	-4.152978977	-0.057685969	7.537594454
H	1	-6.319116737	-0.402256133	7.251661426	**H**	1	-5.9904866	-1.787051439	6.456299161
H	1	-5.754042534	0.142933444	2.69099028	**H**	1	-5.408058689	0.166773059	2.30269352
H	1	-4.543164528	-1.126832202	2.833438294	**H**	1	-3.810327866	-0.755937443	2.361777456
H	1	-3.908983936	1.616558644	2.554430715	**H**	1	-3.942951276	1.70380194	1.6522316

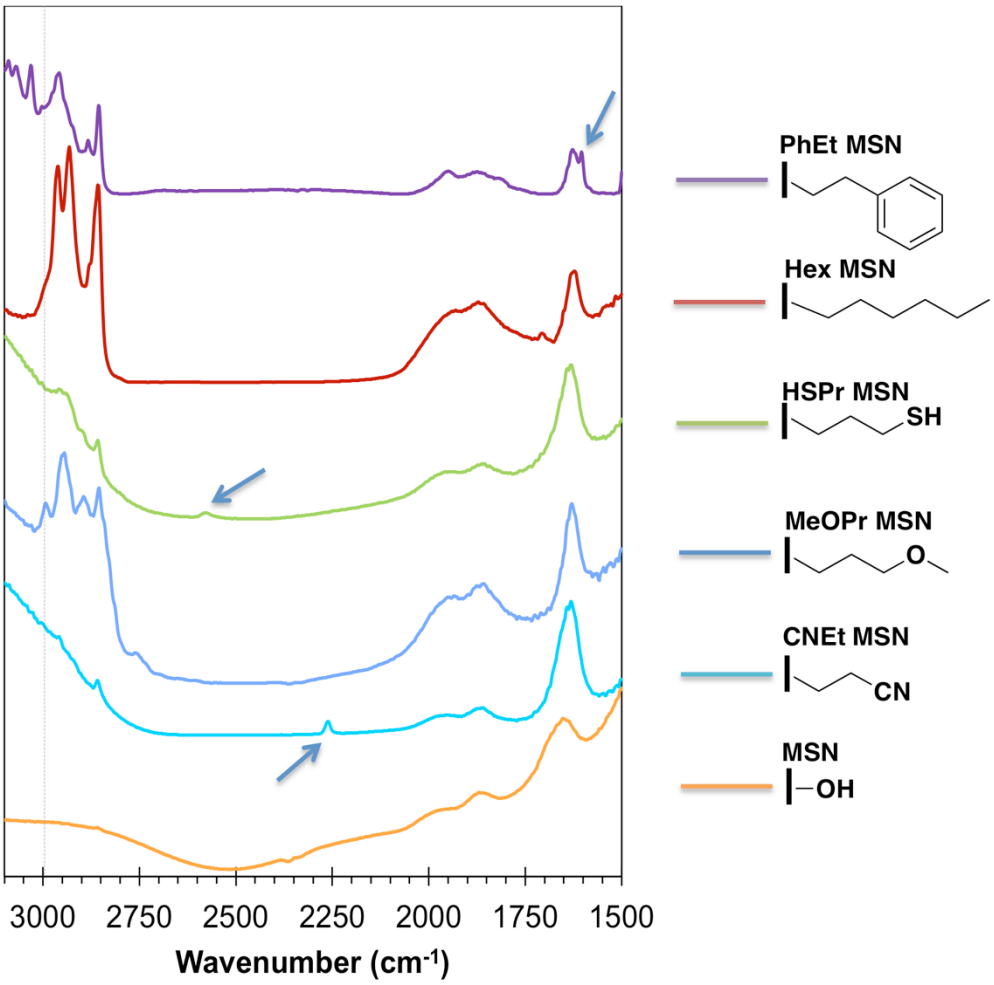

Figure S1. DRIFT-IR spectra of functionalized MSN materials. Characteristic features include intense –C–H stretching bands in the range 2800-2950 cm^{-1} for Hex-MSN and MeOPr-MSN, vibrational bands attributed to =C–H stretching in the range 3020-3100 cm^{-1} and C=C stretching at 1620 cm^{-1} for PhEt-MSN, S–H band at 2605 cm^{-1} for HSPr-MSN, and C≡N stretching band at 2280 cm^{-1} for CNEt-MSN.

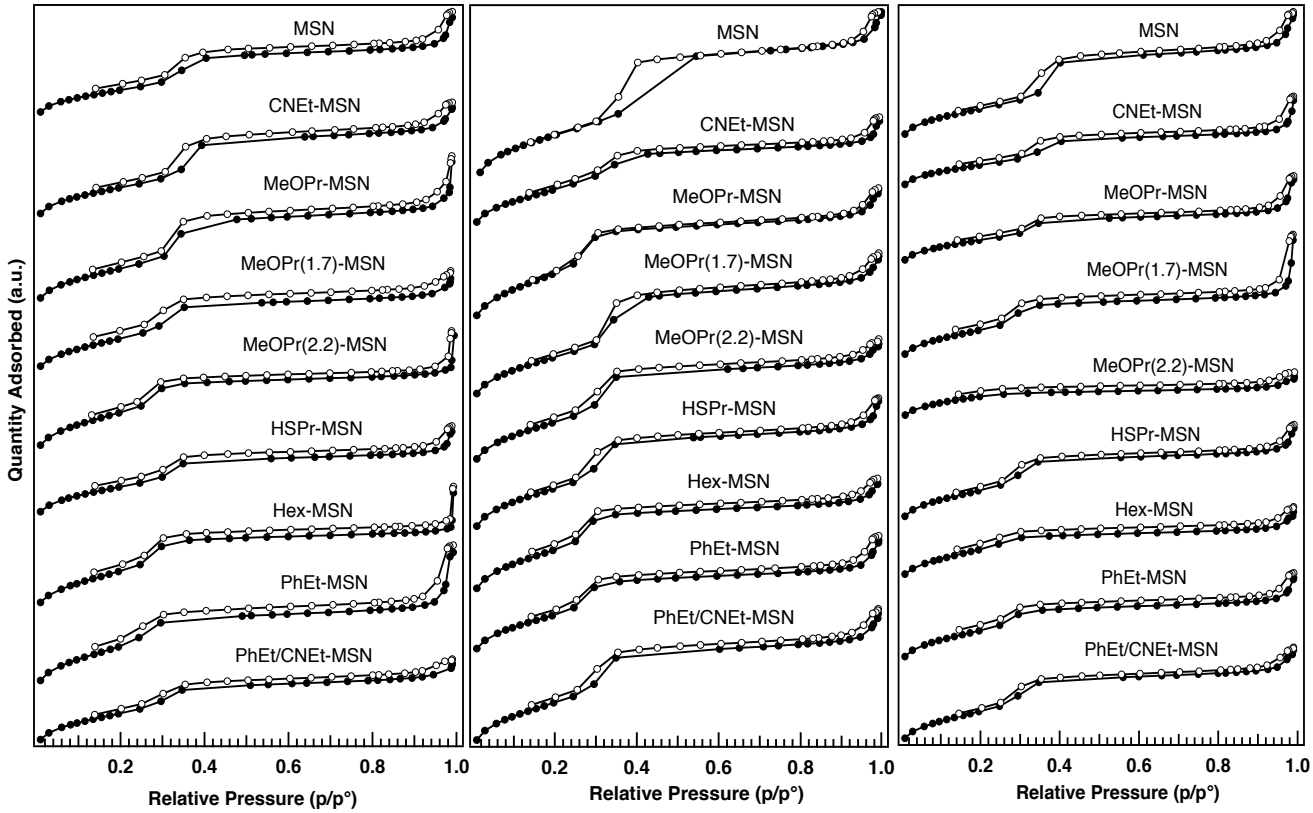

Figure S2. Characteristic type-IV nitrogen sorption isotherms of three different batches of the MSN materials.

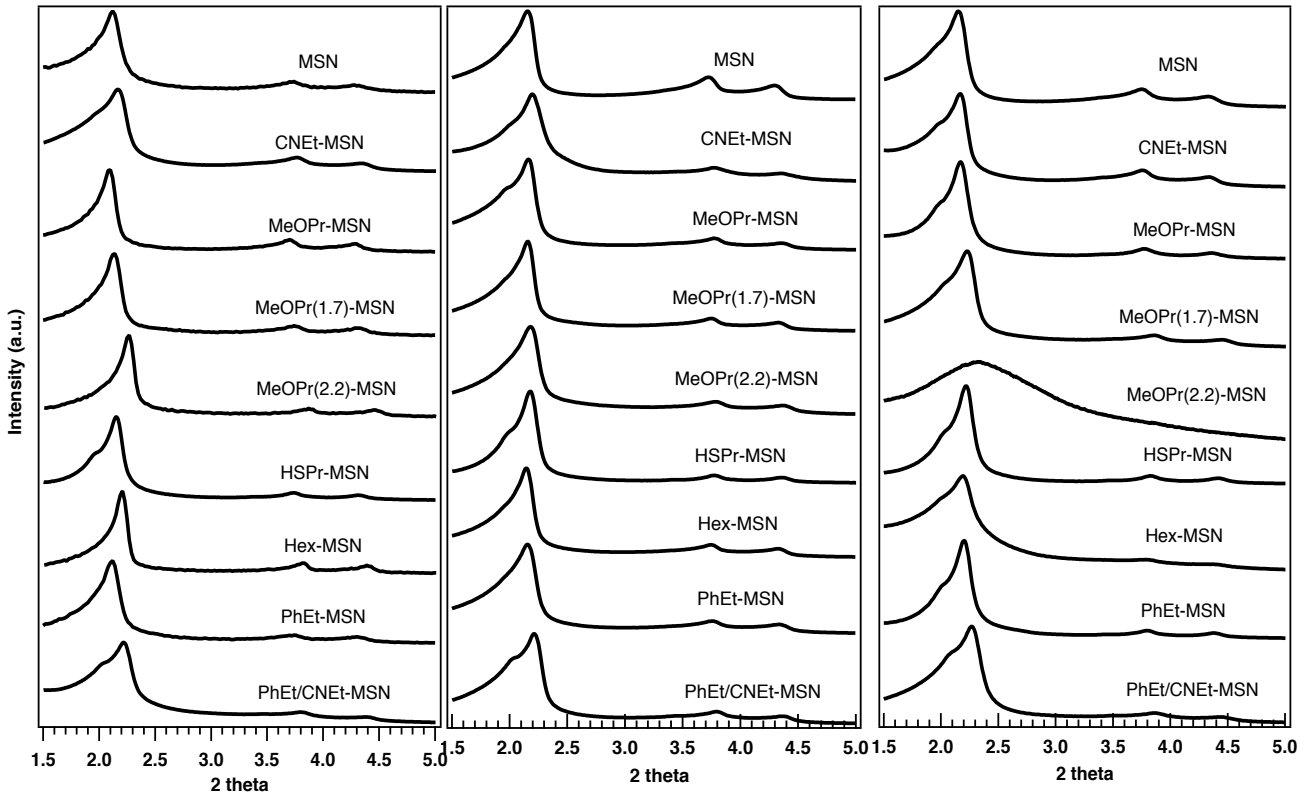

Figure S3. XRD patterns of three different batches of the MSN materials.

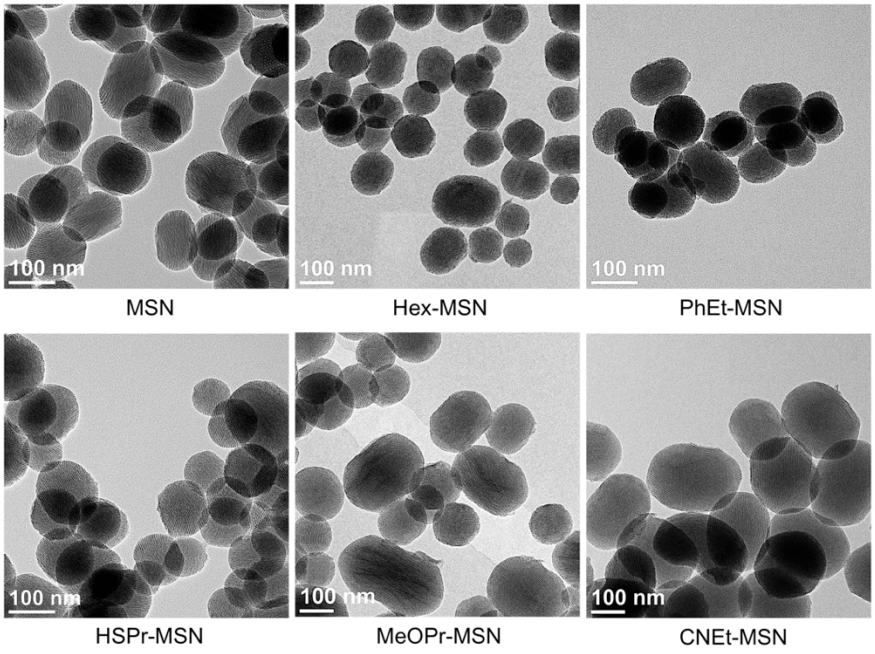

Figure S4. Transmission electron micrographs of the functionalized MSNs.

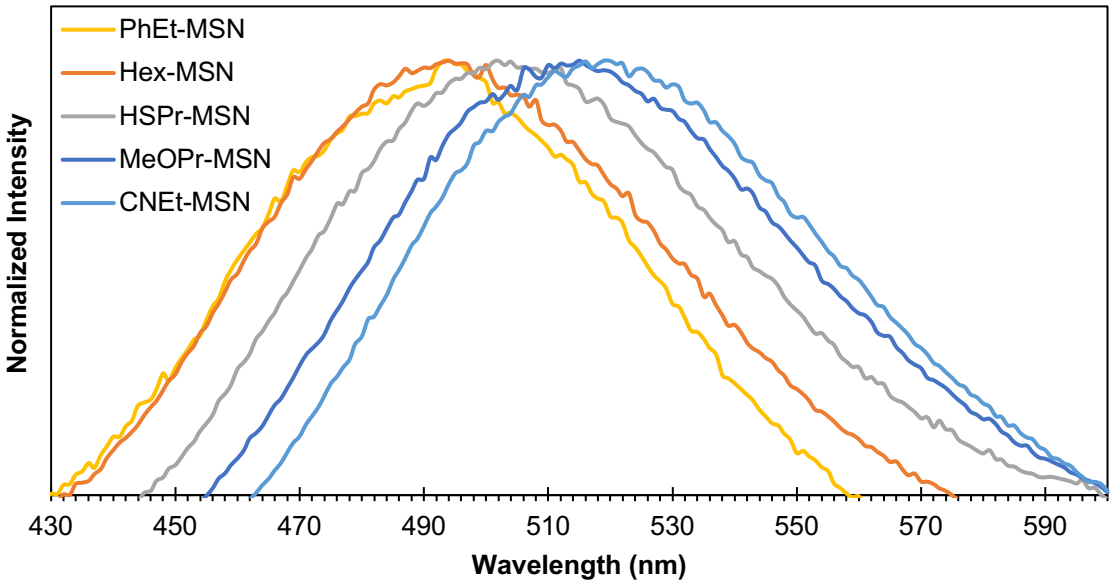

Figure S5. Fluorescence emission spectra of Prodan-loaded functionalized MSN samples suspended in water.

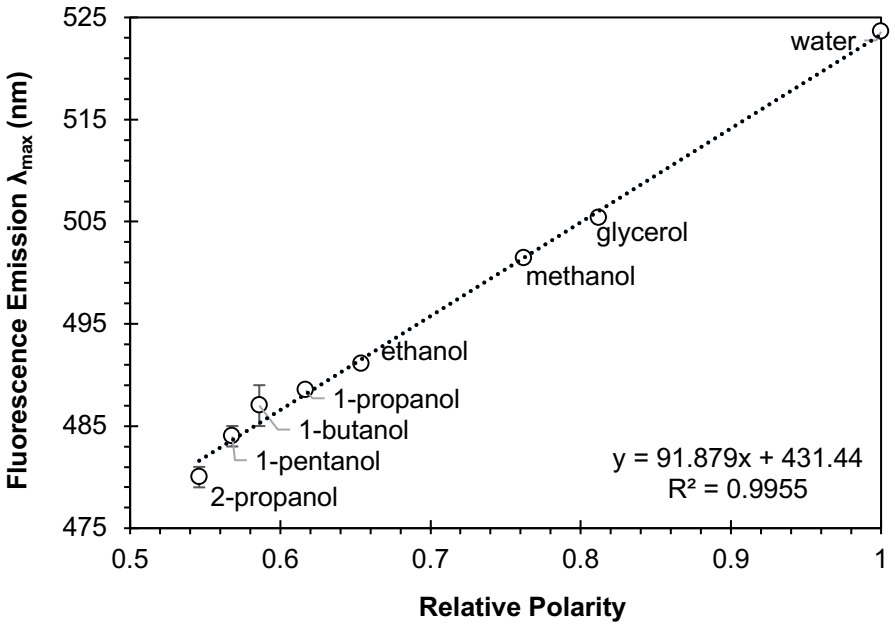

Figure S6. Calibration curve of emission λmax of Prodan versus relative polarity of solvents. (Reichardt, C.; Welton, T. In Solvents and Solvent Effects in Organic Chemistry, Wiley-VCH Verlag GmbH & Co. KGaA: 2010)

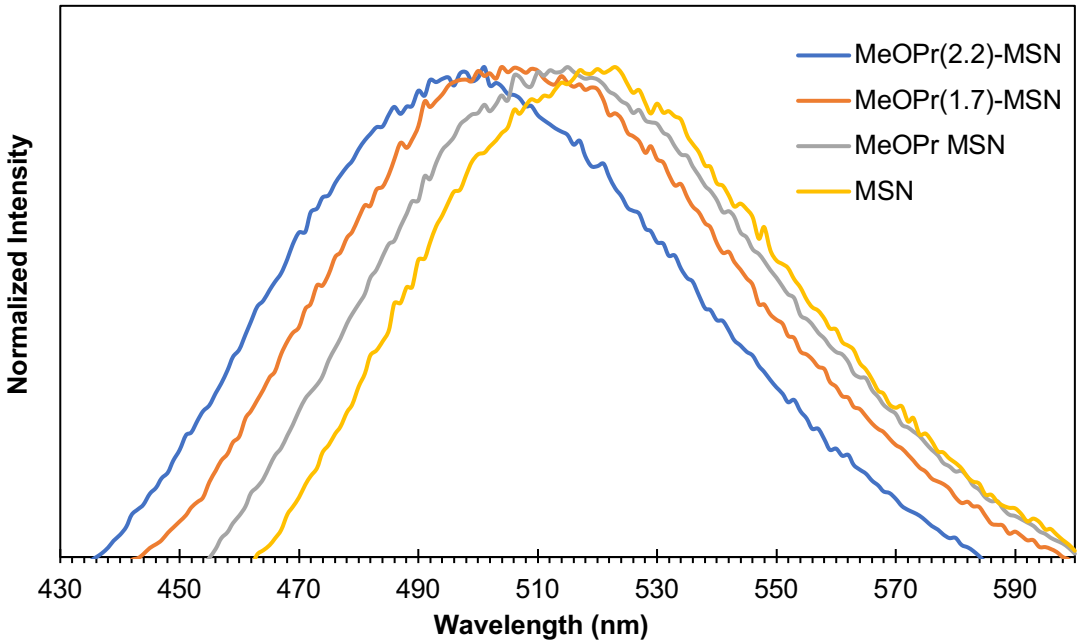

Figure S7. Fluorescence emission spectra of Prodan-loaded MeOPr(x)-MSN samples suspended in water. 3-methoxypropyl group loadings: 0, 1.1., 1.7 and 2.2 mmol g-1, corresponding to surface densities of 0, 0.6, 0.9 and 1.2 groups nm-2.

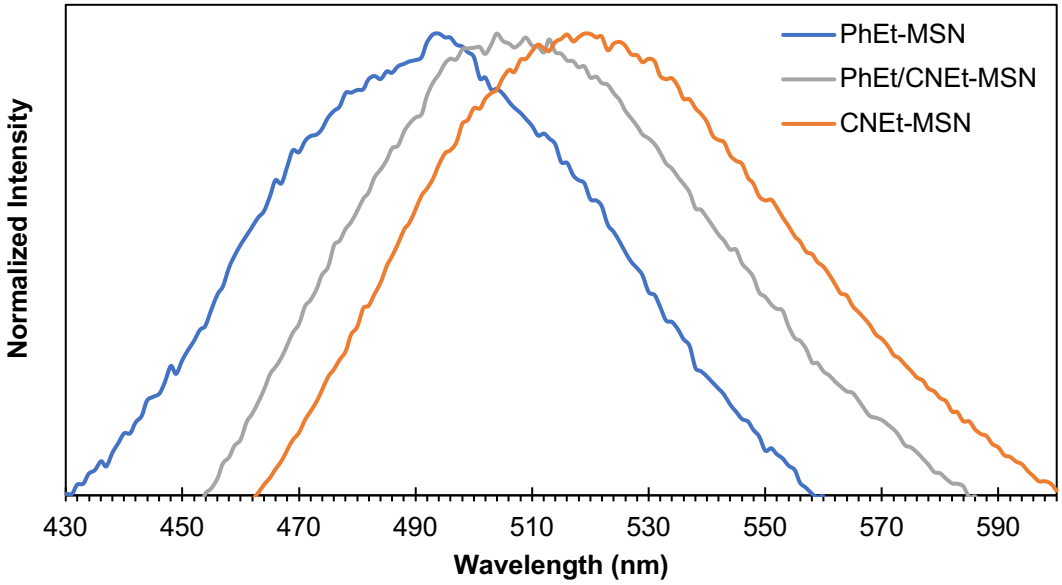

Figure S8. Fluorescence emission spectra of Prodan-loaded PhEt/CNEt-MSN, PhEt-MSN and CNEt-MSN samples suspended in water.

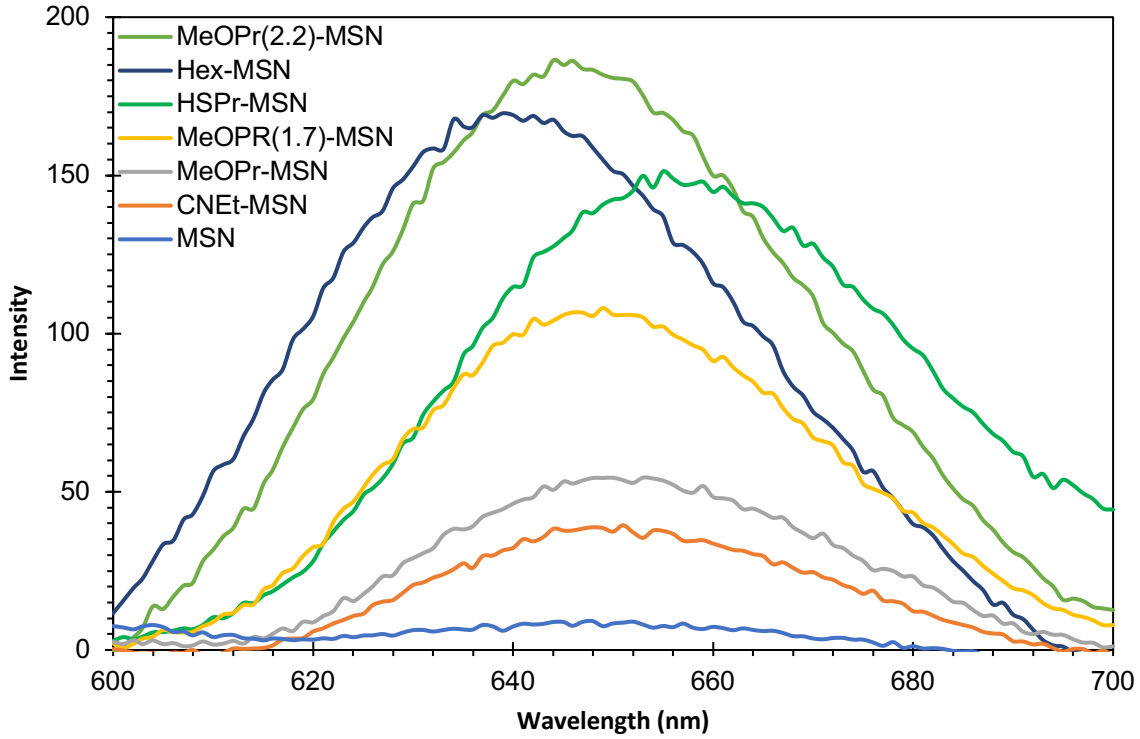

Figure S9. Fluorescence emission spectra of Nile Red-loaded functionalized MSN samples suspended in water. Dye loads (1 μmol g^{-1}) and particle concentration (5 mg mL^{-1}) were the same for all samples.

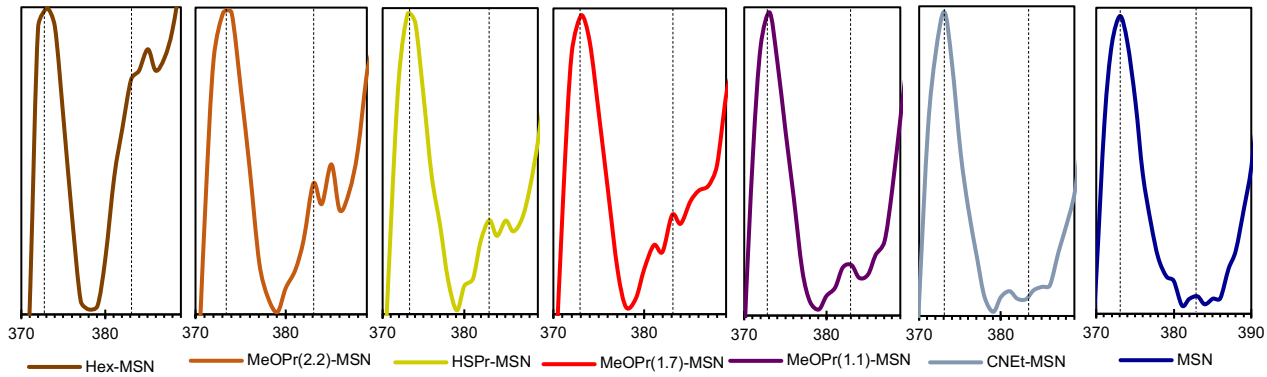

Figure S10. Fluorescence spectra of pyrene in different MSNs showing the changes in relative intensities between the first (373 nm)

References

1. a) D. Kim, J. Joo, Y. Pan, A. Boarino, Y. W. Jun, K. H. Ahn, B. Arkles, M. J. Sailor, Angew. Chem. Int. Ed. 2016, 55, 6423-6427; b) E. J. Anglin, L. Cheng, W. R. Freeman, M. J. Sailor, Adv. Drug Del. Rev. 2008, 60, 1266-1277; c) C. Liang, Z. Li, S. Dai, Angew. Chem. Int. Ed. 2008, 47, 3696-3717; d) A. Corma, Chem. Rev. 1997, 97, 2373-2420; e) I. I. Slowing, J. L. Vivero-Escoto, B. G. Trewyn, V. S.-Y. Lin, J. Mater. Chem. 2010, 20, 7924 - 7937; f) H. Furukawa, K. E. Cordova, M. O'Keeffe, O. M. Yaghi, Science 2013, 341; g) N. Mizoshita, T. Tani, S. Inagaki, Chem. Soc. Rev. 2011, 40, 789-800; h) A. Stein, Z. Wang, M. A. Fierke, Adv. Mater. 2009, 21, 265-293.

2. J. C. Doadrio, E. M. B. Sousa, I. Izquierdo-Barba, A. L. Doadrio, J. Perez-Pariente, M. Vallet-Regi, J. Mater. Chem. 2006, 16, 462-466.

3. L. E. Santos-Figueroa, C. Giménez, A. Agostini, E. Aznar, M. D. Marcos, F. Sancenón, R. Martínez-Máñez, P. Amorós, Angew. Chem. Int. Ed. 2013, 52, 13712-13716.

4. B. Karimi, M. Khorasani, ACS Catal. 2013, 3, 1657-1664.

5. a) A. Bibby, L. Mercier, Green Chem. 2003, 5, 15-19; b) D. Zareyee, H. Alizadeh, RSC Adv. 2014, 4, 37941-37946; c) K. Sarkar, Y. Salinas, I. Campos, R. Martínez-Máñez, M. D. Marcos, F. Sancenón, P. Amorós, ChemPlusChem 2013, 78, 684-694; d) J. Liu, S. Y. Bai, Q. R. Jin, H. Zhong, C. Li, Q. H. Yang, Langmuir 2012, 28, 9788-9796; e) T. Sakamoto, C. Pac, Tetrahedron Lett. 2000, 41, 10009-10012; f) K. Kandel, C. Frederickson, E. A. Smith, Y.-J. Lee, I. I. Slowing, ACS Catal. 2013, 3, 2750-2758; g) M. P. Kapoor, Y. Kasama, M. Yanagi, T. Yokoyama, S. Inagaki, T. Shimada, H. Nanbu, L. R. Juneja, Microporous Mesoporous Mater. 2007, 101, 231-239.

6. J. D. Bass, A. Solovyov, A. J. Pascall, A. Katz, J. Am. Chem. Soc. 2006, 128, 3737-3747.

7. a) C. Reichardt, Org. Process Res. Dev. 2007, 11, 105-113; b) C. Reichardt, Solvents and Solvent Effects in Organic Chemistry, 3 ed., Wiley-VCH, Weinheim, 2003.

8. S. Huh, J. W. Wiench, J.-C. Yoo, M. Pruski, V. S. Y. Lin, Chem. Mater. 2003, 15, 4247-4256.

9. a) G. Weber, F. J. Farris, Biochem. 1979, 18, 3075-3078; b) F. M. Cerezo, S. C. Rocafort, P. S. Sierra, F. García-Blanco, C. D. Oliva, J. C. Sierra, Helv. Chim. Acta 2001, 84, 3306-3312; c) J. Catalan, P. Perez, J. Laynez, F. G. Blanco, J Fluoresc 1991, 1, 215-223.

10. G. S. Loving, M. Sainlos, B. Imperiali, Trends Biotechnol. 2010, 28, 73-83.

11. a) P. Ugliengo, M. Sodupe, F. Musso, I. J. Bush, R. Orlando, R. Dovesi, Adv. Mater. 12. J. R. Shoemaker, M. S. Gordon, J. Phys. Chem. A 1999, 103, 3245-3251.

13. N. Sarkar, K. Das, D. N. Nath, K. Bhattacharyya, Langmuir 1994, 10, 326-329.

14. a) K. Kalyanasundaram, J. K. Thomas, J. Am. Chem. Soc. 1977, 99, 2039-2044; b) F. M. Winnik, Chem. Rev. 1993, 93, 587-614; c) A. Nakajima, Spectrochim. Acta A 1982, 38, 693-695; dD. C. Dong, M. A. Winnik, Photochem. Photobiol. 1982, 35, 17-21.

15. a) N. Wang, R. Liu, J. Chen, X. Liang, Chem. Commun. 2005, 5322-5324; b) L. Wang, J. Li, X. Zhao, Y. Lv, H. Zhang, S. Gao, Tetrahedron 2013, 69, 6041-6045.

16. Y.-X. Chen, L.-F. Qian, W. Zhang, B. Han, Angew. Chem. 2008, 120, 9470-9473.

17. a) W. F. Bailey, J. M. Bobbitt, K. B. Wiberg, J. Org. Chem. 2007, 72, 4504-4509; b) T. A. Hamlin, C. B. Kelly, J. M. Ovian, R. J. Wiles, L. J. Tilley, N. E. Leadbeater, J. Org. Chem. 2015, 80, 8150-8167.

18. K. A. Cooper, M. L. Dhar, E. D. Hughes, C. K. Ingold, B. J. MacNulty, L. I. Woolf, J. Chem. Soc. 1948, 2043-2049.

19. a) R. A. Schoonheydt, B. M. Weckhuysen, Phys. Chem. Chem. Phys. 2009, 11, 2794-2798; b) R. A. Schoonheydt, W. De Wilde, F. Velghe, J. Phys. Chem. 1976, 80, 511-518; c) K. Kandel, S. M. Althaus, C. Peeraphatdit, T. Kobayashi, B. G. Trewyn, M. Pruski, I. I. Slowing, ACS Catal. 2013, 3, 265-271.

20. a) C. A. Schoenbaum, D. K. Schwartz, J. W. Medlin, Acc. Chem. Res. 2014, 47, 1438-1445; b) S. H. Pang, C. A. Schoenbaum, D. K. Schwartz, J. W. Medlin, Nat Commun 2013, 4.

CHAPTER 3. INTERFACIAL CONTROL OF CATALYTIC ACTIVITIES IN THE ALDOL CONDENSATION: COMBINING THE EFFECTS OF HYDROPHOBIC ENVIRONMENTS AND WATER

Reprinted with permission from *ACS Catal.* **2019,** *9* (6), 5574-5582.

Dilini Singappuli-Arachchige[1,2], Takeshi Kobayashi[1], Zhuoran Wang[1,2], Sadie J. Burkhow[1,2], Emily A. Smith[1,2], Marek Pruski[1,2], and Igor I. Slowing*[,1,2]

[1]US DOE Ames Laboratory, Ames, Iowa 50011, United States

[2]Department of Chemistry, Iowa State University, Ames, Iowa 50011, United States

Abstract

Aminopropyl-functionalized mesoporous silica nanoparticles (AP-MSN) catalyze aldol condensations. The activity of AP-MSN decreases with increasing solvent polarity due to the stabilization of ion pairs formed between acidic silanol groups and the amines, which ultimately decreases the number of catalytically active amine sites. However, the reaction in water is faster than expected on the basis of polarity, because water limits the formation of Schiff bases that are also responsible for blocking active sites. In this work, we combined the action of water with a low-local-polarity environment around the catalytic sites of AP-MSN to maximize active site availability and catalyst performance. We specifically demonstrate how the local polarity of AP-MSN can be controlled by modifying its surface with varying concentrations of hexyl groups and how the dielectric constant of the silica−water interface can be determined using the solvatochromic probe Prodan. The catalytic activities of hexyl-modified AP-MSN in water were inversely proportional to their interfacial dielectric constants and were significantly higher (roughly by a factor of 4) than those of AP-MSN in anhydrous solvents of comparable polarities. Producing low-local-polarity environments in aqueous AP-MSN also enhanced the sensitivity of

the aldol reaction to the electronic effects of substituents in the substrate. The enhancement of catalytic activity by low interfacial polarity was also observed in other amine-catalyzed C−C bond forming reactions such as the Henry and vinylogous aldol reactions. Overall, our results demonstrate that the catalytic activity of AP-MSN can be controlled by the synergistic action of water and a low interfacial dielectric constant.

Introduction

The effects of solvents on homogeneous catalytic reactions have been studied extensively.[1−7] In contrast, our understanding of solvent effects in heterogeneous catalysis remains fairly limited.[8−19] Examining the influence of solvents on heterogeneous reactions is complicated due to interfacial interactions,[15] competitive adsorption,[16] fractional solvation of adsorbed species,[10,17] and mass transfer kinetics.[20] Understanding the interplay among these factors is fundamental for the rational design of interfacial catalysts.

The study of interfacial catalysis can be simplified using benchmark reactions with mechanisms that are well understood in solution. A reaction that has been extensively used for this purpose is the aldol condensation.[19,21−29] This reaction has been recently included in the design of many biomassprocessing schemes,[30−36] and its study has provided clear examples of complex behaviors, such as acid−base cooperativity. Several groups have investigated the effects of different types of acidic sites on the activity of immobilized base catalysts, demonstrating that cooperativity is affected by the strength, relative position, and structure of acid and base functionalities.[19,21−29,37] Additional studies have shown the role of properties more relevant to interfacial interactions such as the effects of support hydrophobicity[24,38−40] and solvents on the reaction.[18,19,41−43] For example, it has been shown that the catalytic activity of amine-functionalized mesoporous silicas decreases with increasing solvent polarity.[18,19] This drop in activity has been attributed to the increasing stabilization of ion pairs formed between acidic groups and amines that

blocks a fraction of the active sites by turning them into nonnucleophilic ammonium cations.[18,19,44] Interestingly, in spite of its high dielectric constant, water deviates from this trend: the catalytic activity of primary amines is higher in water than in methanol.[18,19] This anomalous behavior has been explained by the role of water in limiting competing reactions such as the formation of the non-enolizable Schiff base 1 (pathway a, Scheme 1)[18,29] and the conjugated dehydration product 2 (pathway b, Scheme 1)[43] that deactivate another fraction of the active amine sites. In addition, water is required for the hydrolytic desorption of the product in the last step of the reaction (step c, Scheme 1), which drives the equilibrium toward completion.[18]

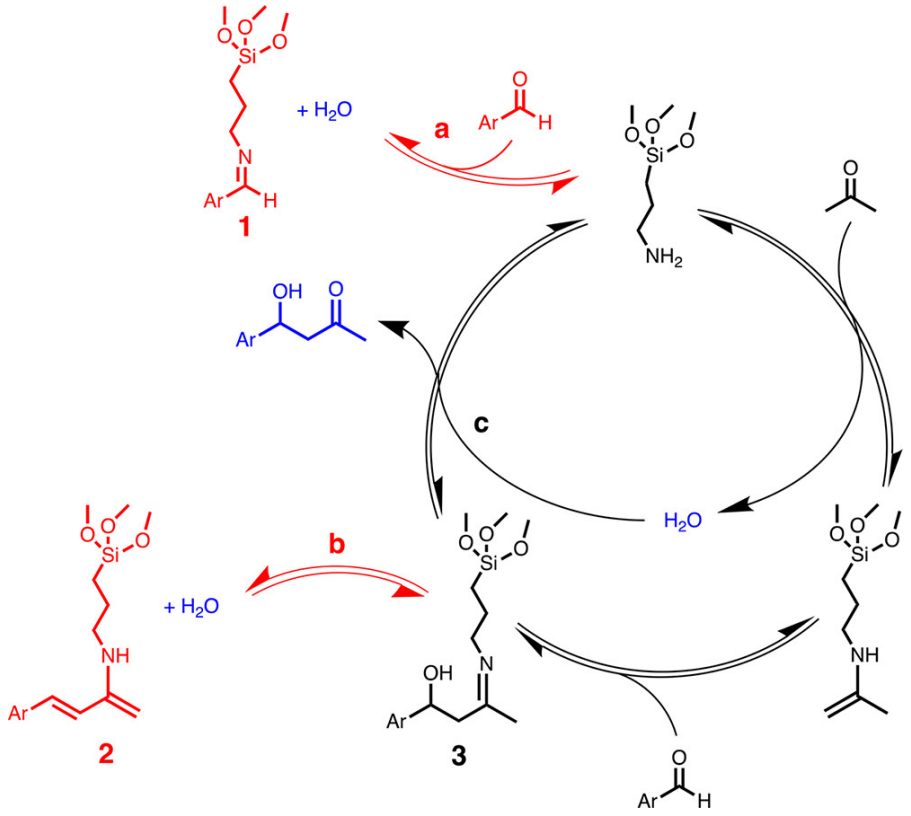

Scheme 1. Proposed Cycle of the Aldol Reaction between p-Nitrobenzaldehyde and Acetone Catalyzed by 3-Aminopropyl-Functionalized Mesoporous Silica Nanoparticles (AP-MSN): Main Reaction (Black) and Possible Inhibitory Pathways (Red)a (aAr = p-nitrophenyl).

On the basis of these observations, we hypothesized that the catalytic performance of amines on silica could be enhanced by combining the effects of water and a low-polarity environment around the active sites, i.e., by simultaneously decreasing the number of sites deactivated through formation of Schiff bases and ammonium ions. We have recently used solvatochromic probes to measure the dielectric properties of water−silica interfaces and demonstrated that organo-functionalization of the surface produces local environments with polarities which differ from that of the bulk solvent.[45] Our measurements and DFT calculations suggested that molecular guests located at the interface between water and organo-functionalized silica are indeed simultaneously surrounded by the tethered organic groups and water molecules.[45] This results in a mixed-solvation environment where the layer close to the silica surface has a lower polarity than the aqueous layer above it. Herein, we report the effects of organo-functionalization of aminopropyl mesoporous silica on its catalytic performance for the aldol condensation in water. We synthesized a series of hexylmodified 3-aminopropyl-functionalized mesoporous silica nanoparticles (Hex-AP-MSN) and used them as catalysts for the cross-aldol reaction between p-nitrobenzaldehyde and acetone in water. We examined the effect of hexyl group loading on the dielectric properties of the interface and the rate of the catalytic conversion and compared their activity with that of 3-aminopropyl mesoporous silica nanoparticles (APMSN) without any hexyl modification in water and in anhydrous solvents of varying dielectric constant.

Results and Discussion

First, we tested the catalytic activity of vacuum-dried AP-MSN (0.07 ± 0.02 mmol aminopropyl/g) for the cross-aldol condensation between p-nitrobenzaldehyde and excess acetone (Scheme 2) in anhydrous methanol, 1-propanol, and water. Consistent with previous reports, AP-MSN showed low catalytic activity in methanol (TOF 0.43 ± 0.02 h−1 , dielectric

constant ε 32.6; Figure 1), likely due to the solvent stabilization of non-nucleophilic ammonium−silanoxy ion pairs and formation of inhibited states 1 and 2 (Scheme 3, case I).[18,19]

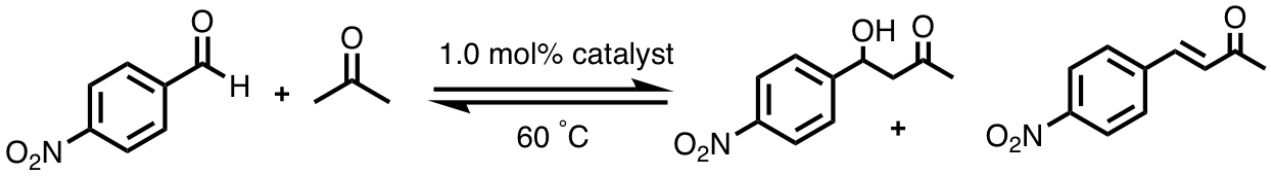

Scheme 2. Cross-Aldol Condensation between p-Nitrobenzaldehyde and Acetone.

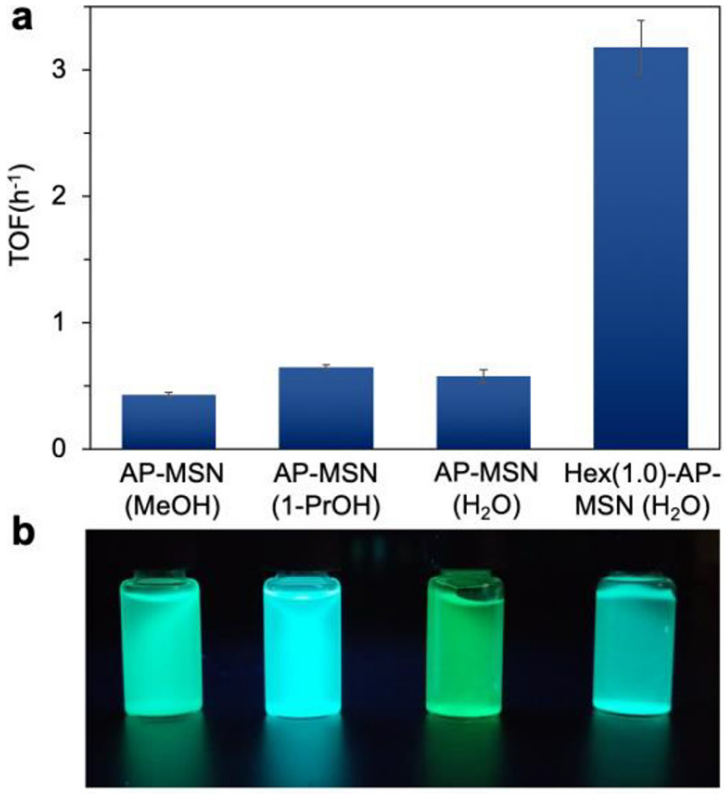

Figure 1. (a) Catalytic activities of AP-MSN in different solvents and Hex(1.0)-AP-MSN in water for the aldol reaction between p-nitrobenzaldehyde and acetone (1.0 mol % AP, 60 °C). (b) Suspensions of the Prodan-loaded materials in the solvents (corresponding to the materials and solvents in (a)) under a 355 nm lamp. The color of the fluorescent emission is indicative of the dielectric constant (ε).

Replacing methanol with the less polar 1-propanol (ε 20.1) led to a ca. 50% enhancement in AP-MSN activity (TOF 0.65 ± 0.02 h−1), suggesting that destabilization of protonated amines by

decreasing solvent polarity increases the number of active nucleophilic sites, even though the persistence of inhibition products 1 and 2 prevents a further increase in reactivity (Scheme 3, case II).[18] Use of water as a solvent led to an AP-MSN activity (TOF 0.58 ± 0.05 h−1) higher than that in methanol but slightly lower than that in propanol, suggesting that the role of water in the hydrolysis of inhibited states 1 and 2 is more significant than its dielectric stabilization of the protonated ammonium ions (Scheme 3, case III).[18,19,43]

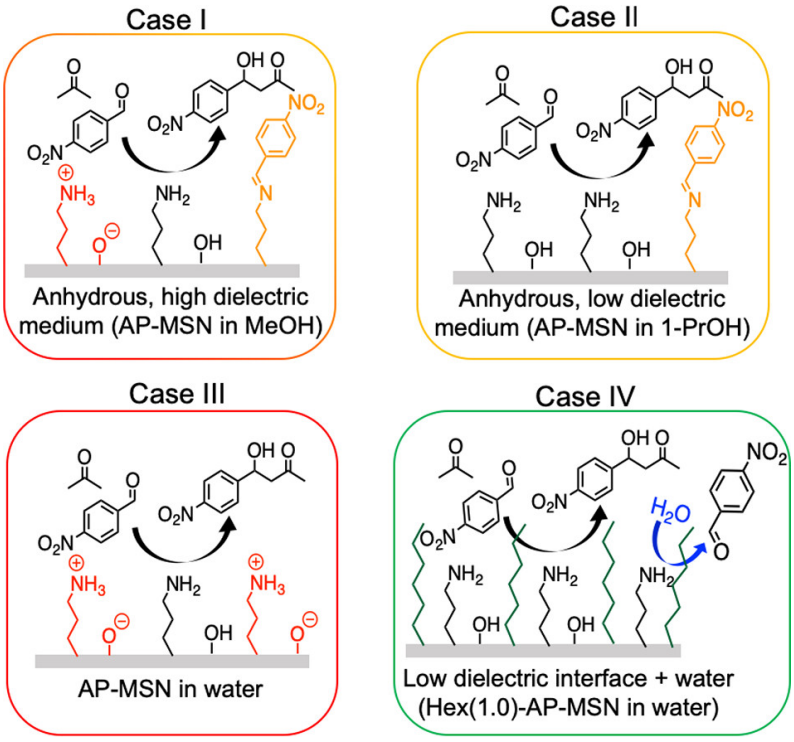

Scheme 3. Species Likely Present at the AP-MSN–Solvent and Hex(1.0)-AP-MSN–Water Interfaces.

These results indicate that AP-MSN catalytic activity can be improved either by decreasing the dielectric constant of the solvent or by utilizing the hydrolytic action of water. Attempts to combine both effects using a 1-propanol/ water mixture failed to further increase the activity, giving a rate lower than those of the pure solvents (TOF 0.44 ± 0.01 h−1). The lack of activity enhancement in the solvent mixture was likely due to its high dielectric constant (ε

44).[46,47] Thus, to effectively combine the hydrolytic effect of water with the destabilization of ammonium−silanoxy pairs, it is necessary to prevent water from significantly increasing the dielectric constant at the reaction site.

We clarify that the TOF values are calculated on the basis of the amine content of the original catalysts as measured by reaction with ninhydrin.[48,49] Because both inhibitory processes (formation of ammonium−silanoxy ion pairs and products 1 and 2) imply deactivation of a fraction of the amine groups, the variations in TOF should account for the differences in number of free active sites that result from these inhibitory mechanisms.

An alternate way to control the dielectric properties around a supported active site is to immobilize organic groups next to it.[9,50] Because the tethered organic groups can interfere with solvation at the solid−water boundary, the dielectric properties of the interface can be decoupled from those of the bulk solvent, resulting in a lower local polarity.45 Following this idea, we synthesized a new catalyst by incorporating hexyltrimethoxysilane along with 3-aminopropyltrimethoxysilane in MSN. Amine quantification by reaction with ninhydrin combined with elemental (CHN) analysis of the material indicated aminopropyl and hexyl group loadings of 0.06 ± 0.01 and 1.02 ± 0.02 mmol/g, respectively (Table S1). The new catalyst was designated Hex(1.0)-AP-MSN.

To measure the effective dielectric constant of the catalyst− water interface, we used the fluorescent solvatochromic probe Prodan.[51−53] Because of its zwitterionic structure, the stability of Prodan's excited state is greatly affected by the dielectric properties of its environment.[45] This results in a dependence of the probe's Stokes shift on the dielectric constant of the solvent (Figure S1). Impregnation of the probe on Hex(1.0)- AP-MSN followed by suspension in water and fluorescence spectroscopy analysis resulted in a Stokes shift of 151.0 ± 0.6 nm, which, on

the basis of the solvent calibration (eq S1), corresponded to an interfacial dielectric constant (εi) of 21.6 ± 0.5. Note that because the probe remains adsorbed on the surface without leaching out to the solvent, it must directly reflect the dielectric properties of the interface. Importantly, the interfacial dielectric constant of Hex(1.0)-AP-MSN in water was significantly lower than that measured for AP-MSN in the same solvent (εi 74.8 ± 0.8; Figure 1b) and was very close to the dielectric constant of 1-propanol (ε 20.1).[47]

Remarkably, the catalytic activity of Hex(1.0)-AP-MSN for the reaction in water (TOF 3.2 ± 0.2 h−1) was about 5 times higher than those of AP-MSN in water or 1-propanol. These results suggest that the combination of a low dielectric environment around the active sites due to the hexyl groups and the availability of water at the interface decreases the extent of catalyst deactivation by species such as Schiff base 1 (Scheme 3, case IV). The coexistence of water and hexyl groups on the surface of Hex(1.0)-AP-MSN was evidenced by exposing a vacuum-dried sample to ambient humidity and acquiring its 1 H solid state (SS)NMR (Figure S2). In addition to the signals corresponding to the hexyl and amine groups, the spectrum presents two resonances at 4.8 and 4.0 ppm attributed to weakly adsorbed water and rapidly exchanging SiOH−(H2O)n species, respectively.[54,55]

Elemental analysis of the spent and washed AP-MSN after the reaction in 1-propanol and Hex(1.0)-AP-MSN after the reaction in water indicated increases in N content of 78% and 56%, respectively. In addition, the spent AP-MSN changed in color from the original white to yellow (Figure S3), which may be indicative of the inhibitory Schiff base 1.[18,29,43] In contrast, Hex(1.0)-AP-MSN retained its white color after reaction in water. Whereas these observations suggest formation of imine intermediate 1, analyses by dynamic nuclear polarization (DNP) enhanced ^{13}C SSNMR, Raman, and FTIR spectroscopy (Figures S4−S7) could not distinghuish this species

from the potentially physisorbed p-nitrobenzaldehyde substrate. All of the collected spectra indicate the presence of aromatic species in the spent catalysts; however, the observed signals could be assigned to either the starting p-nitrobenzaldehyde or the hypothetical Schiff base intermediate 1. While signals specific to the intermediate 1 can be observed by SSNMR at much higher AP loadings (1 mmol/g),[18,29,43] the low active site loadings in this study (ca. 0.06 mmol/g) prevented unequivocal identification of the molecules. Importantly, however, amine quantification with ninhydrin indicated that the spent AP-MSN after reaction in 1-propanol had 0.03 mmol/g of available sites (i.e., a ca. 60% loss of active sites), while the spent Hex(1.0)-AP-MSN after reaction in water retained 0.04 mmol sites/g (a 33% loss after reaction). This result confirms that both catalysts are partially poisoned during the reaction but that the combination of hexyl groups and interfacial water decreased the extent of deactivation. Recycling of both catalysts indicated a steady drop in activity over four cycles, with Hex(1.0)-AP-MSN in water giving always higher product yields in comparison to AP-MSN in 1-propanol (Figure S8).

The dependence of the AP-MSN-catalyzed reaction on the polarity of the medium can be analyzed following the Eyring− Laidler formalism for reactions involving dipoles. According to this model, the logarithm of the rate constant has a linear dependence on the reciprocal of the medium's ε value (eq S2).[1,56–59] Consistent with this theory, the AP-MSN-catalyzed aldol reaction in different solvents shows a linear relationship between the log(TOF) and the inverse of the solvents' ε value (Figure 2, red squares and Table S2 and Figure S9). The positive slope of the correlation likely reflects the increasing availability of nucleophilic amine groups with decreasing ε, because higher ε media should increase the extent of amine protonation and thereby decrease the rate of the aldol pathway (Scheme 3, case I). This dependence should also be valid for the interfacial dielectric constant (εi) of hexyl-substituted APMSN in water. To examine this

hypothesis, we synthesized additional bifunctional Hex-AP-MSN materials loaded with amounts of 3-aminopropyl groups similar to those before (0.06−0.07 mmol/g) but varying amounts of hexyl groups (Hex(0.5)-AP-MSN, Hex(0.7)-AP-MSN, and Hex(0.9)-APMSN). The hexyl groups were incorporated in 10-fold excess with respect to the amines to ensure they could affect the solvation environment of the active sites. Again, group loadings were measured by a combination of elemental (CHN) analysis and amine quantification via reaction with ninhydrin (Table S1). Because silanol groups participate in the reaction as cooperative partners of the amines, they were also quantified by ^{29}Si DP MAS SSNMR.[60] The analysis indicated that all the materials had similar amounts of silanols (Figure S10), more than enough to ensure effective cooperativity with the catalytic amines.[25] Nitrogen physisorption and powder X-ray diffraction analyses of the samples showed that the organic groups had no significant effects on the textural properties and pore structure of the materials (Table S3 and Figure S11). The εi values of the materials suspended in water were obtained by fluorescence spectroscopy analysis of adsorbed Prodan. The εi values decreased with the hexyl group loadings of the materials, confirming that interfacial polarity can be fine-tuned via surface functionalization (Table S3 and Figure S12).[45]

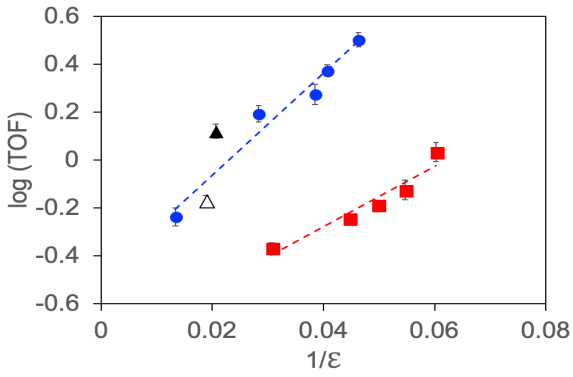

Figure 2. Variation of log(TOF) of the aldol reaction between p-nitrobenzaldehyde and acetone with the reciprocal of the dielectric constant of Hex-AP-MSN having different hexyl group loadings in water (blue circles), MeOP-AP-MSN in water (black triangle), CNEt-AP-MSN in water (white triangle), and AP-MSN in anhydrous solvents (red squares) (1.0 mol % AP, 60 °C).

The reaction was then performed in water using the hexyl functionalized materials as catalysts. The catalytic activities of the Hex-AP-MSN varied significantly, despite all reactions being conducted in water under the same conditions. Moreover, the dependence of the catalytic activity on the interfacial dielectric constant shows a trend analogous to that of AP-MSN in water-free solvents, i.e., the log(TOF) increased as a function of 1/εi (Figure 2, blue circles, and Table S4 and Figure S13). Three important features can be observed here. First, the activities of the Hex-AP-MSN catalysts used in water were significantly higher than those of AP-MSN in water-free solvents with comparable ε values. This upward shift in activity is likely due to the presence of water at the interface, which improves the reactivity as described above. Second, the reactions performed in aqueous media (blue) displayed a higher rate sensitivity to changes in polarity in comparison to those performed in water-free media (red), as indicated by the difference in the slopes of their 1/ε−log(TOF) linear correlations (21.3 for aqueous versus 12.6 for water-free reactions). This difference in sensitivity indicates that the effect of water on the reaction is more important at low interfacial polarities in comparison to that when the local environment is highly polar. Finally, the nonzero slope of the aqueous HexAP-MSN-catalyzed reactions confirms that the dielectric properties at the active site differ from those of the bulk solvent and are controlled by the organic functionalities.

An alternative explanation to the increase in activity of APMSN with hexyl loading could be the steric destabilization of bulky species such as 1 and 2 by the long hydrocarbon chains. To examine this possibility, we synthesized 3-methoxypropyland 2-cyanoethyl-modified AP-MSN (MeOP-AP-MSN, 1.25 ± 0.01 mmol methoxypropyl/g; CNEt-AP-MSN, 0.90 ± 0.01 mmol cyanoethyl/g) with AP loadings similar to those for the Hex-AP-MSN materials (0.05 ± 0.01 and 0.07 ± 0.02 mmol/g, respectively). Fluorescence spectroscopy measurements with adsorbed

Prodan indicated that the materials had interfacial dielectric constants (εi 49 ± 1, MeOP-AP-MSN; εi 53 ± 1, CNEt-AP-MSN) between those of AP-MSN (74.8 ± 0.8) and Hex-AP-MSN (<35), which is consistent with the higher polarity of methyl ether and nitrile groups in comparison to the hexyl chain. In spite of the presence of a large amount of organic groups on the surface, the TOF of the aldol reaction using these materials in water were between those of AP-MSN and the Hex-AP-MSN (1.32 ± 0.09 h−1 , MeO-AP-MSN; 0.68 ± 0.03 h−1 , CNEt-AP-MSN). This result indicates that the effect of the organic groups on the catalytic activity of the materials was not due to sterics but likely due to the differences in the dielectric properties of the interfaces. Importantly, the activities of both MeOP-AP-MSN and CNEt-AP-MSN fit in the 1/ε−log(TOF) trend for aqueous media (Figure 2, black and white triangles respectively).

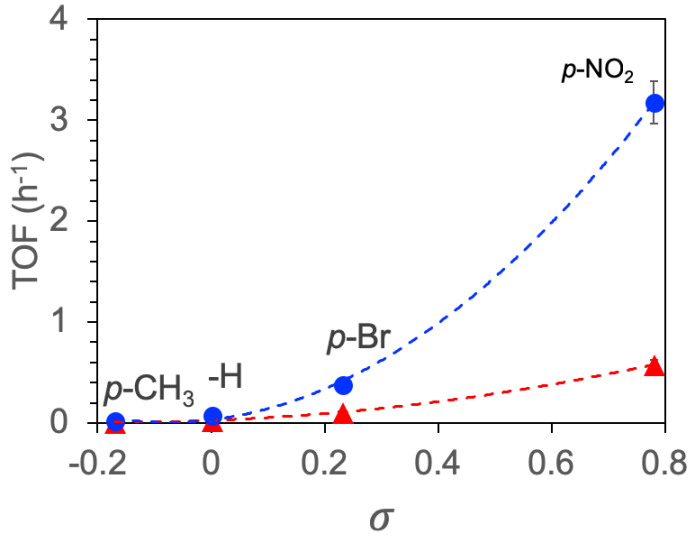

Figure 3. Hammett constants (σ) of para-substituted benzaldehydes versus the TOFs of their aldol reaction with acetone using Hex(1.0)-AP-MSN (blue circles) and AP-MSN (red triangles) as catalysts in water (1.0 mol % amine, 60 °C).

Hammett analysis of the reaction indicates a small difference in its sensitivity to the electronic effects of benzaldehyde substituents when Hex(1.0)-AP-MSN versus AP-MSN is used as a catalyst in water (Figures S13 and S14 and Table S5). The positive slope obtained with both

materials is consistent with previous reports[21] and suggests that there are no fundamental differences in the reaction mechanism using these catalysts. The positive slope is indicative of a negative charge buildup in the transition state of the rate-limiting step. This step has been proposed as the nucleophilic attack of the enamine on the benzaldehyde carbonyl (bottom of catalytic cycle in Scheme 1).[21,23,25,26] Electron-withdrawing groups lower the activation barrier by decreasing the negative charge density at the reaction center. This effect is more relevant in nonpolar environments because they have less capacity to stabilize charges in comparison to high-dielectric media. This was recognized in the initial work by Hammett, when he showed that the reaction constant (ρ) is inversely proportional to the dielectric constant of the media (eqs S3 and S4).61 Thus, the slightly larger slope in the Hammett plot for Hex(1.0)-APMSN than for AP-MSN in water (Figure S14) is consistent with the lower εi of the former. The difference in substituent sensitivities between the two catalysts appears small in the Hammett plot because it is based on the logarithm of the TOF ratios of substituted and nonsubstituted benzaldehyde; however, it becomes more obvious in direct comparisons of the substrates' TOFs (Figure 3).

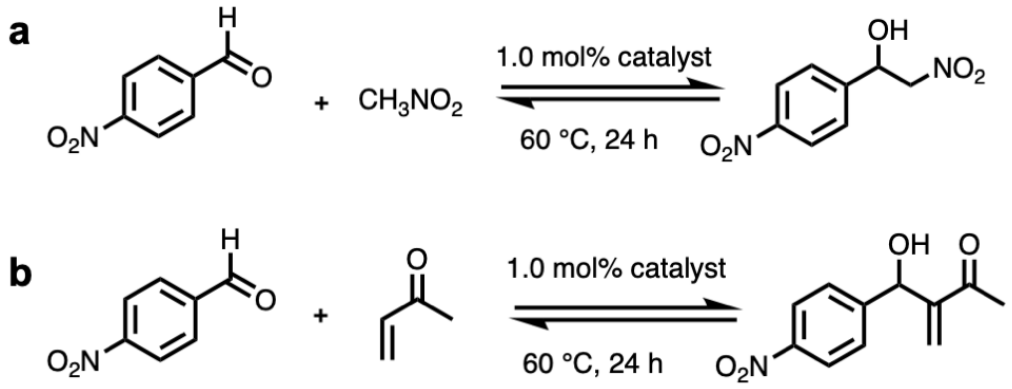

Scheme 4. (a) Henry Reaction between p-Nitrobenzaldehyde and Nitromethane and (b) Vinylogous Aldol Reaction between p-Nitrobenzaldyhde and 3-Buten-2-one

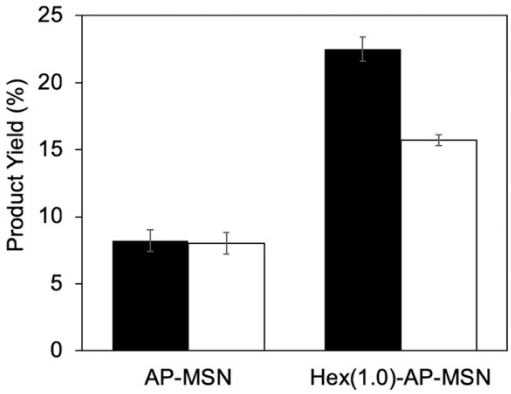

Figure 4. Differences in catalytic activities between aqueous AP-MSN and Hex(1.0)-AP-MSN for the Henry (black) and vinylogous aldol reactions (white ×100) (1.0 mol % amine, 24 h, 60 °C).

We also observed some variations in product selectivity as a function of hexyl substitution of the catalyst. Under all the conditions tested, the aldol product was favored over the enone regardless of the catalyst employed. It is known that the selectivity for enone is typically favored by increasing reaction temperatures.[34] On the basis of the reaction equilibrium, one could also expect that the presence of anhydrous media would give higher enone selectivity in comparison to water. Indeed, while all the AP-MSN-catalyzed reactions run in anhydrous solvents showed enone selectivities between 19 and 28%, the reaction conducted in water with the same catalyst gave lower aldol product (5%) (Table S2). Reactions with hexylsubstituted catalysts in water also showed lower enone selectivities (3−4%) (Table S4).

Overall, our results suggest that lowering the interfacial polarity of aqueous AP-MSN enhances its catalytic activity toward the aldol condensation because it increases the availability of the nucleophilic amines. On the basis of this postulate, the same approach should favor other reactions catalyzed by silica-supported amines. For example, Ballini and Bosica have reported that the amine-catalyzed Henry reaction (Scheme 4a) is improved when organic solvents are replaced with water.[62] While this reaction proceeds through a different mechanism than the aldol

condensation, the rate-limiting step requires the availability of free amines[21,62,63] and should therefore benefit from a lower interfacial polarity. To examine this hypothesis, we performed the Henry reaction between pnitrobenzaldehyde and nitromethane using aqueous Hex(1.0)- AP-MSN and AP-MSN as catalysts. Our measurements indicated that, indeed, the hexyl-modified catalyst was twice as active as AP-MSN (Figure 4, black bars), which is consistent with the proposed hypothesis. Similarly, the activity of aqueous Hex(1.0)-AP-MSN for the vinylogous aldol reaction between p-nitrobenzaldehyde and 3-buten-2-one (Scheme 4b)[64] was about 50% higher than that of AP-MSN (Figure 4, white bars), further supporting the idea that low interfacial polarity enhances the activity of these catalysts by increasing the availability of the amine active sites.

Materials and Methods

Materials

Hexadecyltrimethylammonium bromide (CTAB), p-nitrobenzaldehyde, dimethyl sulfone (DMS), methanol, N-(3-dimethylaminopropyl)-N′-ethylcarbodiimide hydrochloride, N-hydroxysuccinimide sodium salt, resorcinol, anhydrous 2-butanol, anhydrous 1-propanol, and ninhydrin were purchased from Sigma-Aldrich. p-Bromobenzaldehyde, pFigure 3. Hammett constants (σ) of para-substituted benzaldehydes versus the TOFs of their aldol reaction with acetone using Hex(1.0)- AP-MSN (blue circles) and AP-MSN (red triangles) as catalysts in water (1.0 mol % amine, 60 °C). Scheme 4. (a) Henry Reaction between pNitrobenzaldehyde and Nitromethane and (b) Vinylogous Aldol Reaction between p-Nitrobenzaldyhde and 3-Buten-2-one Figure 4. Differences in catalytic activities between aqueous AP-MSN and Hex(1.0)-AP-MSN for the Henry (black) and vinylogous aldol reactions (white ×100) (1.0 mol % amine, 24 h, 60 °C). ACS Catalysis Research Article DOI: 10.1021/acscatal.9b00195 ACS Catal. 2019, 9, 5574−5582 5578 tolualdehyde, benzaldehyde, 3-buten-2-one, and tetrakis- (trimethylsilyl)silane

(TTMS) were purchased from Aldrich. Tetraethyl orthosilicate (TEOS), 3-aminopropyltrimethoxysilane,3-methoxypropyltrimethoxysilane,and hexyltrimethoxysilane were purchased from Gelest, Inc. NaOH, concentrated HCl, 2-propanol, and acetone were purchased from Fisher Scientific. Ethanol was purchased from Decon Laboratories and Prodan from Anapec, Inc. Butylamine was purchased from Fluka. Methanol, ethanol, 2-propanol, and acetone were dried with CaH2 and distilled before use. All other reagents were used as received without further purification.

Synthesis of functionalized MSNs

CTAB (1.0 g, 2.74 mmol) was dissolved in deionized water (480 mL) in a roundbottom flask followed by addition of 2 M NaOH (3.5 mL, 7.0 mmol). The solution was stirred for 1 h at 80 °C. TEOS (5.0 mL, 22.6 mmol) and organosilanes (amounts according to Table S6) were then added dropwise over 7 min to the CTAB solution. Magnetic stirring was continued for another 2 h at 80 °C. The solution was filtered, washed with abundant water and methanol, respectively, and vacuum-dried overnight. The CTAB template was removed by refluxing 1.0 g of dry solid with 100 mL of methanol and concentrated HCl (0.8 mL, 9.7 mmol) at 60 °C for 6 h. The surfactant removal step was repeated one more time. The surfactant-removed samples were then filtered, washed with abundant methanol and water, and vacuum-dried at 100 °C overnight

Characterization of catalysts

XRD patterns were recorded on a Bruker X-ray diffractometer equipped with Cu Kα radiation (40 kV, 44 mA) over the range of 1−10° 2θ. The nitrogen adsorption/desorption isotherms were measured in a Micromeritics Tristar surface area and porosity analyzer. The surface areas and pore size distributions were calculated by the Brunauer−Emmett−Teller (BET) and Barrett−Joyner−Halenda (BJH) methods, respectively. Elemental analyses of the dry samples were done in triplicate on a PerkinElmer 2100 series II CHNS analyzer, using

acetanilide as a calibration standard and combustion and reduction temperatures of 925 and 640 °C, respectively.

Homogeneous synthesis of schiff-base intermediate (Analogous to Species 1 in Scheme 1)

p-Nitrobenzaldehyde (0.40 mmol) and butylamine (0.50 mmol) were mixed in methanol-d4 (1 mL) and stirred at 60 °C for 24 h. 1 H NMR (600 MHz, methanol-d4; δ, ppm): 8.46 (s,1H), 8.29 (d, J = 8.1 Hz, 2H), 7.96 (d, J = 8.1 Hz, 2H), 3.68 (td, J = 7.4 Hz, 1.49 Hz, 2H), 1.72 (m, 2H), 1.43 (m, 2H), 0.95 (t, 3H). 13C{1 H} NMR (600 MHz, methanol-d4; δ, ppm): 160.0, 149.0, 141.5, 128.6 (2C), 123.5 (2C), 60.8, 32.5, 20.0, 12.8.

Solid-state NMR

The concentrations of silanols in the MSN were determined by 29Si direct polarization magic-angle spinning (DPMAS) NMR spectroscopy.60 The 29Si DPMAS NMR spectra were acquired on an Agilent NMR spectrometer operated at 9.4 T, equipped with a Chemagnetics 5 mm MAS probe. The samples were packed in a zirconia MAS rotor and spun at 8 kHz. The 1 H spectrum of predried Hex(1.0)-APMSN was acquired at 14.1 T on a Varian NMR System 600 spectrometer, using a FastMAS 1.6 mm probe operated at 25 kHz. To characterize the spent catalysts, DNP-enhanced 13C{1 H} CPMAS experiments were carried out on a Bruker Avance III spectrometer operated at 9.4 T, equipped with a 3.2 mm cryoMAS probe and a 263 GHz gyrotron. The samples were mixed with 10 mM AMUPol dissolved in water, packed in a sapphire rotor, and spun at 7 kHz at 105 K. The experimental parameters used to acquire 29Si and 13C spectra are given in the captions to Figures S1 and S8 in the Supporting Information.

Raman spectroscopy

An XploRA Plus Raman confocal upright microscope with a Synapse EMCCD camera was used for all Raman measurements (HORIBA Scientific, Edison, NJ). A 785 nm solid state diode laser with a 26000 W/cm2 irradiance was used for the spent catalysts, and due to the strong

Raman scattering from p-nitrobenzaldehyde and the homogeneously synthesized intermediate, 3000 and 500 W/ cm2 irradiances were used, respectively. Raman data were collected in the epi-direction with a 20× magnification, a 0.4 numerical aperture objective, a 600 grooves/millimeter grating, a 200 μm monochromator slit, and a 500 μm confocal pinhole. The acquisition time was 50 s with three accumulations. To obtain a representative signal, three different sample areas were measured and averaged for the spectra shown within Figure S6.

FTIR spectroscopy

Diffuse reflectance infrared Fourier transform (DRIFT) measurements were made on a Bruker Vertex 80 FT-IR spectrometer equipped with a HeNe laser and photovoltaic MCT detector and OPUS software, to characterize the spent catalysts. Before measurements, samples were vacuum-dried overnight after a 24 h reaction. Then, they were mixed with KBr and finely ground to ensure a smooth surface in the sample chamber. p-Nitrobenzaldehyde and homogeneously synthesized intermediate were also analyzed in the same manner for comparison.

Active site quantification

Measurement of amine sites in the materials was performed using a modified ninhydrin method.48,49 Different AP-MSN samples (15.0 mg each) were suspended in absolute ethanol (3.0 mL). An aliquot (0.5 mL) of ninhydrin in EtOH (56 mM) solution was added to the suspension, and the mixture was heated for 10 min at 100 °C. After the samples were cooled for 5 min, the absorption of the resultant Ruheman's purple complex was measured at 588 nm in a microplate reader against a blank consisting of MSN (15.0 mg), absolute ethanol (3.0 mL), and ninhydrin solution (56 mM, 0.5 mL). Butylamine was used as a calibration standard for quantification purposes.

Fluorescence measurements of Prodan-loaded MSN samples

10.0 mg each) and ground. The mixture was left to dry and then suspended in water (2.0 mL). The suspensions were analyzed by fluorescence spectroscopy in a Cary Eclipse spectrophotometer. The excitation wavelength was set at 337 nm, and both excitation and emission slit widths were set at 5 nm. The fluorescence spectra were then fitted in OriginPro using a Gaussian distribution model. The maximum fluorescence emission wavelength of each sample was used to assign dielectric constants on the basis of probe fluorescence in reference solvents (Figure S1 and eq S1).45 To test if the dye was associated to the materials, the suspensions were centrifuged. Fluorescence spectroscopy analysis of the supernatants gave no signal, indicating the dye was not present in water. Resuspension of the solids in fresh water restored the signal, indicating the dye remained associated to the MSN.

Aldol reaction between para-substituted benzaldehydes and acetone

Para-substituted benzaldehydes (0.20 mmol) were dissolved in excess acetone (1.5 mL, 20 mmol), followed by the addition of a suspension of functionalized APMSN (35−38 mg, corresponding to 1.0 mol % amine based on the aldehyde substrate) in the corresponding solvent (1.5 mL). The solution was stirred for different amounts of time ranging from 2 to 75 h at 60 °C. Reactions for p-tolualdehyde and benzaldehyde were performed using twice the amount of reactants. The reaction mixtures were quenched with ice and centrifuged; the supernatant was then concentrated under reduced pressure in a rotary evaporator. The products were redissolved in CDCl3 and quantified by 1 H NMR using DMS or TTMS as the internal standards. All mass balances were 100% ± 10%. Because of their lower boiling points, the reactions using ptolualdehyde and benzaldehyde were also analyzed by GC-MS, to verify the mass balance. These samples were centrifuged, and an aliquot (0.200 mL) was diluted in ethanol (1.0 mL) and analyzed in an Agilent GC-MS instrument (7890A, 5975C) with a HP-5MS column, with

resorcinol as the internal standard. TOFs were calculated from the slope of the kinetic plots (time versus turnover number). The turnover number was defined as mmol of product divided by mmol of aminopropyl groups in the reaction system (based on ninhydrin quantification). Selectivities were calculated as 100% times the mmol of each product divided by the mmol of the sum of the products at the longest time of sampling

Henry reaction between p-nitrobenzaldehyde and nitromethane

p-Nitrobenzaldehyde (30 mg, 0.20 mmol) was dissolved in excess nitromethane (1.5 mL, 28 mmol), followed by the addition of a suspension of functionalized MSN (35 mg, 1.0 mol % AP) in water (1.5 mL). The solution was stirred for 24 h at 60 °C. The reaction mixture was quenched with ice and centrifuged; the supernatant was then concentrated under reduced pressure. The products were quantified by 1 H NMR using TTMS as the internal standard. Vinylogous Aldol Reaction between p-Nitrobenzaldehyde and 3-Buten-2-one. p-Nitrobenzaldehyde (30 mg, 0.20 mmol) and 3-buten-2-one (16.2 μL, 0.20 mmol) were added to a a suspension of functionalized MSN (35 mg, 1.0 mol % AP) in water (3 mL). The solution was stirred for 24 h at 60 °C. The reaction mixture was quenched with ice and centrifuged; the supernatant was then concentrated under reduced pressure. The products were quantified by 1 H NMR using DMS as the internal standard.

Conclusions

This work demonstrates that nonpolar and aqueous media can be combined in interfacial systems to enhance the performance of supported catalysts. The activity of the AP-MSN-catalyzed aldol reaction can be improved by both (1) low-polarity media because they disfavor silanol-mediated amine protonation and (2) water because it destabilizes inhibitory pathways. The synergistic combination of low-polarity local environments and water can be achieved by introducing alkyl groups along with the catalyst on MSN and suspending the composite in water.

The dielectric constant at the MSN−water interface (ε_i) can be determined by fluorescence spectroscopy using solvatochromic probes such as Prodan and calibrating the fluorescence with standard solvents. The ε_i of Hex-AP-MSN in water is directly proportional to the surface density of alkyl groups. Decreasing the ε_i of aqueous Hex-AP-MSN leads to enhancements in the TOF of the aldol reaction comparable to those on decreasing the ε of the solvent; however, for a given ε_i or ε the aqueous reaction is about 4 times faster than the reaction using anhydrous alcohols as solvents. Decreasing the ε_i of Hex-AP-MSN in water enhances the sensitivity of the aldol reaction to substituent effects, as probed by studying the Hammett linear structure−activity relationships of the system. Electron-withdrawing groups particularly enhance the activity of Hex-AP-MSN for this reaction because they disperse the charge density in the transition state of the rate-limiting step, compensating for the inability of the low-polarity media to stabilize charges. Understanding the role of local environment on the catalysis of the aldol reaction enables controlling other amine-mediated transformations, as demonstrated by the higher activity of aqueous Hex-AP-MSN in comparison to AP-MSN in the Henry and vinylogous aldol reactions. Ultimately, controlling the interfacial dielectric properties of heterogeneous catalysts will enable designing advanced systems that replace nonpolar organic solvents with water, an economical and an environmentally friendly solvent.

Acknowledgements

This research was supported by the U.S. Department of Energy, Office of Basic Energy Sciences, Division of Chemical Sciences, Geosciences, and Biosciences, through the Ames Laboratory Catalysis Science program. The Ames Laboratory is operated for the U.S. Department of Energy by Iowa State University under Contract No. DE-AC02-07CH11358.

Supplemental Tables and Figures

Table S1. Concentrations of surface species on MSN samples.

Sample	AP[a] (mmol/g)	Organic gorup[b] (mmol/g)
AP-MSN	0.07 ± 0.02	-
Hex(0.5)-AP-MSN	0.07 ± 0.03	0.48 ± 0.01
Hex(0.7)-AP-MSN	0.07 ± 0.01	0.74 ± 0.05
Hex(0.9)-AP-MSN	0.07 ± 0.02	0.94 ± 0.01
Hex(1.0)-AP-MSN	0.06 ± 0.01	1.02 ± 0.02
MeOP-AP-MSN	0.05 ± 0.01	1.25 ± 0.01
CNEt-AP-MSN	0.07 ± 0.02	0.90 ± 0.01

a)From quantification by reaction with ninhydrin.
b)Calculated as a difference between AP concentration obtained from ninhydrin quantification and total organics obtained from elemental analysis.

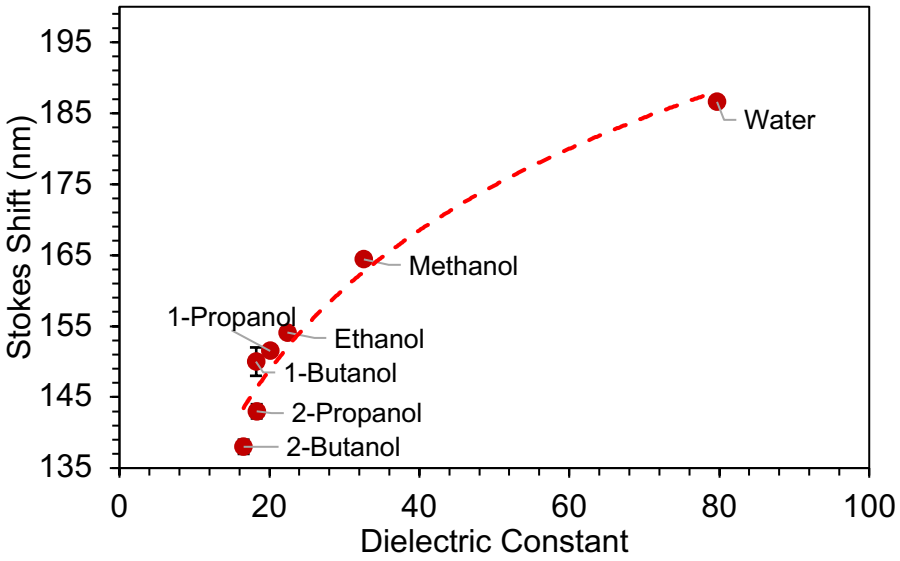

Figure S1. Stokes shifts of Prodan in pure solvents of varying dielectric constants (ε values from Smallwood, I., *Handbook of Organic Solvent Properties*. Elsevier: Burlington, 1996).

Equation S1. Correlation between Prodan's Stokes shift and solvent dielectric constants.

$$Stokes\ Shift = 28.4 \ln(\varepsilon) + 63.7$$

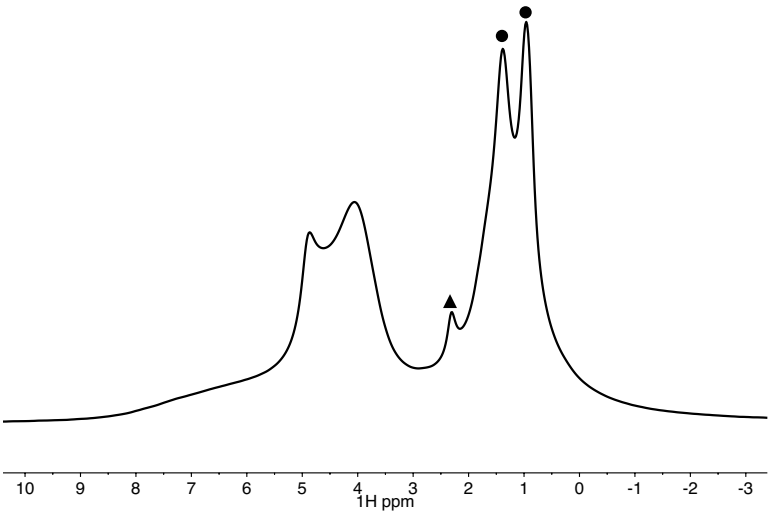

Figure S2. 1H SS NMR spectrum of pre-dried Hex(1.0)-AP-MSN and then exposed to ambient humidity. Signals at 0.9 and 1.4 ppm are assigned to protons in hexyl group (black circles), aminopropyl protons on the alpha carbon can be observed at 2.3 (black triangle) while the other protons overlap with those of hexyl. Peaks at 4.8 and 4.0 ppm correspond to weakly adsorbed water and rapidly exchanging SiOH-(H2O)n species, respectively.[1]

[1]Trébosc, J.; Wiench, J. W.; Huh, S.; Lin, V. S. Y.; Pruski, M., J. Am. Chem. Soc. 2005, 127, 3057-3068.

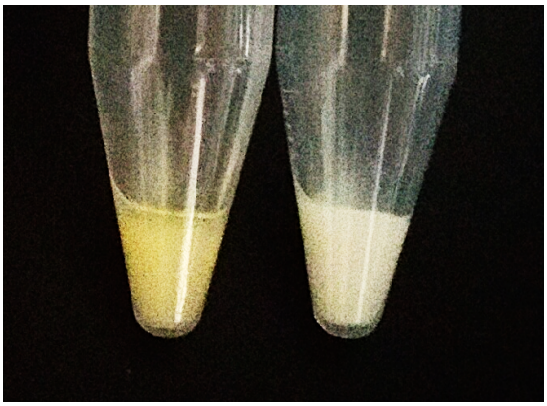

Figure S3. Photographs of the spent AP-MSN (left) and Hex(1.0)-AP-MSN (right) catalysts after reaction in 1-propanol and water, respectively.

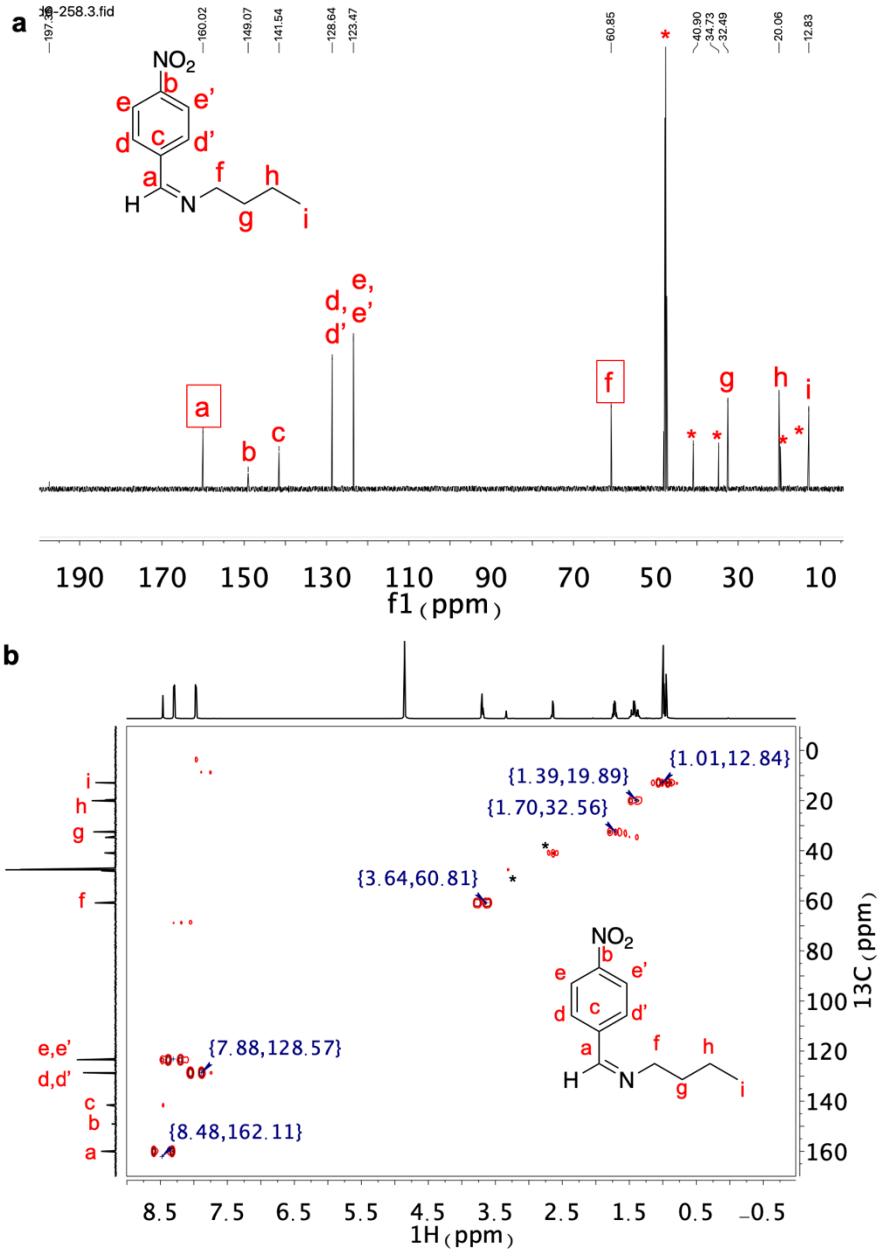

Figure S4. Schiff base model of intermediate 1 obtained by reaction between p-nitrobenzaldheyde and butylamine: a) 13C{1H} NMR spectra and b) HSQC (* excess butylamine and solvent), peaks a and f are absent in any of the starting materials.

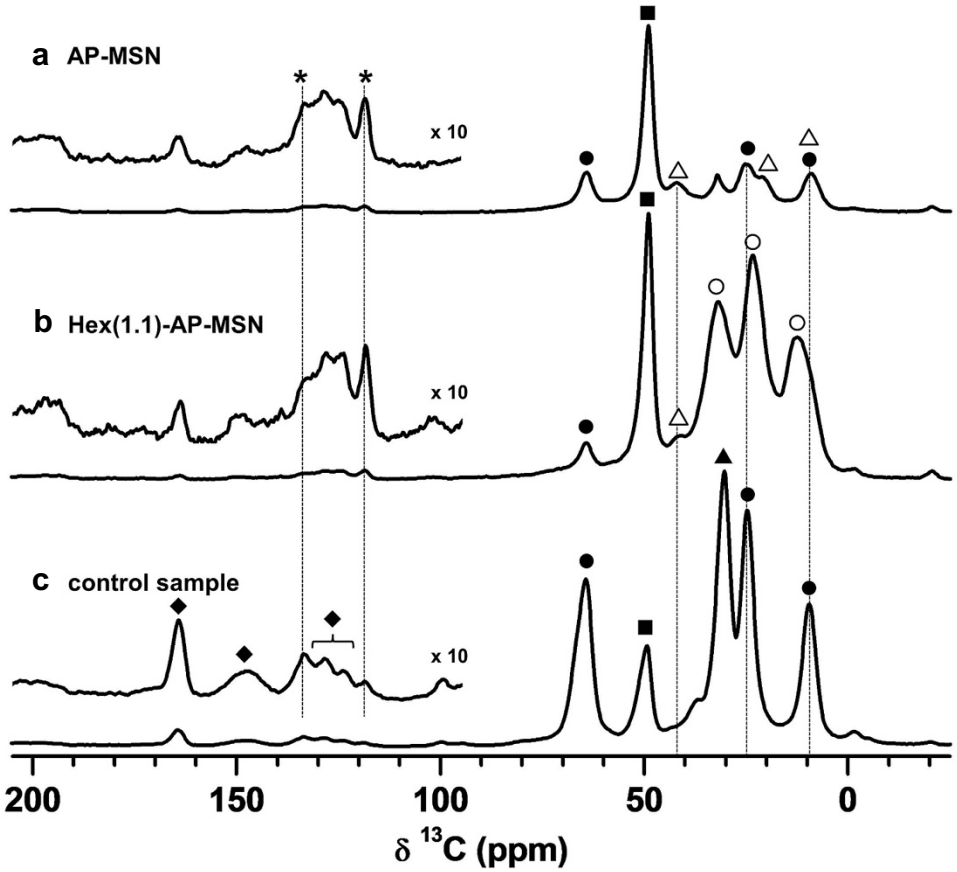

Figure S5. DNP-enhanced $^{13}C\{^{1}H\}$ CPMAS spectra of a) AP-MSN after reaction in 1-propanol, b) Hex(1.1)-AP-MSN after reaction with water, and c) control sample. The spectra were obtained using $\nu_{RF}(^{1}H)$ = 100 kHz during short pulse and heteronuclear ^{1}H decoupling (TPPM), $\nu_{RF}(^{1}H)$ = 85 kHz during CP, $\nu_{RF}(^{13}C)$ = 71 kHz during CP, contact time τ_{CP} = 0.5 ms, recycle delay τ_{RD} = 6.0 (s), number of scans = 800 (A, B), and 3200 (C). The spectra were normalized based on the number of scans and the sample amount packed in the NMR rotor. The control sample was prepared as follows: the mixture containing non-functionalized MSN (60 mg), 1-propanol (3 mL), *p*-nitrobenzaldehyde (60 mg) and acetone (3 mL) was stirred for 24 h at 60 °C, centrifuged, decanted, and washed with methanol. The sample was again centrifuged, decanted, and then dried for 2 h under vacuum. The open triangles (△) and circles (○) represent the signals assigned to AP and Hex, respectively. The filled symbols represent 1-propanol (●), CTAB (▲) , methoxy (CH_3–O–Si) (■) and *p*-nitrobenzaldehyde derivative(s) (♦). Asterisks denote the spinning sidebands.

The spectra of AP-MSN and Hex(1.1)-AP-MSN showed the signals attributed to the functional groups. However, due to the very low loading (~0.06 mmol/g), the AP resonances in the AP-MSN were dominated by additional peaks representing residual solvent, reactants, and products,

which remained even after vacuum drying. As expected, in the Hex(1.1)-AP-MSN, the aliphatic spectral region was dominated by the silica-bound hexyl functionalities. Unfortunately, resonances representing the Schiff base products, which we were able to identify in the heavily AP-loaded MSNs (>1 mmol/g),1,2 could not be unambiguously discerned in neither sample, as they overlapped with those representing residual p-nitrobenzaldehyde derivatives and the spinning sidebands originating from the strong aliphatic peaks. This is not surprising, given that the concentration of Schiff base in these samples is even smaller than AP. However, in addition to elemental analysis, Schiff base formation was indicated by comparing the color of the spent catalysts (Figure S4).

[1]Kandel, K.; Althaus, S. M.; Peeraphatdit, C.; Kobayashi, T.; Trewyn, B. G.; Pruski, M.; Slowing, I. I., ACS Catal. 2013, 3, 265-271.

[2]Kandel, K.; Althaus, S. M.; Peeraphatdit, C.; Kobayashi, T.; Trewyn, B. G.; Pruski, M.; Slowing, I. I., J. Catal. 2012, 291, 63-68.

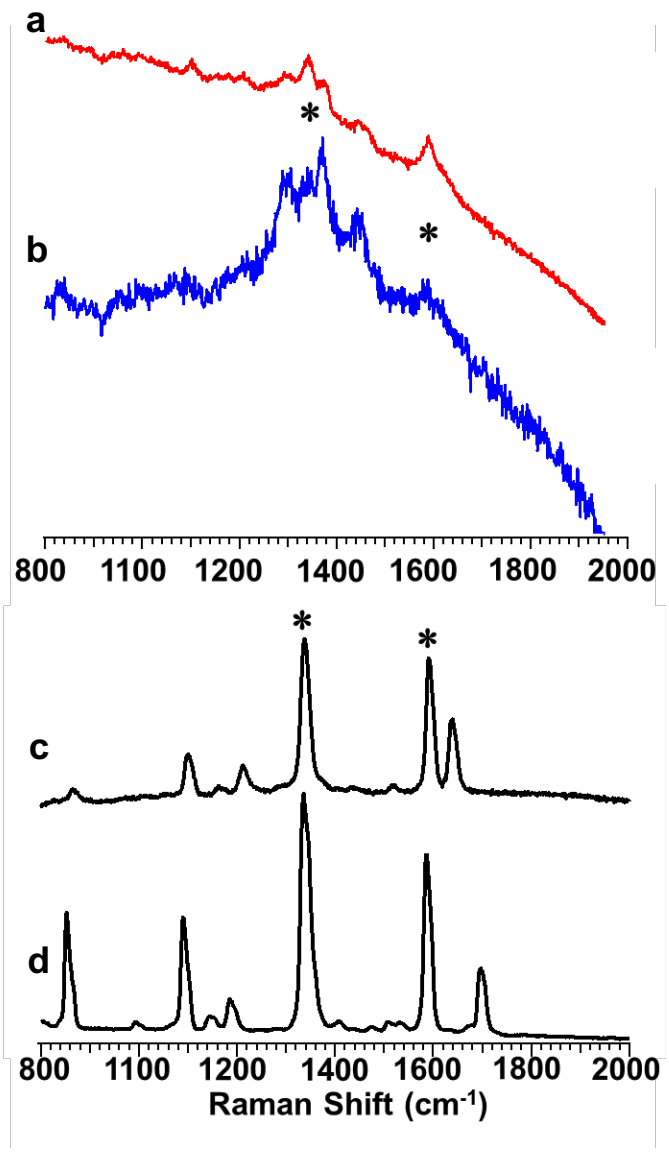

Figure S6. Raman spectra of a) spent AP-MSN, b) spent Hex(1.0)-AP-MSN, c) Schiff base model of the intermediate obtained from reaction between p-nitrobenzaldehyde and butylamine, and d) p-nitrobenzaldehyde. The Raman peaks at ca. 1590 cm-1 and 1350 cm-1 correspond to aromatic NO2 antisymmetric and symmetric stretching respectively.[1,2] Y-axis is relative Raman scattering intensity (a.u.)

[1]Kalaichelvan, S., N. Sundaraganesan, and B.D. Joshua, FT-IR, FT-Raman spectra and ab initio HF and DFT calculations of 2-nitro-and 4-nitrobenzaldehydes. 2008.

[2]Lambert, J.B., et al., Introduction to organic spectroscopy. 1987: Macmillan Publishing Company.

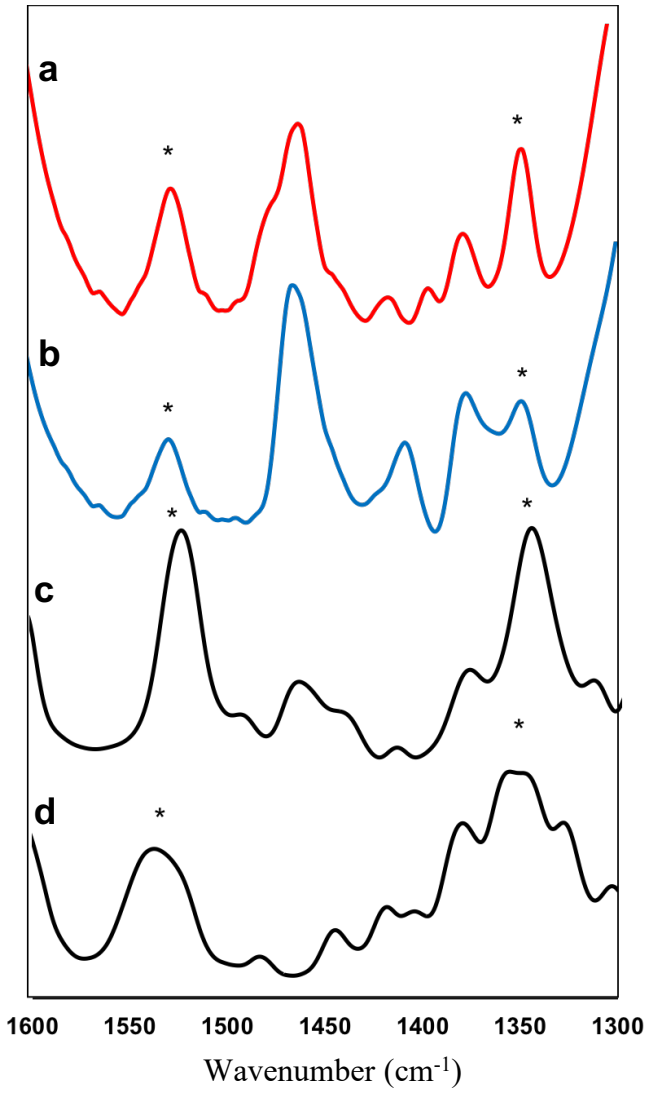

Figure S7. DRIFT-IR spectra in the fingerprint region of a) spent AP-MSN, b) spent Hex(1.0)-AP-MSN, c) Schiff base model of the intermediate obtained from reaction between *p*-nitrobenzaldehyde and butylamine, and d) *p*-nitrobenzaldehyde. The IR bands at approximately 1520 cm^{-1} and 1350 cm^{-1}correspond to aromatic NO_2 stretching vibrations.

Equation S2.

For a bimolecular reaction between two dipoles having no net charge;

$$\ln k \approx \ln k_0 + \frac{3e^2}{8KT}\left(\frac{2}{\varepsilon} - 1\right)\left(\frac{G_A}{b_A^3} + \frac{G_B}{b_B^3} - \frac{G_{\neq}}{b_{\neq}^3}\right)$$

ε	Dielectric constant of the medium
k	Rate constant in a medium of dielectric constant ε
k_0	Rate constant in a medium of dielectric constant ε =1
K	Boltzmann constant
T	Temperature
e	Charge on surface
b	Radius of molecule
G	Charge distribution parameter, proportional to the dipole moment

(A and B correspond to two reactant dipoles and ≠ sign corresponds to the activated complex)
(From: Laidler, K. J.; Landskroener, P. A., The influence of the solvent on reaction rates. *Trans. Faraday Soc.* 1956, *52*, 200-210)

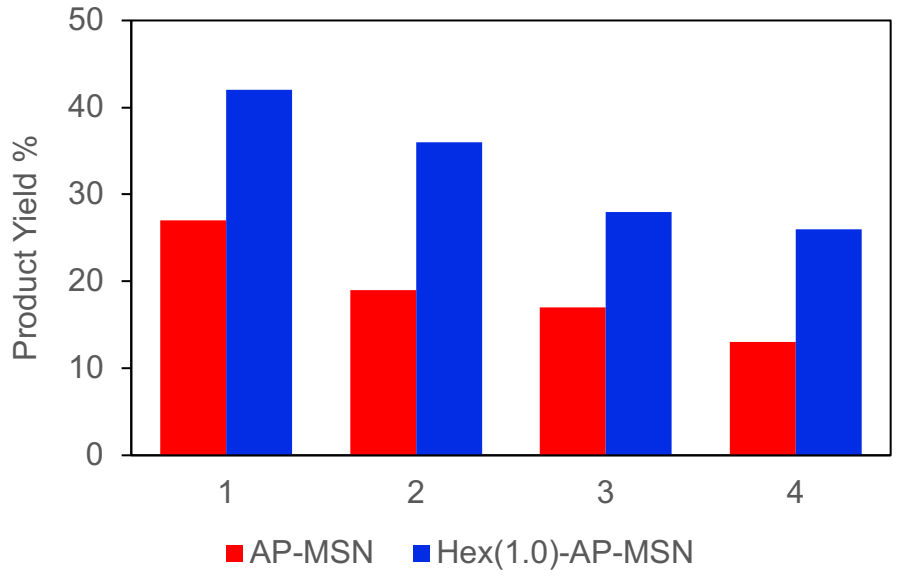

Figure S8. Catalyst recycling for AP-MSN in 1-propanol (red) and Hex(1.0)-AP-MSN in water (blue). Conditions: 60 °C, 12 h, 60 mg catalyst. Catalysts were washed with acetone after each cycle to remove physisorbed unreacted *p*-nitrobenzaldehyde.

Table S2. Catalysis data for AP-MSN in different solvents.

Sample	ε	TOF (h^{-1})	% Selectivity	
			Aldol	Enone
Water	65.8±1.4	0.58±0.05	95	5
Methanol	32.6	0.43±0.02	77	23
Ethanol	22.4	0.57±0.02	72	28
1-Propanol	20.1	0.65±0.02	73	26
2-Propanol	18.3	0.75±0.07	81	19
2-Butanol	16.6	1.1±0.1	80	20

Reaction conditions:1.0 mol% AP, 60 °C, 8 h.

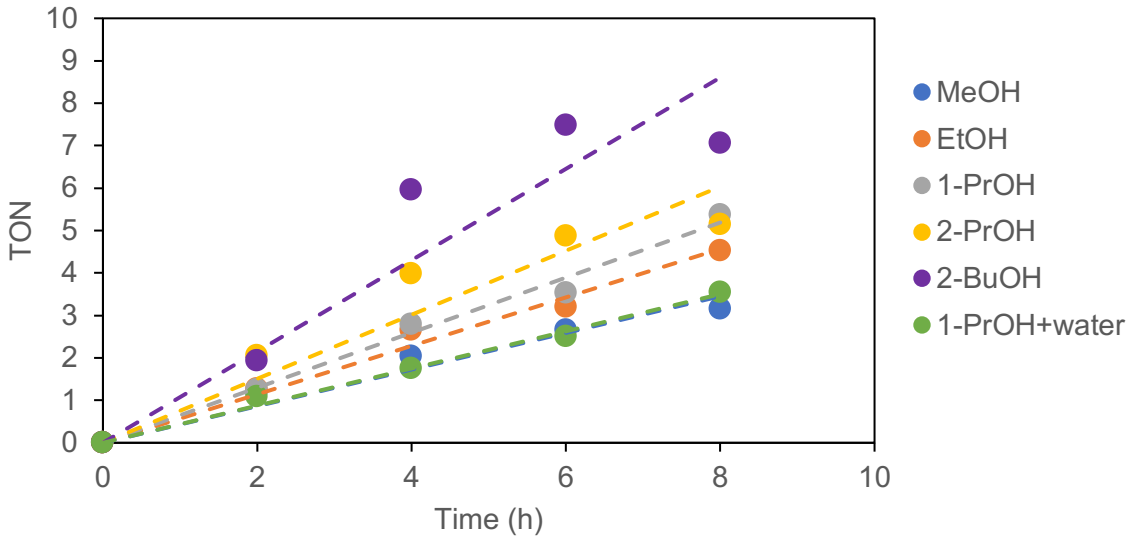

Figure S9. Kinetic plots for AP-MSN in different solvents. Reaction conditions:1.0 mol% AP, 60 °C, 8 h.

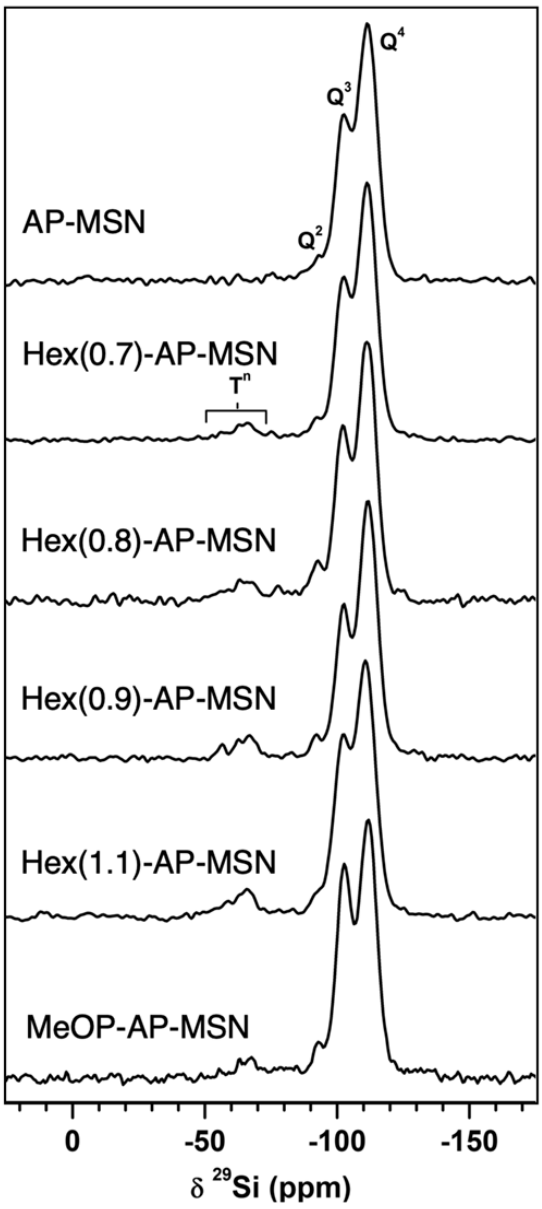

Figure S10. ^{29}Si DPMAS-NMR spectra of different MSN samples. The spectra were obtained using excitation with a single $\pi/2$ pulse of 5 μs followed by data acquisition under TPPM ^{1}H decoupling, using the magnitude of the RF magnetic field $\nu_{RF}(^{1}H)$ = 40 kHz. 296 transients were accumulated with a recycle delay of 300 s. The resonances are assigned as follows: Q^4 represents core sites connected to four Si neighbors via siloxane bridges ($(\equiv SiO)_4\mathbf{Si}$), whereas surface sites are denoted as Q^3 ($(\equiv SiO)_3\mathbf{Si}(OH)$) and Q^2 ($(\equiv SiO)_2\mathbf{Si}(OH)_2$). Functionalization with R groups generates the so-called T^n sites, with a general formula ($(\equiv SiO)_n\mathbf{Si}R(OH)_{3-n}$).

Table S3. Surface properties of the functionalized MSN samples.

Sample	SA_{BET} (m^2/g)	W_{BJH} (nm)	Stokes Shift(nm)	Interfacial Dielectric Constant in Water (ε_i)
AP-MSN	1234	2.9	186.3±0.3	74.8±0.8
Hex(0.5)-AP-MSN	803	2.0	164.9±0.4	35.3±0.5
Hex(0.7)-AP-MSN	1181	2.4	156.2±0.1	26.0±0.1
Hex(0.9)-AP-MSN	1053	2.3	154.7±0.1	24.6±0.1
Hex(1.0)-AP-MSN	1126	2.6	151.0±0.6	21.6±0.5
MeOP-AP-MSN	1119	2.6	174.0±0.8	49±1
CNEt-AP-MSN	1180	2.7	176.6±0.6	53±1

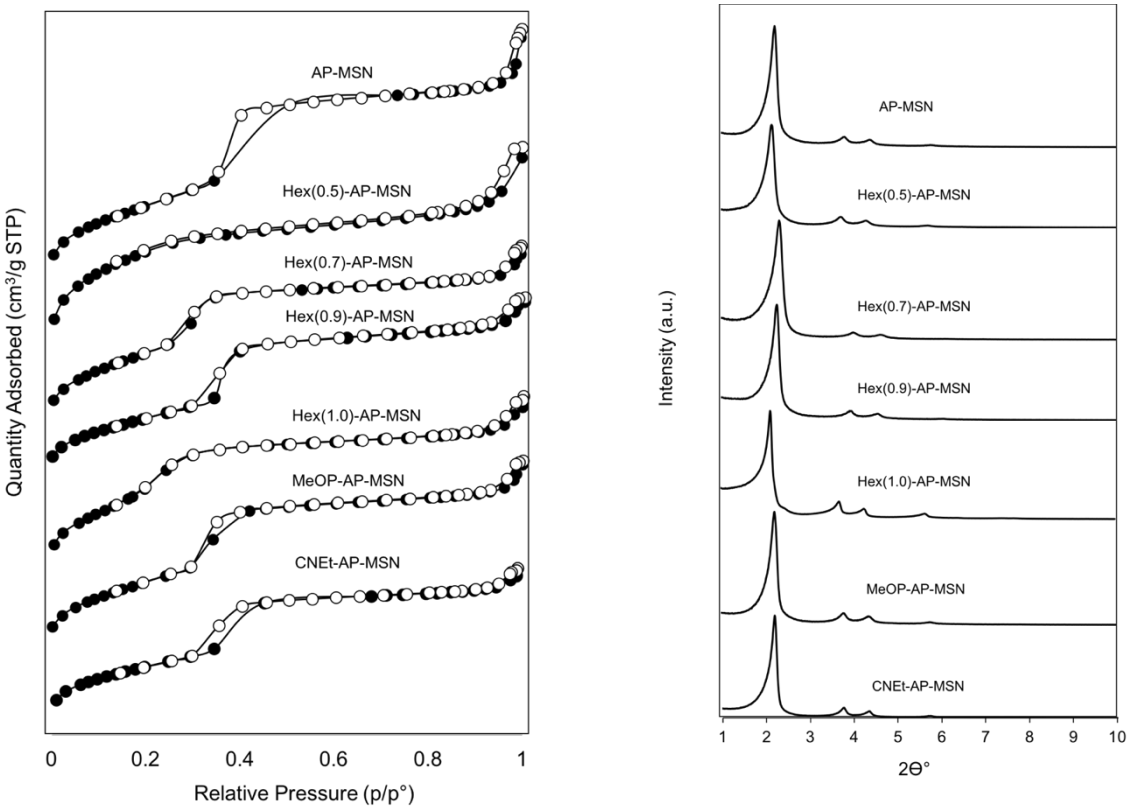

Figure S11. a) Nitrogen physisorption isotherms, and b) powder x-ray diffraction patterns of the functionalized MSN samples.

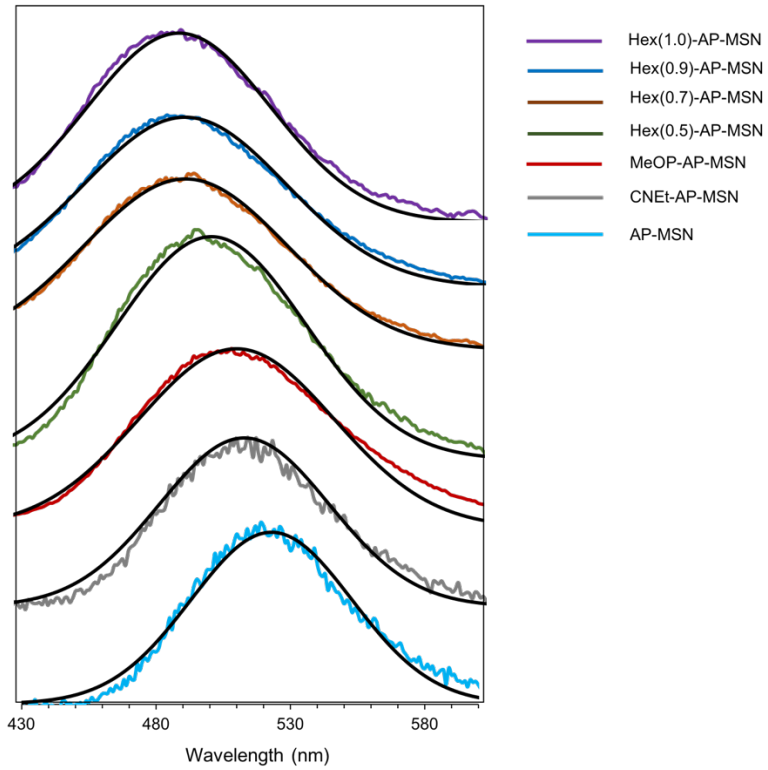

Figure S12. Fluorescence emission spectra of water suspensions of Prodan-loaded MSN samples fitted (black trace) with a Gaussian function in OriginPro. Excitation wavelength: 337 nm, slit widths: 5 nm each.

Table S4. Catalysis data for Hex-AP-MSN in water.

Sample	ε_i	TOF (h^{-1})	% Selectivity	
			Aldol	Enone
AP-MSN	74.8±0.8	0.58±0.05	95	5
Hex(0.5)-AP-MSN	35.3±0.5	1.6±0.1	96	4
Hex(0.7)-AP-MSN	26.0±0.1	1.9±0.2	97	3
Hex(0.9)-AP-MSN	24.6±0.1	2.4±0.1	97	3
Hex(1.0)-AP-MSN	21.6±0.5	3.2±0.2	96	4
MeOP-AP-MSN	48.5±1.4	1.32±0.09	91	9
CNEt-AP-MSN	53.1±1.1	0.68±0.03	94	6
AP-MSN (water+1-propanol)	44[a]	0.44±0.01	72	28

[a]Méndez-Bermúdez, J. G.; Dominguez, H.; Pusztai, L.; Guba, S.; Horváth, B.; Szalai, I., Composition and temperature dependence of the dielectric constant of 1-propanol/water mixtures: Experiment and molecular dynamics simulations. *J. Mol. Liq.* 2016, *219*, 354-358. Reaction conditions:1.0 mol% AP, 60 °C, 8 h.

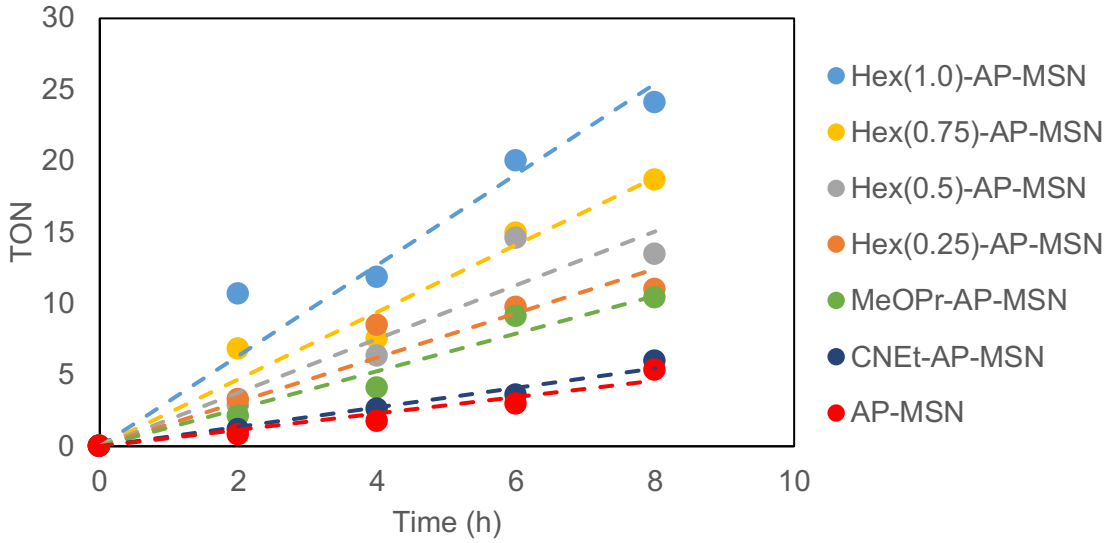

Figure S13. Kinetic plots for substituted AP-MSN in water. Reaction conditions:1.0 mol% AP, 60 °C.

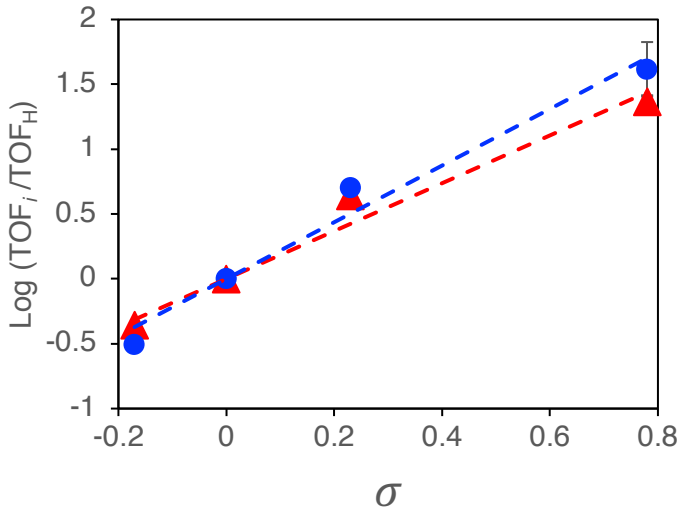

Figure S14. Hammett plots for the aldol reaction between *p*-substituted benzaldehydes and acetone using Hex(1.0)-AP-MSN (blue circles) and AP-MSN (red triangles) as catalysts in water (1.0 mol% amine, 60 °C).

Table S5. Catalysis data for Hammett relationships studies.

Substituent	AP-MSN			Hex(1.0)-AP-MSN		
	TOF (h^{-1})	%Aldol	%Enone	TOF (h^{-1})	%Aldol	%Enone
$-NO_2$[a]	0.58±0.05	95	5	3.2±0.2	96	4
-Br[b]	0.109±0.004	78	20	0.39±0.04	86	14
-H[c]	0.025±0.004	88	12	0.077±0.009	88	12
$-CH_3$[c]	0.011±0.003	82	18	0.024±0.003	83	17

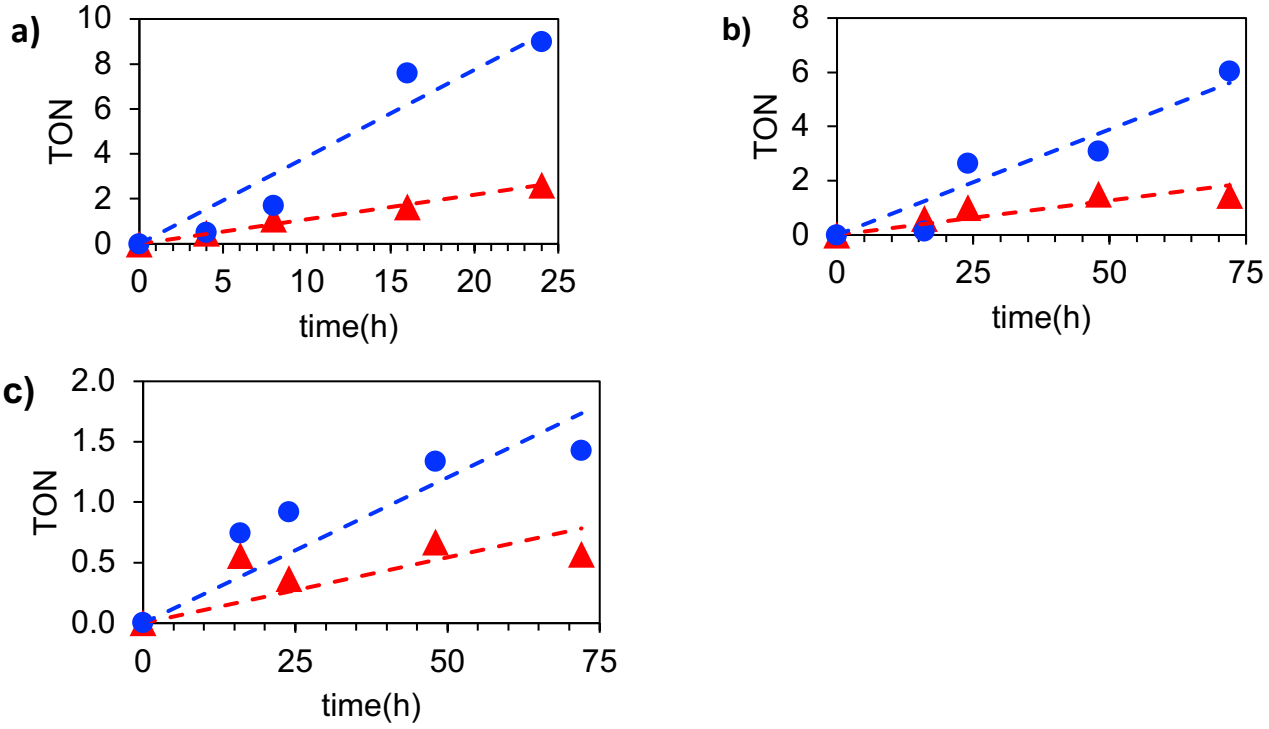

Figure S15. Kinetic plots for Hammett relationship studies. a) p-Br-, b) unsubstituted (-H), and c) p-methyl- benzaldehyde substrates. The plots for p-nitrobenzaldehyde are shown in Figures S12 and S13.

Equation S3.

$$Log\ \frac{TOF}{TOF_0} = \rho\sigma$$

TOF turnover frequency for the substituted benzaldehyde
TOF0 turnover frequency for the unsubstituted benzaldehyde
ρ reaction constant
σ substituent constant
(From: Hammett, L. P., The Effect of Structure upon the Reactions of Organic Compounds. Benzene Derivatives. J. Am. Chem. Soc. 1937, 59, 96-103)

Equation S4.

$$\rho = \frac{1}{d^2\,T}\left(\frac{B_1}{\varepsilon} + B_2\right)$$

T temperature,
d the distance from the substituent to the reacting group (carbonyl group)
ε the dielectric constant of the reaction medium
B_1,B_2 constants depend on the reaction and independent of temperature and solvent
(From: Hammett, L. P., The Effect of Structure upon the Reactions of Organic Compounds. Benzene Derivatives. *J. Am. Chem. Soc.* **1937,** *59*, 96-103.

Table S6. Amounts of organosilanes used in the synthesis of functionalized MSN.

Sample	Ligand	Volume (µL)
AP-MSN	3-aminopropyltrimethoxysilane	35
Hex(0.5)-AP-MSN	3-aminopropyltrimethoxysilane	35
	hexyltrimethoxysilane	55
Hex(0.7)-AP-MSN	3-aminopropyltrimethoxysilane	35
	hexyltrimethoxysilane	110
Hex(0.9)-AP-MSN	3-aminopropyltrimethoxysilane	35
	hexyltrimethoxysilane	170
Hex(1.0)-AP-MSN	3-aminopropyltrimethoxysilane	35
	hexyltrimethoxysilane	220
MeOP-AP-MSN	3-aminopropyltrimethoxysilane	35
	3-methoxypropyltrimethoxysilane	190
CNEt-AP-MSN	3-aminopropyltrimethoxysilane	35
	2-cyanoethyltriethoxysilane	154

Spectral data of substrates and reaction products.

1. Aldol reaction: *p*-Nitrobenzaldehyde (PNB) and acetone

PNB: ^{1}H NMR (500 MHz, $CDCl_3$) 10.17 (s, 1H), 8.41 (d, J = 8.5 Hz, 2H), 8.09 (d, J = 8.6 Hz, 2H); *aldol product*: ^{1}H NMR (500 MHz, $CDCl_3$) 8.23 (d, J = 8.7 Hz, 2H), 7.57 (d, J = 8.6 Hz, 2H), 5.29 (dt, J = 7.6,3.4, Hz, 1 H), 2.87 (m, 2H), 2.25 (s, 3H); *enone product*: ^{1}H NMR (500 MHz, $CDCl_3$) 8.28 (d, J = 8.8 Hz, 2H), 7.72 (d, J = 9.0 Hz, 2H), 7.55 (d, J = 16.3 Hz, 1H), 6.84 (d, J = 16.3 Hz, 1H), 2.44 (s, 3H).

2. Aldol reaction: *p*-Bromobenzaldehyde (PBB) and acetone

PBB: ^{1}H NMR (500 MHz, $CDCl_3$) 9.98 (s, 1H), 7.75 (d, J = 8.5 Hz, 2H), 7.69 (d, J = 8.5 Hz, 2H); *aldol product*: ^{1}H NMR (500 MHz, $CDCl_3$) 7.47 (d, J = 8.4 Hz, 2H), 7.24 (d, J = 8.3 Hz, 2H), 5.12 (dd, J = 8.7,3.6 Hz, 1 H), 2.83 (d, J = 8.7 Hz, 1H), 2.81 (d, J = 3.7 Hz, 1H), 2.20 (s, 3H); *enone product*: ^{1}H NMR (500 MHz, $CDCl_3$) 7.53 (d, J = 8.5 Hz, 2H), 7.44 (d, J = 16.3 Hz, 1H), 7.41 (d, J = 8.5 Hz, 2H), 6.70 (d, J = 16.3 Hz, 1H), 2.38 (s, 3H)

3. Aldol reaction: Benzaldehyde and acetone

Benzaldehyde: ^{1}H NMR (500 MHz, $CDCl_3$) 10.03 (s, 1H), 7.89 (d, J = 7.6 Hz, 2H), 7.64 (t, J = 7.4 Hz, 1H), 7.54 (t, J = 7.5 Hz, 2H), GC-MS, *m/z*: $[M]^+$ (106), 105 $[M-H]^+$, 77 $[M-CHO]^+$, *aldol product*: ^{1}H NMR (500 MHz, $CDCl_3$) 7.64 (m, 2H), 7.38 (m, 2H), 7.32 (m, 1H), 5.20 (dd, J = 9.3, 3.1 Hz, 1 H), 2.93 (dd, J = 17.6, 9.4 Hz, 1H), 2.86 (dd, J = 17.6, 3.2 Hz, 1H), 2.08 (s, 3H); *enone product*: ^{1}H NMR (500 MHz, $CDCl_3$) 7.58 (dd, J = 6.7, 3.0 Hz, 2H), 7.55 (d, J = 16.4 Hz, 1H), 7.43 (m, 3H), 6.76 (d, J = 16.3 Hz, 1H), 2.42 (s, 3H), GC/MS, *m/z*: $[M]^+$ (146), 131 $[M-CH_3]^+$, 103 $[M-COCH_3]^+$ (Quantifications were done with combined NMR and GC-MS data)

4. Aldol reaction: *p*-Tolualdehyde (PT) and acetone

PT: ^{1}H NMR (500 MHz, $CDCl_3$) 9.97 (s, 1H), 7.81 (d, J = 7.8 Hz, 2H), 7.33 (d, J = 7.8 Hz, 2H), 2.44 (s,3H); GC-MS, *m/z*: $[M]^+$ (120), 119 $[M-H]^+$, 91 $[M-CHO]^+$, *aldol product*: ^{1}H NMR (600 MHz, $CDCl_3$) 7.25 (d, J = 8.0 Hz, 2H), 7.17 (d, J = 7.8 Hz, 2H), 5.13 (dd, J = 9.4, 3.1 Hz, 1 H), 2.89 (dd, J = 17.5,9.4 Hz, 1H), 2.80 (dd, J = 17.5,3.1 Hz, 1H)2.01 (s, 3H); *enone product*: ^{1}H NMR (500 MHz, $CDCl_3$) 7.50 (d, J = 16.2 Hz, 1H), 7.45 (d, J = 8.1 Hz, 2H), 7.21 (d, J = 7.9 Hz, 2H), 6.69 (d, J = 16.3 Hz, 1H), 2.27 (s, 3H),GC/MS, *m/z*: $[M]^+$ (160), 145 $[M-CH_3]^+$, 117 $[M-COCH_3]^+$

(Quantifications were done with combined NMR and GC-MS data)

5. Henry reaction: *p*-Nitrobenzaldehyde (PNB) and nitromethane

PNB: 1H NMR (500 MHz, Acetone- d6)) 10.00 (s, 1H), 8.22 (d, J = 9.0 Hz, 2H), 7.99 (d, J = 9.0 Hz, 2H); condensation product: 1H NMR (500 MHz, Acetone-D6) 8.04 (m, 2H), 7.60 (d, J = 9.0 Hz, 2H), 5.42 (m, 1 H), 4.68 (dd, J = 12.9,3.4 Hz, 1H), 2.47 (m, 1H); dehydration product: 1H NMR (500 MHz, Acetone-d6) 8.11 (d, J = 8.7 Hz, 1H), 8.03 (m, 2H), 7.92 (d, J = 10.8 Hz, 2H), 7.89 (d, J = 6.7 Hz, 1H)

6. Vinylogous aldol reaction: *p*-Nitrobenzaldehyde (PNB) and 3-butan-2-one

PNB: ^{1}H NMR (500 MHz, $CDCl_3$) 10.17 (s, 1H), 8.41 (d, J = 8.5 Hz, 2H), 8.09 (d, J = 8.6 Hz, 2H); *condensation product*: ^{1}H NMR (500 MHz, $CDCl_3$) 8.23 (d, J=8.8 Hz, 2H), 7.59 (d, J = 8.9 Hz, 2H), 6.06 (d, J=1.1 Hz, 1 H), 5.71 (d, J = 1.1Hz, 1H), 4.87 (s, 1H), 2.39 (s, 3H)

7. Homogeneous model of intermediate 1: (*p*-nitrobenzaldehyde reacted with butylamine, N-butyl-1-(4-nitrophenyl)methanimine)

^{1}H NMR (600 MHz, Methanol-d_4) 8.46 (s,1H), 8.29 (d, J=8.1 Hz, 2H), 7.96 (d, J=8.1 Hz, 2H), 3.68 (td, J=7.4 Hz, 1.49Hz, 2H), 1.72 (m, 2H), 1.43 (m, 2H), 0.95 (t, 3H). ^{13}C NMR (600 MHz, Methanol-d_4) 160.02, 149.07, 141.54, 128.64, 123.47, 60.85, 32.49, 20.06, 12.83

Solvent purification procedures.

Commercial anhydrous 1-propanol and anhydrous 2-butanol were used without any further purification. Acetone, methanol, ethanol and 2-propanol were treated with CaH_2 at room temperature overnight. Acetone (b.p. 56 °C), and methanol (b.p. 64 °C) were then purified using simple distillation from the CaH_2-containing mixture. Ethanol (b.p. 78 °C) and 2-propanol (b.p. 82 °C) were purified from the CaH_2-containing mixture using fractional distillation column. The solvents were sealed and used for reactions immediately after distillation.

References

(1) Reichardt, C., Solvents and Solvent Effects in Organic Chemistry. 4th ed.; Weinheim, Germany : Wiley-VCH: Weinheim, Germany, 2011.

(2) Reichardt, C., Solvents and Solvent Effects: an Introduction. Org. Proc.Res. Develop. 2007, 11, 105-113.

(3) Ruiz-Pernía, J. J.; Martí, S.; Moliner, V.; Tuñón, I., A Novel Strategy to Study Electrostatic Effects in Chemical Reactions: Differences Between the Role of Solvent and the Active Site of Chalcone Isomerase in a Michael Addition. J. Chem. Theor. Comput. 2012, 8, 1532-1535.

(4) Theilacker, K.; Buhrke, D.; Kaupp, M., Validation of the Direct-COSMO-RS Solvent Model for Diels–Alder Reactions in Aqueous Solution. J. Chem. Theor. Comput. 2015, 11, 111-121.

(5) Bernasconi, L.; Baerends, E. J., A Frontier Orbital Study with ab Initio Molecular Dynamics of the Effects of Solvation on Chemical Reactivity: Solvent-Induced Orbital Control in FeO-Activated Hydroxylation Reactions. J. Am. Chem. Soc. 2013, 135, 8857-8867.

(6) Jalan, A.; West, R. H.; Green, W. H., An Extensible Framework for Capturing Solvent Effects in Computer Generated Kinetic Models. J. Phys. Chem. B 2013, 117, 2955-2970.

(7) Horn, M.; Matyjaszewski, K., Solvent Effects on the Activation Rate Constant in Atom Transfer Radical Polymerization. Macromolecules 2013, 46, 3350-3357.

(8) Narske, R. M.; Klabunde, K. J.; Fultz, S., Solvent Effects on the Heterogeneous Adsorption and Reactions of (2-Chloroethyl)ethyl Sulfide on Nanocrystalline Magnesium Oxide. Langmuir 2002, 18, 4819-4825.

(9) Bass, J. D.; Solovyov, A.; Pascall, A. J.; Katz, A., Acid−Base Bifunctional and Dielectric Outer-Sphere Effects in Heterogeneous Catalysis: A Comparative Investigation of Model Primary Amine Catalysts. J. Am. Chem. Soc. 2006, 128, 3737-3747.

(10) Brindza, M. R.; Walker, R. A., Differentiating Solvation Mechanisms at Polar Solid/Liquid Interfaces. J. Am. Chem. Soc. 2009, 131, 6207-6214.

(11) Alam, T. M.; Hibbs, M. R., Characterization of Heterogeneous Solvent Diffusion Environments in Anion Exchange Membranes. Macromolecules 2014, 47, 1073-1084.

(12) Xu, X.; Zhang, C.; Zhai, Y.; Liu, Y.; Zhang, R.; Tang, X., Upgrading of Bio-Oil Using Supercritical 1-Butanol over a Ru/C Heterogeneous Catalyst: Role of the Solvent. Energy Fuels 2014, 28, 4611-4621.

(13) Fridkin, G.; Yehezkel, L.; Columbus, I.; Zafrani, Y., Solvent Effects on the Reactions of the Nerve Agent VX with KF/Al2O3: Heterogeneous or Homogeneous Decontamination? J. Org. Chem. 2016, 81, 2154-2158.

(14) Sievers, C.; Noda, Y.; Qi, L.; Albuquerque, E. M.; Rioux, R. M.; Scott, S. L., Phenomena Affecting Catalytic Reactions at Solid–Liquid Interfaces. ACS Catal. 2016, 6, 8286-8307.

(15) Weber, D.; Mitchell, J.; McGregor, J.; Gladden, L. F., Comparing Strengths of Surface Interactions for Reactants and Solvents in Porous Catalysts Using Two-Dimensional NMR Relaxation Correlations. J. Phys. Chem. C 2009, 113, 6610-6615.

(16) Copeland, J. R.; Shi, X.-R.; Sholl, D. S.; Sievers, C., Surface Interactions of C2 and C3 Polyols with γ-Al2O3 and the Role of Coadsorbed Water. Langmuir 2013, 29, 581-593.

(17) Faheem, M.; Suthirakun, S.; Heyden, A., New Implicit Solvation Scheme for Solid Surfaces. J. Phys. Chem. C 2012, 116, 22458-22462.

(18) Kandel, K.; Althaus, S. M.; Peeraphatdit, C.; Kobayashi, T.; Trewyn, B. G.; Pruski, M.; Slowing, I. I., Solvent-Induced Reversal of Activities between Two Closely Related Heterogeneous Catalysts in the Aldol Reaction. ACS Catal. 2013, 3, 265-271.

(19) Zeidan, R. K.; Hwang, S.-J.; Davis, M. E., Multifunctional Heterogeneous Catalysts: SBA-15-Containing Primary Amines and Sulfonic Acids. Angew. Chem., Int. Ed. 2006, 45, 6332-6335.

(20) Farnesi Camellone, M.; Negreiros Ribeiro, F.; Szabová, L.; Tateyama, Y.; Fabris, S., Catalytic Proton Dynamics at the Water/Solid Interface of Ceria-Supported Pt Clusters. J. Am. Chem. Soc. 2016, 138, 11560-11567.

(21) Collier, V. E.; Ellebracht, N. C.; Lindy, G. I.; Moschetta, E. G.; Jones, C. W., Kinetic and Mechanistic Examination of Acid–Base Bifunctional Aminosilica Catalysts in Aldol and Nitroaldol Condensations. ACS Catal. 2016, 6, 460-468.

(22) Kim, K. C.; Moschetta, E. G.; Jones, C. W.; Jang, S. S., Molecular Dynamics Simulations of Aldol Condensation Catalyzed by Alkylamine-Functionalized Crystalline Silica Surfaces. J. Am. Chem. Soc. 2016, 138, 7664-7672.

(23) Brunelli, N. A.; Venkatasubbaiah, K.; Jones, C. W., Cooperative Catalysis with Acid–Base Bifunctional Mesoporous Silica: Impact of Grafting and Co-condensation Synthesis Methods on Material Structure and Catalytic Properties. Chem. Mater. 2012, 24, 2433-2442.

(24) Lauwaert, J.; Ouwehand, J.; De Clercq, J.; Cool, P.; Van Der Voort, P.; Thybaut, J. W., Tuning component enrichment in amino acid functionalized (organo)silicas. Catal. Commun. 2017, 88, 85-89.

(25) Lauwaert, J.; De Canck, E.; Esquivel, D.; Thybaut, J. W.; Van Der Voort, P.; Marin, G. B., Silanol-Assisted Aldol Condensation on Aminated Silica: Understanding the Arrangement of Functional Groups. ChemCatChem 2014, 6, 255-264.

(26) Lauwaert, J.; De Canck, E.; Esquivel, D.; Van Der Voort, P.; Thybaut, J. W.; Marin, G. B., Effects of amine structure and base strength on acid–base cooperative aldol condensation. Catal. Today 2015, 246, 35-45.

(27) Lewis, J. D.; Van de Vyver, S.; Román-Leshkov, Y., Acid–Base Pairs in Lewis Acidic Zeolites Promote Direct Aldol Reactions by Soft Enolization. Angew. Chem., Int. Ed. 2015, 54, 9835-9838.

(28) 2Hoyt, C. B.; Lee, L.-C.; Cohen, A. E.; Weck, M.; Jones, C. W., Bifunctional Polymer Architectures for Cooperative Catalysis: Tunable Acid–Base Polymers for Aldol Condensation. ChemCatChem 2017, 9, 137-143.

(29) Kandel, K.; Althaus, S. M.; Peeraphatdit, C.; Kobayashi, T.; Trewyn, B. G.; Pruski, M.; Slowing, I. I., Substrate Inhibition in the Heterogeneous Catalyzed Aldol Condensation: A Mechanistic Study of Supported Organocatalysts. J. Catal. 2012, 291, 63-68.

(30) Tarabanko, V. E.; Hendogina, Y. V.; Petuhov, D. V.; Pervishina, E. P., On the Role of Retroaldol Reaction in the Process of Lignin Oxidation into Vanillin. Kinetics of the Vanillideneacetone Cleavage in Alkaline Media. React. Kinetics Catal. Lett. 2000, 69, 361-368.

(31) Fan, H.; Yang, Y.; Song, J.; Ding, G.; Wu, C.; Yang, G.; Han, B., One-pot Sequential Oxidation and Aldol-Condensation Reactions of Veratryl Alcohol Catalyzed by the Ru@ZIF-8 + CuO/Basic Ionic Liquid System. Green Chem. 2014, 16, 600-604.

(32) Sasaki, M.; Furukawa, M.; Minami, K.; Adschiri, T.; Arai, K., Kinetics and Mechanism of Cellobiose Hydrolysis and Retro-Aldol Condensation in Subcritical and Supercritical Water. Ind. Eng. Chem. Res. 2002, 41, 6642-6649.

(33) Liang, G.; Wang, A.; Zhao, X.; Lei, N.; Zhang, T., Selective Aldol Condensation of Biomass-derived Levulinic Acid and Furfural in Aqueous-phase over MgO and ZnO. Green Chem. 2016, 18, 3430-3438.

(34) Nelson, N.; Chaudhary, U.; Kandel, K.; Slowing, I., Heterogeneous Multicatalytic System for Single-Pot Oxidation and C–C Coupling Reaction Sequences. Top. Catal. 2014, 57, 1000-1006.

(35) Dabral, S.; Hernández José, G.; Kamer Paul, C. J.; Bolm, C., Organocatalytic Chemoselective Primary Alcohol Oxidation and Subsequent Cleavage of Lignin Model Compounds and Lignin. ChemSusChem 2017, 10, 2707-2713.

(36) Bui Tuong, V.; Sooknoi, T.; Resasco Daniel, E., Simultaneous Upgrading of Furanics and Phenolics through Hydroxyalkylation/Aldol Condensation Reactions. ChemSusChem 2017, 10, 1631-1639.

(37) Pham Tu, N.; Zhang, L.; Shi, D.; Komarneni Mallik, R.; Ruiz Maria, P.; Resasco Daniel, E.; Faria, J., Fine-Tuning the Acid–Base Properties of Boron-Doped Magnesium Oxide Catalyst for the Selective Aldol Condensation. ChemCatChem 2016, 8, 3611-3620.

(38) Lee, K. S.; Parquette, J. R., A self-assembled nanotube for the direct aldol reaction in water. Chem. Commun. 2015, 51, 15653-15656.

(39) Lu, A.; Moatsou, D.; Hands-Portman, I.; Longbottom, D. A.; O'Reilly, R. K., Recyclable l-Proline Functional Nanoreactors with Temperature-Tuned Activity Based on Core–Shell Nanogels. ACS Macro Letters 2014, 3, 1235-1239.

(40) Eymur, S.; Akceylan, E.; Sahin, O.; Uyanik, A.; Yilmaz, M., Direct Enantioselective Aldol Reactions Catalyzed by Calix[4]Arene-Based L-Proline Derivatives in the Water. Tetrahedron 2014, 70, 4471-4477.

(41) Doyagüez, E. G.; Calderón, F.; Sánchez, F.; Fernández-Mayoralas, A., Asymmetric Aldol Reaction Catalyzed by a Heterogenized Proline on a Mesoporous Support. The Role of the Nature of Solvents. J. Org. Chem. 2007, 72, 9353-9356.

(42) Schmid, M. B.; Zeitler, K.; Gschwind, R. M., The Elusive Enamine Intermediate in Proline-Catalyzed Aldol Reactions: NMR Detection, Formation Pathway, and Stabilization Trends. Angew. Chem., Int. Ed. 2010, 49, 4997-5003.

(43) De Vylder, A.; Lauwaert, J.; Esquivel, D.; Poelman, D.; De Clercq, J.; Van Der Voort, P.; Thybaut, J. W., The Role of Water in the Reusability of Aminated Silica Catalysts for Aldol Reactions. J. Catal. 2018, 361, 51-61.

(44) Cummings, T. F.; Shelton, J. R., Mannich Reaction Mechanisms. J. Org. Chem. 1960, 25, 419-423.

(45) Singappuli-Arachchige, D.; Manzano, J. S.; Sherman, L. M.; Slowing, I. I., Polarity Control at Interfaces: Quantifying Pseudo-solvent Effects in Nano-confined Systems. ChemPhysChem 2016, 17, 2982-2986.

(46) Méndez-Bermúdez, J. G.; Dominguez, H.; Pusztai, L.; Guba, S.; Horváth, B.; Szalai, I., Composition and Temperature Dependence of the Dielectric Constant of 1-Propanol/Water Mixtures: Experiment and Molecular Dynamics Simulations. J. Mol. Liq. 2016, 219, 354-358.

(47) Smallwood, I., Handbook of Organic Solvent Properties. Burlington : Elsevier Science: Burlington, 1996.

(48) Soto-Cantu, E.; Cueto, R.; Koch, J.; Russo, P. S., Synthesis and Rapid Characterization of Amine-Functionalized Silica. Langmuir 2012, 28, 5562-5569.

(49) Manzano, J. S.; Weinstein, Z. B.; Sadow, A. D.; Slowing, I. I., Direct 3D Printing of Catalytically Active Structures. ACS Catal. 2017, 7, 7567-7577.

(50) Bass, J. D.; Anderson, S. L.; Katz, A., The Effect of Outer-Sphere Acidity on Chemical Reactivity in a Synthetic Heterogeneous Base Catalyst. Angew. Chem. 2003, 115, 5377-5380.

(51) Weber, G.; Farris, F. J., Synthesis and Spectral Properties of a Hydrophobic Fluorescent Probe: 6-Propionyl-2-(Dimethylamino)Naphthalene. Biochem. 1979, 18, 3075-3078.

(52) Cerezo, F. M.; Rocafort, S. C.; Sierra, P. S.; García-Blanco, F.; Oliva, C. D.; Sierra, J. C., Photophysical Study of the Probes Acrylodan (1-[6-(Dimethylamino)naphthalen-2-yl]prop-2-en-1-one), ANS (8-Anilinonaphthalene-1-sulfonate) and Prodan (1-[6-(Dimethylamino)naphthalen-2-yl]propan-1-one) in Aqueous Mixtures of Various Alcohols. Helv. Chim. Acta 2001, 84, 3306-3312.

(53) Catalan, J.; Perez, P.; Laynez, J.; Blanco, F. G., Analysis of the Solvent Effect on the Photophysics Properties of 6-Propionyl-2-(dimethylamino)naphthalene (PRODAN). J Fluoresc 1991, 1, 215-223.

(54) Trébosc, J.; Wiench, J. W.; Huh, S.; Lin, V. S. Y.; Pruski, M., Solid-State NMR Study of MCM-41-type Mesoporous Silica Nanoparticles. J. Am. Chem. Soc. 2005, 127, 3057-3068.

(55) Grünberg, B.; Emmler, T.; Gedat, E.; Shenderovich, I.; Findenegg, G. H.; Limbach, H.-H.; Buntkowsky, G., Hydrogen Bonding of Water Confined in Mesoporous Silica MCM-41 and SBA-15 Studied by 1H Solid-State NMR. Chem. Eur. J. 2004, 10, 5689-5696.

(56) Laidler, K. J.; Landskroener, P. A., The Influence of the Solvent on Reaction Rates. Trans. Faraday Soc. 1956, 52, 200-210.

(57) Yakupov, M. Z.; Lyapina, N. K.; Shereshovets, V. V.; Imashev, U. B., The Solvent Effect on the Rate of Reaction between Propanethiol and Chlorine Dioxide. Kinet. Catal. 2001, 42, 609-612.

(58) Yutilova, K.; Shved, E.; Shuvakin, S., Behavior of epichlorohydrin catalytic acidolysis reaction with the variation of solvent polarity. React. Kinet. Mech. Catal. 2018, 125, 15-24.

(59) Karthikeyan, G.; Anbalagan, K.; Elango, K. P., Correlation Analysis of Reactivity in the Reduction of Trans-Chloro(RC6H4NH2)Bis(1,2-Diaminoethane)Cobalt(III) Complexes by Hexacyanoferrate(II) in Aqueous Methanol. Transit. Metal Chem. 2000, 25, 213-218.

(60) Huh, S.; Wiench, J. W.; Yoo, J.-C.; Pruski, M.; Lin, V. S.-Y., Organic Functionalization and Morphology Control of Mesoporous Silicas via a Co-Condensation Synthesis Method. Chem. Mater. 2003, 15, 4247-4256.

(61) Hammett, L. P., The Effect of Structure upon the Reactions of Organic Compounds. Benzene Derivatives. J. Am. Chem. Soc. 1937, 59, 96-103.

(62) Ballini, R.; Bosica, G., Nitroaldol Reaction in Aqueous Media: An Important Improvement of the Henry Reaction. J. Org. Chem. 1997, 62, 425-427.

(63) Motokura, K.; Tada, M.; Iwasawa, Y., Heterogeneous Organic Base-Catalyzed Reactions Enhanced by Acid Supports. J. Am. Chem. Soc. 2007, 129, 9540-9541.

(64) Casiraghi, G.; Battistini, L.; Curti, C.; Rassu, G.; Zanardi, F., The Vinylogous Aldol and Related Addition Reactions: Ten Years of Progress. Chem. Rev. 2011, 111, 3076-3154.

CHAPTER 4. FINE-TUNING THE RELEASE OF MOLECULAR GUESTS FROM MESOPOROUS SILICAS BY CONTROLLING THE ORIENTATION AND MOBILITY OF SURFACE PHENYL SUBSTITUENTS

This work was published in *Chem. Eng. J.*, **2018**, *340*,75-80.

J. Sebastián Manzano,[1,2,†] Dilini Singappuli-Arachchige, [1,2,†] Bosky L. Parikh[1,2], Igor I. Slowing[1,2]

[1]US DOE Ames Laboratory, Ames, Iowa 50011, United States

[2]Department of Chemistry, Iowa State University, Ames, Iowa 50011, United States

[†]These authors contributed equally to this study.

Abstract

Phenyl-functionalized mesoporous silica materials were used to explore the effect of non-covalent interactions on the release of Ibuprofen into simulated body fluid. Variations in orientation and conformational mobility of the surface phenyl groups were introduced by selecting different structural precursors: 1) a rigid upright orientation was obtained using phenyl groups directly bound to surface Si atoms (Ph-MSN), 2) mobile groups were produced by using ethylene linkers to connect phenyl groups to the surface (PhEt-MSN), and 3) groups co-planar to the surface were obtained synthesizing a phenylene-bridged periodic mesoporous organosilica (Ph-PMO). The Ibuprofen release profiles from these materials and non-functionalized mesoporous silica nanoparticles (MSN) were analyzed using an adsorption-diffusion model. The model provided kinetic and thermodynamic parameters that evidenced fundamental differences in drug-surface interactions between the materials. All phenyl-bearing materials show lower Ibuprofen initial release rates than bare MSN. The conformationally locked Ph-MSN and Ph-PMO have stronger interactions with the drug (negative ΔG of adsorption) than the flexible PhEt-MSN and bare MSN (positive ΔG of adsorption). These differences in strength of

adsorption are consistent with differences between interaction geometries obtained from DFT calculations. B3LYP-D3-optimized models show that π-π interactions contribute more to drug adsorption than H-bonding with silanol groups. The results suggest that the type and geometry of interactions control the kinetics and extent of drug release, and should therefore serve as a guide to design new drug delivery systems with precise release behaviors customized to any desired target.

Introduction

Advancements in drug delivery systems (DDS) are of utmost importance to the development of the pharmaceutical and biomedical fields. One of the key properties of advanced DDS is the ability of releasing drug molecules in a controlled fashion. In this respect, mesoporous silicas have been extensively studied as promising DDS because in addition to their biocompatibility, controllable pore structure, large pore volumes and surface areas, they can be functionalized with a wide variety of moieties.[1-5] These properties have enabled the design of gated DDS that release their cargo upon application of specific stimuli like radiation, changes in pH, temperature, redox potentials, magnetic fields, or signaling molecules.[6-12] Furthermore, these materials have also been modified with receptors, antibodies, or aptamers to provide targeting capabilities, and with reactive moieties to control cell internalization and endo/lysosomal escape.[13-18]

In spite of all these sophisticated designs and their successful *in vitro* and *in vivo* applications,[19-21] little attention has been paid to the influence of drug-surface interactions on the extent and kinetics of release. Moreover, our understanding of the role of organic moieties on surface-solvent partition equilibria and diffusion rates of the loaded drugs is fairly limited and often overlooked. This is surprising given the importance usually attributed to the high surface area and the ability to tailor the surface chemistry of these materials. Initial efforts to determine

the effects of surface groups on the performance of mesoporous silica DDS were conducted by Vallet-Regí and co-workers when studying Erythromycin release as a function of alkyl substitution.[22] Their results showed that release was affected by surface hydrophobicity, and suggested that partition equilibria between the surface and the media controlled drug discharge. More recently, Berger and collaborators investigated the effects of group functionalities on the release of Metoprolol from mesoporous silica.[23] They observed a correlation between functional group pK_a and the amount of drug released, suggesting that electrostatic interactions controlled release rates. Interestingly, computational studies by Ugliengo and co-workers suggested that even weak interactions can determine drug release. Their simulations showed that London dispersion forces play a more important role than H-bonding in the adsorption of Ibuprofen on the silica surface.[24, 25] However, NMR and relaxation dielectric spectroscopy studies have shown that the interaction of Ibuprofen with the silica surface is so weak that only a fraction of the drug is adsorbed to the pore walls and the rest exists as highly mobile species.[26-31] Thus, one can expect that producing gradual enhancements of the drug-silica interactions may allow fine-tuning drug release.

Herein, with the aim of enabling precise control of drug release rates, we explore the potential role of non-covalent interactions on the behavior of mesoporous silica-based DDS. Specifically, we investigate the effect of π-π interactions between Ibuprofen and surface-immobilized phenyl groups on its release kinetics from silica carriers. To this end, we produced phenyl-functionalized mesoporous silicas with different structural features, namely: 1) mesoporous silica nanoparticles (MSN) with phenyl groups directly bound to silicon atoms (Ph-MSN) where groups are rigid and upright, 2) MSN with phenyl groups attached via flexible ethylene linkers (PhEt-MSN) where groups have conformational mobility, and 3) phenylene-

bridged periodic mesoporous organosilica (Ph-PMO) where the phenyl group is co-planar to the pore surface (Scheme 1). We compared the Ibuprofen release profiles from these materials and non-functionalized MSN to assess the effects of orientation (perpendicular versus co-planar to the pore walls) and conformational flexibility on the strength of interactions and release kinetics of the drug. By fitting the release profiles to a three-parameter kinetic model developed by Zeng and Wu, we characterized the thermodynamics of surface-solvent partition and the diffusion kinetics of the desorbed molecules from the pores to the bulk media.[32, 33] Finally, we pursued an atomistic level understanding of the interactions via computational modeling of drug-surface complexes using a silica surface model developed by Ugliengo and co-workers.[34, 35]

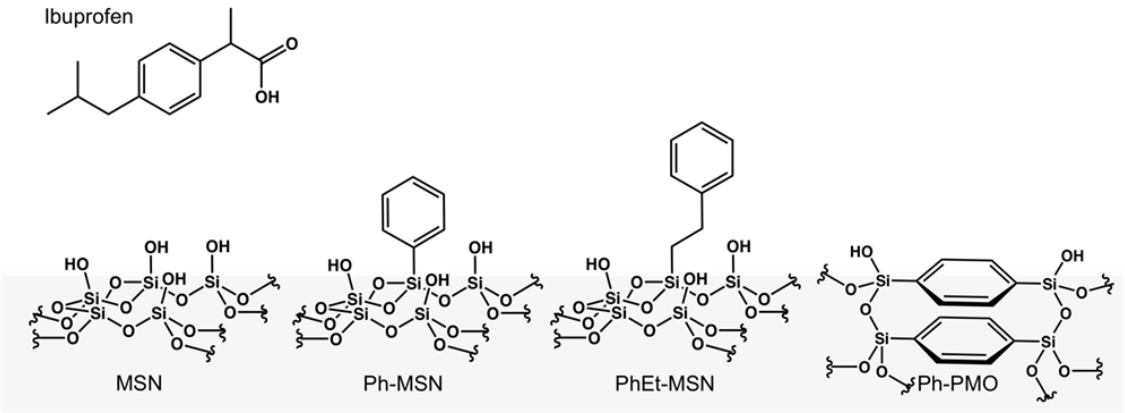

Scheme 1. Structure of Ibuprofen and surface functionalities of the four mesoporous silica based DDS.

Results and Discussion

Material synthesis and characterization

To explore the effects of non-covalent interactions, group orientation and conformational flexibility on Ibuprofen release, MCM-41 type mesoporous silica nanoparticles (MSN) functionalized with phenyl (Ph-MSN) and phenethyl (PhEt-MSN) groups, and phenylene-bridged periodic mesoporous organosilica (Ph-PMO) were synthesized. Non-functionalized MSN was also prepared as a control (Scheme 1).

Characterization of the materials by nitrogen physisorption and x-ray diffraction revealed that the organic groups have no significant effects on the textural properties and pore geometry of the MSN samples. While all the MSN materials have similar surface areas (around 1200 $m^2 g^{-1}$), the surface of Ph-PMO is about 30% lower (807 $m^2 g^{-1}$) (Table 1, Fig. S1). However, the pore width distributions of all materials are very similar (centered at 2.6 – 3.0 nm), and all of them have 2D hexagonal arrays of pores as evidenced by XRD patterns and TEM images (Fig. S2, S3). While the loadings of phenyl groups are very similar for Ph-MSN and PhEt-MSN based on CHN elemental analysis, Ph-PMO has a much higher number of groups because its only precursor is the bis-siloxy-benzene.

The relative polarities of the pore surfaces were measured to determine if material hydrophobicity controls Ibuprofen release. Pore polarities were assessed via fluorescence spectroscopy of the impregnated molecular probe Prodan, as reported before (Table 1, Fig. 1, S4).[36] Because of the lack of organic moieties, the silanol-rich non-functionalized MSN has a much higher interfacial polarity than the other materials. Interestingly, Ph-MSN has a higher polarity than PhEt-MSN, likely due to the differences in flexibility of the two surface groups. While the rigid Ph groups in Ph-MSN expose the surface silanols allowing their contribution to the interfacial polarity, the flexible PhEt can bend over the surface and mask some of the polar silanols to decrease their contribution.[43] Interestingly, in spite of the larger amount of phenyl groups in Ph-PMO, its relative polarity is very similar to that of PhEt-MSN. This result supports the idea that the phenyl groups in PhEt-MSN may lay flat on the surface covering a fraction of silanols thus giving a balance of hydrophobic-hydrophilic groups comparable to that of Ph-PMO.

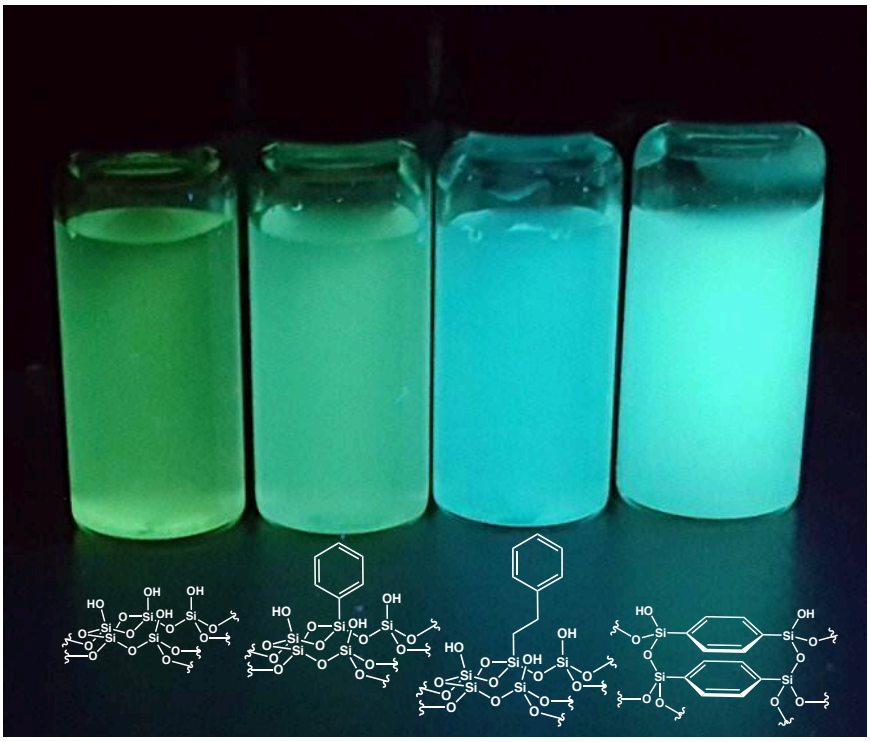

Figure 1. Photograph of aqueous suspensions of (left to right) MSN, Ph-MSN, PhEt-MSN, and Ph-PMO loaded with the solvatochromic fluorophore Prodan. Interfacial polarity is proportional to the wavelength of emission (i.e. green and blue indicate high and low polarity respectively).36

FTIR analysis of the materials (Fig. S5) evidenced features common to all of them, including the characteristic intense peaks centered at ca. 1090 cm^{-1} and 3400 cm^{-1} assigned to Si–O–Si and –O–H stretching vibrations respectively, the latter corresponding to H-bonding silanols and physisorbed water. Presence of water in all the materials is confirmed by a clear signal of the scissor bending vibration at 1630 cm^{-1}. The organic groups are characterized in Ph-MSN, PhEt-MSN and Ph-PMO by peaks in the 3000 – 3100 cm^{-1} region corresponding to aromatic C–H stretching vibrations, and 1380 – 1420 cm^{-1} region attributed to aromatic ring vibrations and Si–C stretching. These signals are much better defined in Ph-PMO due to the larger number of organic groups in the material. Additional absorption between 2900 and 3000 cm^{-1} is visible for PhEt-MSN corresponding to the aliphatic C–H bonds of the ethylene groups.

Table 1. Physicochemical properties of the materials.

	S_{BET} (m^2 g^{-1})	W_{BJH} (nm)	Relative polarity[a]	Phenyl groups (mmol g^{-1})[b]
MSN	1262	3.0	1.00 ± 0.01	--
Ph-MSN	1221	2.6	0.84 ± 0.02	1.2
PhEt-MSN	1196	2.6	0.69 ± 0.01	1.0
Ph-PMO	807	2.8	0.72 ± 0.01	3.2[c]

[a]Determined by fluorescence measurement of solvatochromic probe Prodan.[36]
[b]Determined by CHN elemental analysis. [c]Estimated from the surface area of the material and its structural model.[44]

Ibuprofen loading

Ibuprofen was loaded into the materials via incipient wetness impregnation to facilitate drug penetration into the pores by capillary action.[45] The amount loaded (0.5 mmol g^{-1}) was selected to ensure there were plenty of phenyl groups in the materials to interact with the drug. Drug loading is confirmed by FTIR analysis of the impregnated materials which show a clear absorption band at 1710 cm^{-1} corresponding to the C=O stretching of Ibuprofen (Fig 2). This signal is red-shifted by ca. 14 cm^{-1} in all of the loaded materials with respect to the pure drug suggesting interaction of the group with the surface, likely via hydrogen bonding with silanol groups.[26] Smaller blue shifts in ring vibration bands (1462 to 1467 cm^{-1} and 1508 to 1514 cm^{-1}) suggest that the aromatic group is either interacting with the surface or its mobility is significantly restricted likely due to confinement in the porous materials.[46-48] Wide angle XRD analysis of the drug-loaded materials does not show crystalline Ibuprofen reflections in any of the materials (Fig. S6), which is consistent with previous reports and has also been attributed to confinement of the drug into the pores.[26]

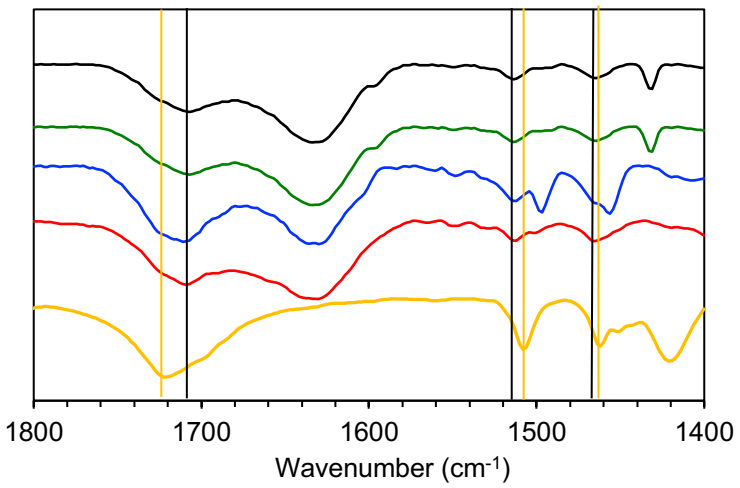

Figure 2. FTIR spectra of Ibuprofen-loaded MSN (black), Ph-MSN (green), PhEt-MSN (blue) and Ph-PMO (red). Spectrum of the free drug (KBr pellet) is in yellow.

Ibuprofen release from different MSN

The release of Ibuprofen from the materials to simulated body fluid (SBF) was monitored via UV-visible spectroscopy (λ = 263 nm). The drug-loaded materials were set in a dialysis bag (MW cutoff = 12–14 kDa) and immersed in SBF (Fig. S7). The solution was continuously circulated through a quartz flow cuvette and spectra were acquired every 5 min for 20 h.

The average Ibuprofen release profiles indicate a clear dependence on the functionality of the silica materials (Fig. 3, Table 2). Some of the most relevant differences between the profiles include: 1) only MSN and PhEt-MSN reach a plateau within the experimental timeframe (less than 1% change after 12 and 16 h, respectively), 2) MSN and Ph-MSN show the largest cumulative release after 20 h (ca. 82 ± 3% and 81 ± 4%, respectively), 3) MSN presents a higher initial release rate than the other materials, all of which present the same values (0.44 versus 0.25 mM h^{-1} respectively), 4) while all the phenyl-bearing materials give the same initial rates, PhEt-MSN sustains it for a longer time (2 h) than Ph-MSN (1.5 h) and Ph-PMO (0.5 h). These differences indicate that the phenyl groups indeed have an effect on the adsorption and retention

of Ibuprofen, and are consistent with the phenyl-bearing materials having lower polarity (i.e. more hydrophobicity) than the non-functionalized MSN. However, the differences observed between the drug release profiles of all the phenyl-functionalized materials cannot be explained by hydrophobicity alone. The different release profiles from these materials must be due to significant variations in the drug-surface interactions at the molecular level, which are likely regulated by the relative orientation and flexibility of binding sites on the surface.

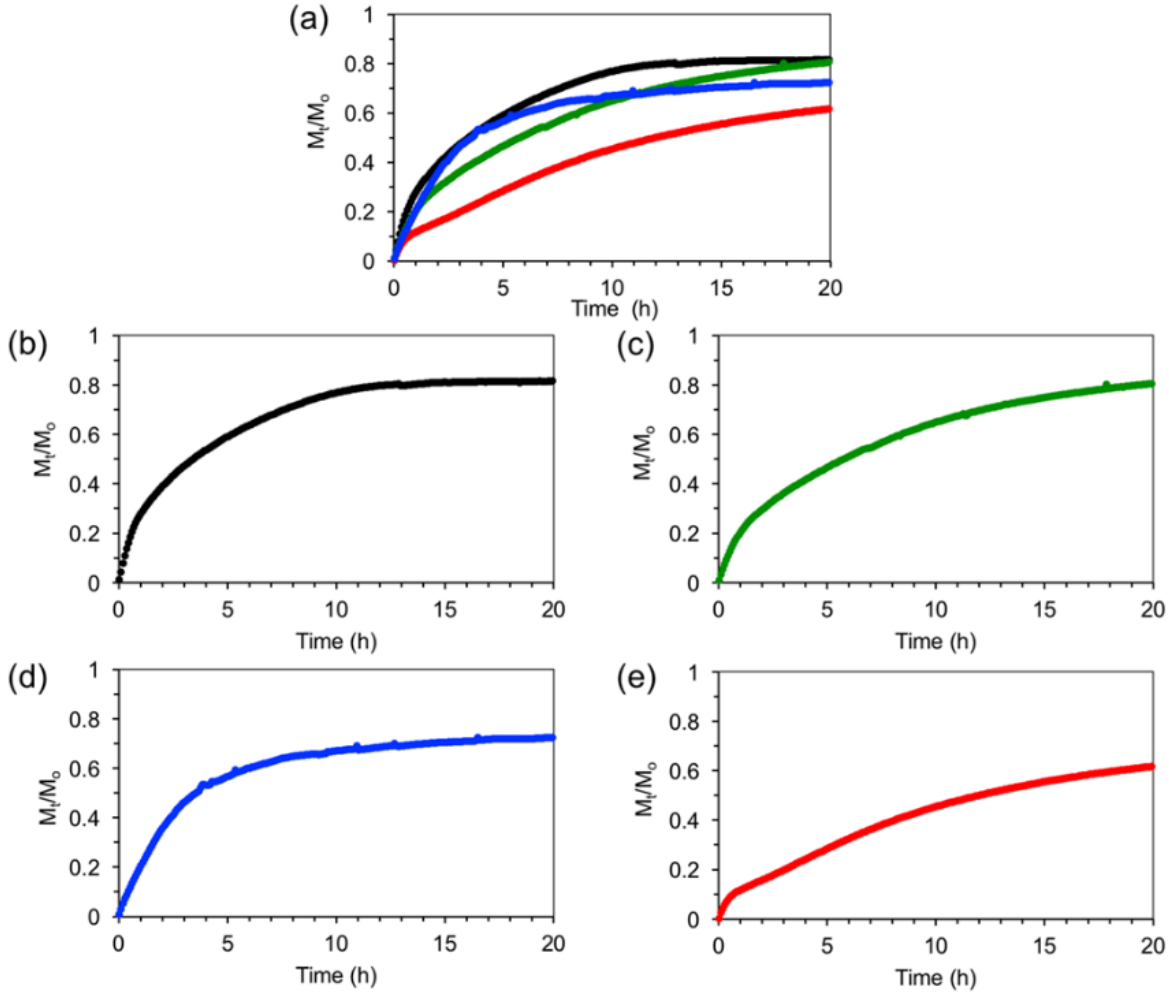

Figure 3. Average release profiles of Ibuprofen from the DDS. Mt/Mo is the fraction of Ibuprofen released at a given time t. (a) Overlaid profiles of all materials. (b-e) Individual profiles: (b) MSN (black), (c) Ph-MSN (green), (d) PhEt-MSN (blue), (e) Ph-PMO (red). The colors in (a) correspond to those in (b-e).

Table 2. Descriptors of Ibuprofen release from the mesoporous materials.

Material	20 h release (%)	Initial rate (mM h^{-1})	Initial rate regime (h)
MSN	82 ± 3	0.44	0.8
Ph-MSN	81 ± 4	0.25	1.5
PhEt-MSN	73 ± 2	0.25	2.0
Ph-PMO	62 ± 4	0.25	0.5

Kinetic and thermodynamic analysis of Ibuprofen release

To better understand the differences between the materials the drug release data were fitted to a kinetic model developed by Wu and co-workers.[49] The model deconvolutes the contributions of pore diffusion and drug-support interactions from the release profiles, and is defined by three fundamental parameters: the diffusion/convection rate constant (k_s), and the rate constants for adsorption (k_{on}) and desorption (k_{off}) of the drug from the support. The experimental release profiles are fitted to the model equation:

$$\frac{M_t}{M_0} = \frac{k_{off}}{k_{on}+k_{off}}(1 - e^{-k_s t}) + \frac{k_{on}}{k_{on}+k_{off}}(1 - e^{-k_{off} t}) \qquad (1)$$

where M_t and M_0 are the cumulative drug release at time t and the initial drug amount, respectively, and the kinetic constants k_s, k_{on}, and k_{off} are defined as above. In addition, the partition equilibrium between the surface and the solvent is defined by the ratio k_{on}/k_{off}, and the associated free energy change that controls the burst-release phase is related to this ratio by:

$$\Delta G = -k_B\, T\, ln(\frac{k_{on}}{k_{off}}) \qquad (2)$$

where k_B is the Boltzmann constant and T the absolute temperature. Fitting of the average release profiles to equation (1) gives high correlation coefficients ($R^2 > 0.98$ for each profile, Fig. S8), and provides kinetic constants for Ibuprofen release from each material (Table 3).

Table 3. Kinetic and thermodynamic parameters for the release of Ibuprofen from all of the materials.

	k_s (h^{-1})	k_{on} (h^{-1})	k_{off} (h^{-1})	$\Delta G \times 10^{21}$ (J)
MSN	0.377 ± 0.012	0.019 ± 0.003	0.037 ± 0.003	2.80 ± 1.44
Ph-MSN	0.836 ± 0.031	0.227 ± 0.007	0.074 ± 0.0005	-4.63 ± 0.04
PhEt-MSN	0.376 ± 0.003	0.005 ± 0.0004	0.010 ± 0.0006	2.71 ± 0.72
Ph-PMO	0.242 ± 0.019	0.104 ± 0.016	0.035 ± 0.001	-4.47 ± 0.22

The sign of ΔG is indicative of the strength of interaction between the surface and the drug. The positive ΔG for MSN and PhEt-MSN indicates that desorption of the drug from the surface is favored ($k_{off} > k_{on}$) leading to the burst type release observed in Fig. 3b,d. To the contrary, ΔG for Ph-MSN and Ph-PMO is negative, indicating strong interactions with the drug that hinder desorption ($k_{off} < k_{on}$), and is reflected by a more sustained type of release (Fig. 3c,e). While ΔG of Ibuprofen with Ph-MSN indicates a strong adsorption, its cumulative release after 20 h is the same as MSN and higher than PhEt-MSN, both of which have weaker interactions with the drug. The magnitude of the cumulative release is proportional to the rate of diffusion from the pores to the SBF media (k_s), which is also higher for Ph-MSN than for MSN and PhEt-MSN. This apparent contradiction between the difference in strength of interaction and the diffusion kinetics and cumulative drug release from these materials is explained by examining the magnitudes of k_{on} and k_{off}. While the ratio of these two parameters favors adsorption for Ph-MSN, both k_{on} and k_{off} are significantly higher indicating that the drug exchanges quickly between adsorbed and desorbed state in this material, which leads to a higher probability of reaching the end of the pores and escape to the surrounding SBF solution. This also explains why PhEt-MSN, despite having the same k_s and ΔG as MSN, gives a lower cumulative 20 h release: the much lower adsorption and desorption rate constants decrease the probabilities of the drug reaching the end of the pores for discharge into SBF.

Computational modeling of Ibuprofen-surface interactions

DFT calculations were performed to understand the differences between the interaction of Ibuprofen with the mesoporous materials. For the functionalized MSNs, the models used were based on a silica slab reported by Ugliengo and collaborators.[34, 35] The different surfaces were modified with the respective organic groups and optimized using the hybrid QM/MM SIMOMM method.[42] The Ph-PMO structure was produced based on the model developed by Martinez and Pacchioni.[40]

The possible interactions of Ibuprofen with the materials' surfaces are H-bonding between –COOH and silanol groups, and π-π interactions between the phenyl rings in the drug and the rings on the surface. The optimized structures showed a significant difference in the O-H distances corresponding to H-bonds between the non-functionalized MSN (1.97 Å) and phenyl-bearing materials (Ph-MSN 1.76 Å and PhEt 1.72Å) (Fig. 4, S9). This suggests a weaker interaction of the former with the surface, a result that is consistent with the highest experimental rate and extent of release observed for MSN.

While the slightly shorter O-H distance in PhEt-MSN than Ph-MSN would suggest a stronger interaction of the drug with the former, the ΔG of adsorption derived from their release profiles indicate the opposite behavior. However, as pointed out by Ugliengo *et al.*, H-bonding is not the dominant interaction between Ibuprofen and a silica surface.[24] Thus, it is likely that the experimental differences observed between the release profiles of Ibuprofen from these two materials are due to π-π interactions between the aromatic rings. Further analysis of the optimized complexes reveals differences in the relative positions of the phenyl groups in the drug with respect to the surface phenyl groups (Fig. S10). While there are clear deviations from ideal stacking in all of the interacting pairs, the misalignment with the ring in Ibuprofen is larger in PhEt-MSN: the average distances between aromatic carbons of the rings are longer (4.89 Å

versus 4.56 Å) and the diverging angle is wider (39° versus 28°) than in Ph-MSN (Fig. S10). These differences in interaction geometries are likely the main reason for the more favorable ΔG of adsorption of the drug with Ph-MSN, and for the observed differences in drug release profiles between the materials.

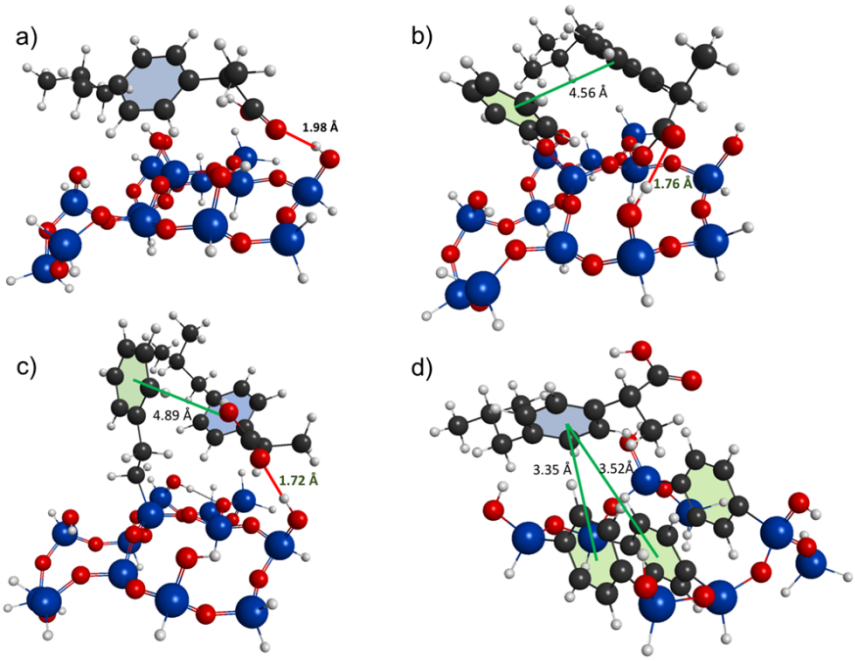

Figure 4. QM section of the optimized structures of Ibuprofen interacting with (a) MSN, (b) Ph-MSN, (c) PhEt-MSN, and (d) Ph-PMO. For clarity, the surface phenyl rings are shaded green and the Ibuprofen phenyl rings are shaded blue.

While the slightly shorter O-H distance in PhEt-MSN than Ph-MSN would suggest a stronger interaction of the drug with the former, the ΔG of adsorption derived from their release profiles indicate the opposite behavior. However, as pointed out by Ugliengo *et al.*, H-bonding is not the dominant interaction between Ibuprofen and a silica surface.[24] Thus, it is likely that the experimental differences observed between the release profiles of Ibuprofen from these two materials are due to π-π interactions between the aromatic rings. Further analysis of the optimized complexes reveals differences in the relative positions of the phenyl groups in the drug

with respect to the surface phenyl groups (Fig. S10). While there are clear deviations from ideal stacking in all of the interacting pairs, the misalignment with the ring in Ibuprofen is larger in PhEt-MSN: the average distances between aromatic carbons of the rings are longer (4.89 Å versus 4.56 Å) and the diverging angle is wider (39° versus 28°) than in Ph-MSN (Fig. S10). These differences in interaction geometries are likely the main reason for the more favorable ΔG of adsorption of the drug with Ph-MSN, and for the observed differences in drug release profiles between the materials.

Analysis of Ph-PMO indicates much shorter distances between its phenyl rings and those of the drug (3.35 and 3.52 Å). In addition, while the π-π interactions of Ibuprofen with Ph-MSN and PhEt-MSN tend to be face-to-face, the relative orientation of the rings in the drug-Ph-PMO model indicates the interaction is edge-to-face. Because of the quadrupolar nature of phenyl rings, edge-to-face interactions are generally stronger than face-to-face.[50] These results suggest that the interaction of the drug with Ph-PMO must be stronger than with Ph-MSN and PhEt-MSN, and are in agreement with the negative ΔG and lowest rate and extent of Ibuprofen release observed for this material.

Materials and Methods

Materials

Hexadecyltrimethylammonium bromide (CTAB), Brij 76 ($C_{18}EO_{10}$) and Ibuprofen were purchased from Aldrich. Tetraethylorthosilicate (TEOS), phenyltrimethoxysilane, phenethyltrimethoxysilane and 1,4-bis(triethoxysilyl) benzene were purchased from Gelest, Inc. NaOH, NaCl, KCl, K_2HPO_4, $MgCl_2{\cdot}6H_2O$, $CaCl_2$, Na_2SO_4, Tris(hydroxymethyl)aminomethane, conc. HCl and acetone were purchased from Fisher Scientific. $NaHCO_3$ was from Alfa Aesar, and Prodan from Anapec, Inc. All chemicals were used as received without any further purification.

Synthesis of MSN

CTAB (1.0 g, 2.74 mmol) was dissolved in deionized water (480 ml) in a round bottom flask followed by addition of 2 M NaOH (3.5 mL, 7.0 mmol). The solution was stirred for 1 h at 80 °C. TEOS (5.0 mL, 22.6 mmol) was then added drop wise over 5 min to the CTAB solution. Magnetic stirring was continued for another 2 h at 80 °C. The solution was filtered, washed with abundant water and methanol, and vacuum dried overnight. CTAB was removed by refluxing 1.0 g of dry solid with 100 mL of methanol and conc. HCl (0.8 mL, 9.7 mmol) at 60 °C for 6 h. The surfactant removal step was repeated. The surfactant-removed sample was then filtered, washed with abundant methanol and vacuum dried overnight.

Synthesis of phenyl (Ph-MSN) and phenethyl (PhEt-MSN) substituted MSN

CTAB (1.0 g, 2.74 mmol) was dissolved in deionized water (480 ml) in a round bottom flask followed by addition of 2 M NaOH (3.5 mL, 7.0 mmol). The solution was stirred for 1 h at 80 °C. TEOS (5.0 mL, 22.6 mmol) and phenyltrimethoxysilane (0.19 mL, 1.0 mmol) for Ph-MSN or phenethyltrimethoxysilane (0.22 mL, 1.0 mmol) for PhEt-MSN were then added drop wise over 7 min to the CTAB solution. Magnetic stirring was continued for another 2 h at 80 °C. The solution was filtered, washed with abundant water and methanol respectively, and vacuum dried overnight. CTAB template was removed by refluxing 1.0 g of dry solid with 100 mL of methanol and conc. HCl (0.8 mL, 9.7 mmol) at 60 °C for 6 h. The surfactant removal step was repeated. The surfactant-removed samples were then filtered, washed with abundant methanol and vacuum dried overnight.

Synthesis of phenyl bridged periodic mesoporous organosilica (Ph-PMO)

Brij 76 (0.5 g, 0.703 mmol) was dissolved in 2 M HCl (12.5 mL, 25.0 mmol) and distilled water (2.5 mL) in a round bottom flask with continuous magnetic stirring for 30 min at 50 °C. 1,4-Bis(triethoxysilyl) benzene (1.04 mL, 2.63 mmol) was then added to the mixture and

the stirring was continued for another 20 h at 50 °C. The solid product was collected via filtration and was air-dried for 24 h. The surfactant template was removed by refluxing 1.0 g of dry solid with 150 ml of ethanol and conc. HCl (1.69 mL, 20.3 mmol) at 50 °C for 5 h. The surfactant removal step was repeated one more time. The final product was filtered, air-dried, and further dried under vacuum overnight.

Characterization

XRD patterns were recorded on a Bruker X–ray diffractometer using Cu Kα radiation (40 kV, 44 mA) over the range of 1–50 2θ degrees. Nitrogen sorption isotherms were measured on a Micromeritics Tristar surface area and porosity analyzer. The surface area and pore size distribution were calculated by the Brunauer Emmett Teller (BET) and Barrett Joyner Halenda (BJH) methods respectively. Elemental analyses of the dry samples were done by triplicate on a Perkin Elmer 2100 series II CHNS analyzer, using acetanilide as calibration standard and combustion and reduction temperatures of 925 °C and 640 °C respectively. Transmission Electron Microscopy (TEM) images were obtained using a FEI Tecnai G2 F20 scanning transmission electron microscope operating at 200 kV. TEM samples were prepared by placing 2-3 drops of dilute methanol suspensions onto a carbon-coated copper grid. Transmission mode FTIR measurements were made on a Bruker Vertex 80 FT-IR spectrometer equipped with a HeNe laser and photovoltaic MCT detector and OPUS software. Samples were mixed at ca. 2 wt% with KBr and pressed into pellets for analysis.

Relative polarity measurements of samples were done according to a previously published method.[36] A solution of Prodan in acetone (10 μL, 1.0 mM) was added to the samples (10.0 mg each), grinded, let dry, and suspended in water (2.0 mL). Fluorescence measurements of the suspensions were recorded in a Cary Eclipse Fluorescence Spectrophotometer. Excitation wavelength was set at 337 nm and both excitation and emission slit widths were set at 5 nm.

Obtained fluorescence curves were fitted in origin pro using a Gaussian distribution model. Maximum fluorescence emission wavelength of each sample was used to assign relative polarities based on probe fluorescence in reference solvents.[36]

Impregnation of Ibuprofen into mesoporous materials

Ibuprofen was introduced into the pores via incipient wetness impregnation. In brief, the mesoporous materials (30.0 mg each) were ground to a fine powder using a pestle in an agate mortar. A fresh solution of Ibuprofen in acetone (30 µL, 0.5 M) was then added dropwise to each material, and the mixture was ground until seemingly dry. The impregnated materials were then oven-dried to remove excess acetone, and then dried overnight under vacuum.

Preparation of simulated body fluid (SBF) solution

This solution was prepared following the literature.[37] NaCl (7.996 g, 0.14 mmol), $NaHCO_3$ (0.350 g, 0.0042 mmol), KCl (0.224 g, 0.0030 mmol), K_2HPO_4 (0.174 g, 0.001 mmol), $MgCl_2{\bullet}6H_2O$ (0.305 g, 0.0015 mmol), 1M HCl (40.0 mL, 0.04 mmol), $CaCl_2$ (0.278 g, 0.0025 mmol), Na_2SO_4 (0.071 g, 0.0050 mmol), and tris(hydroxymethyl) aminomethane (6.057 g, 0.05 mmol) were dissolved in deionized water (500 mL) one by one in the above mentioned order in a 1L polyethylene bottle while stirring at 36.5 ºC. The pH of the solution was adjusted to 7.40 using a 1M HCl solution. The total volume of the solution was then adjusted to 1L by adding deionized water and shaking at 20 °C. The prepared SBF solution was stored in a refrigerator at 5 °C.

Ibuprofen release experiments

The Ibuprofen-loaded samples (30.0 mg each) were introduced into a dialysis membrane (Spectrum Labs, MW cutoff = 12-14 kDa) and immersed into SBF (10.0 mL). The intact SBF solution was continuously circulated through a quartz flow cuvette, and the absorption band at

263 nm was monitored for 20 h via UV-vis spectroscopy, taking scans every 5 min. Three separate release experiments were performed for each material, and the results were averaged.

Computational methods

All calculations were performed using the dispersion-corrected B3LYP-D3[38] method implemented in the GAMESS[39] package using the 6-311G(d,p) basis set. Three different surfaces were optimized using the MCM-41 model developed by Ugliengo and collaborators.[34] The surfaces consisted of bare MCM-41 silica, and MCM-41 silica substituted with a phenyl group and with a phenethyl group. Ph-PMO was modeled based on previous work by Martinez and Pacchioni.[40] The structure corresponds to a sequence of six and four membered rings of organosilica tetrahedra with T3:T2 ratio of 2:1, based on the solid state NMR study by Comotti *et al*.[41] All of the models were optimized using the QM/MM SIMMOM[42] implemented in GAMESS, using the B3LYP-D3 functional with a 6-311(d,p) basis set.

Conclusions

In summary, the kinetics and cumulative release of Ibuprofen from mesoporous silica DDS can be controlled by modification of the carrier's surface with phenyl groups. The presence of phenyl groups on the surface decreases the initial rate of release, in principle due to a decrease in interfacial polarity that affects the partition equilibrium between the surface and the aqueous SBF. Controlling the orientation and conformational flexibility of the surface phenyl groups uncovers subtle differences in intermolecular interactions that allow further fine-tuning the drug release profiles. At the molecular level, incorporation of phenyl groups on silica surfaces results in stronger drug-surface interactions arising from cooperativity between COOH-silanol H-bonding and π-π interactions with the surface phenyl groups. The negative ΔG of Ph-MSN and positive ΔG of PhEt-MSN suggest that π-π interactions contribute more to Ibuprofen adsorption than H-bonding, because the former has closer and better phenyl ring alignment but longer O-H

distances than the latter. While these two systems possess silanols and phenyl rings, it appears that the locked conformation of phenyl groups in Ph-MSN provides a better fit for Ibuprofen docking than the phenyl groups with mobile ethylene linkers in PhEt-MSN. This conformational rigidity of Ph-MSN appears to facilitate a rapid drug adsorption/desorption equilibrium evidenced by the large k_{on} and k_{off} values that eventually lead to a high cumulative release after long contact times. In contrast to Ph-MSN and PhEt-MSN where the phenyl rings of Ibuprofen tend to interact face-to-face, the π-π interaction of the drug with Ph-PMO seems to be edge-to-face. This type of interaction in Ph-PMO is stronger than the face-to-face and explains the slower kinetics and cumulative release of Ibuprofen observed for this material. These results demonstrate that careful selection and design of drug-surface interactions can be a valuable tool to precisely tune the sustained release of drugs for custom therapeutic applications.

Acknowledgements

This research is supported by the U.S. Department of Energy, Office of Basic Energy Sciences, Division of Chemical Sciences, Geosciences, and Biosciences, through the Ames Laboratory Catalysis Science program. The Ames Laboratory is operated for the U.S. Department of Energy by Iowa State University under Contract No. DE-AC02-07CH11358.

Supplemental Tables and Figures

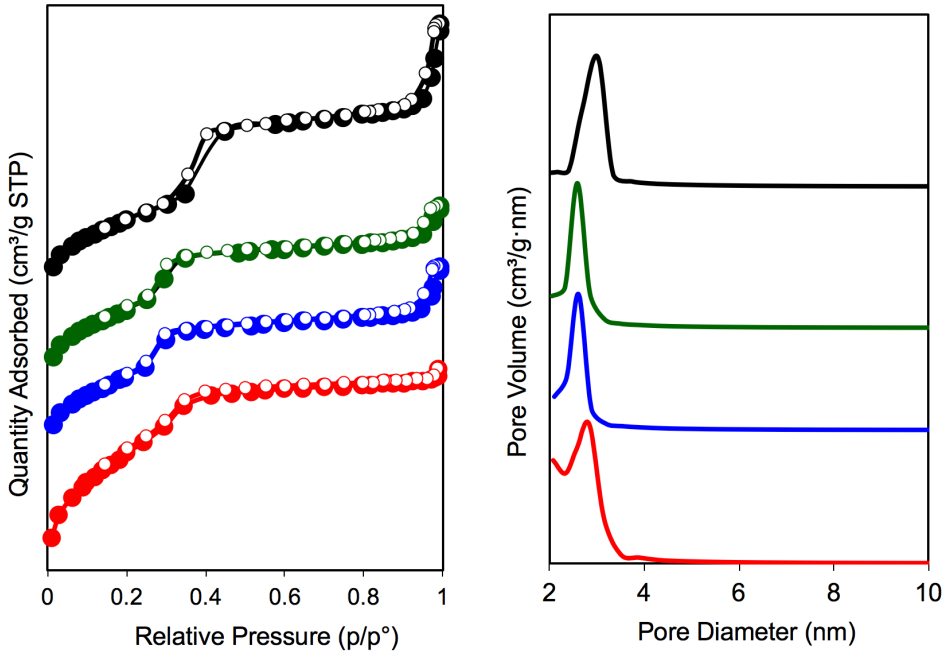

Figure S1. (a) N2 sorption isotherms and (b) pore size distributions of MSN (black), Ph-MSN (green), PhEt-MSN (blue) and Ph-PMO (red). Figures are shifted for clarity.

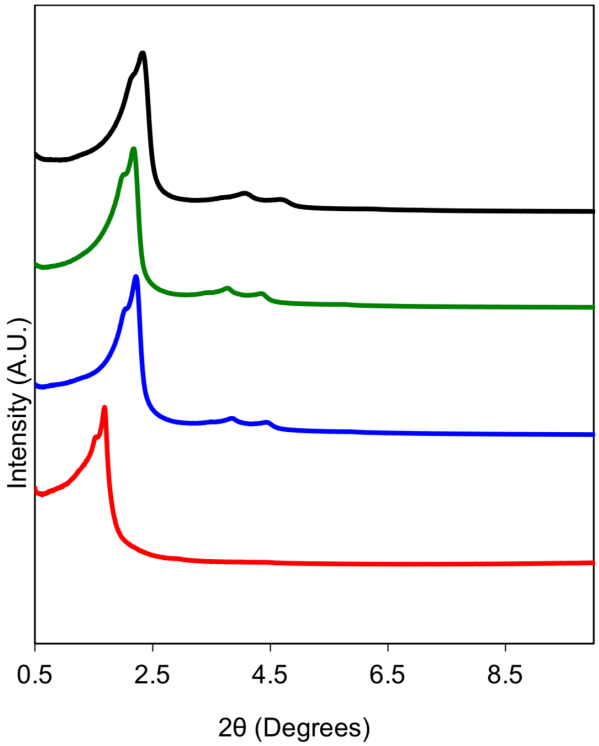

Figure S2. XRD patterns of MSN (black), Ph-MSN (green), PhEt-MSN (blue) and Ph-PMO (red). Figures are shifted for clarity.

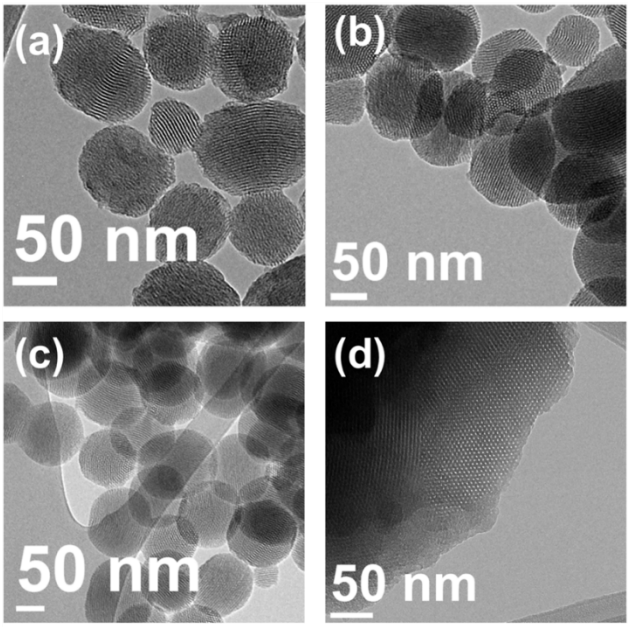

Figure S3. Transmission electron micrographs of (a) MSN, (b) Ph-MSN, (c) PhEt-MSN and (d) Ph-PMO.

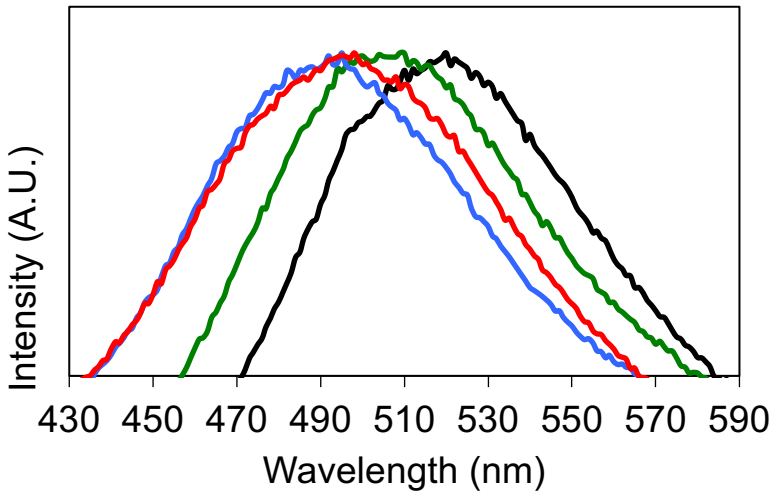

Figure S4. Fluorescence emission spectra of aqueous suspensions of Prodan-loaded MSN (black), Ph-MSN (green), PhEt-MSN (blue) and Ph-PMO (red). Excitation wavelength: 337 nm.

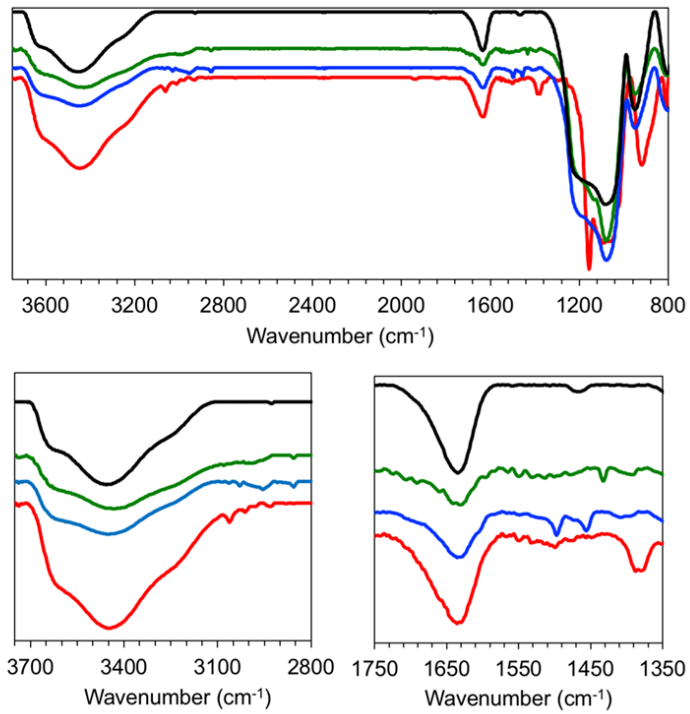

Fig. S5. Different regions of the FT-IR spectra of MSN (black), Ph-MSN (green), PhEt-MSN (blue) and Ph-PMO (red).

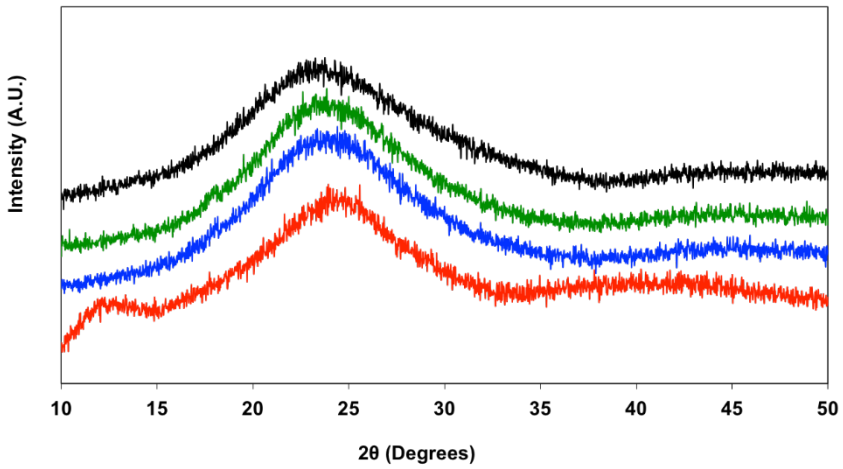

Figure S6. Wide angle XRD patterns of Ibuprofen(0.5 mmol/g) loaded MSN (black), Ph-MSN (green), PhEt-MSN (blue) and Ph-PMO (red).

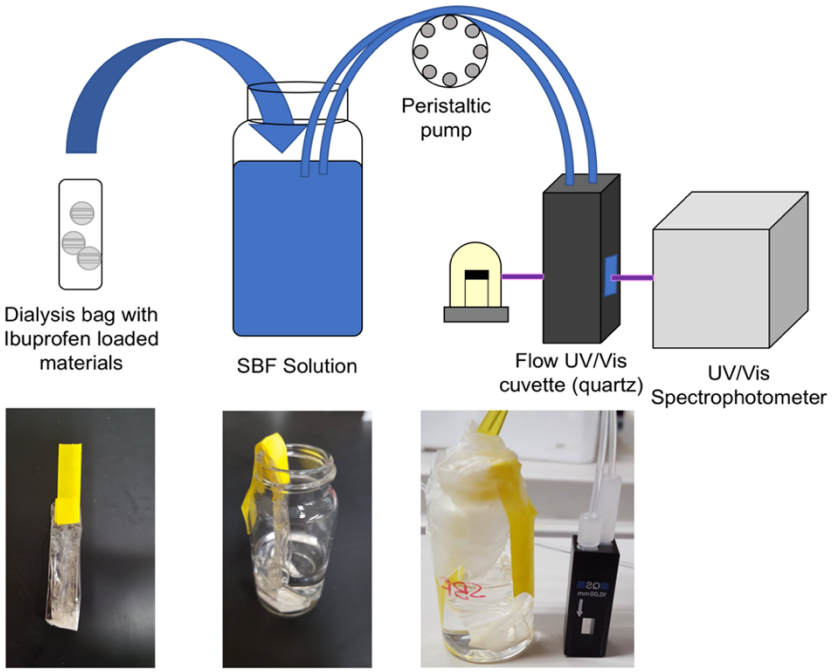

Figure S7. Experimental setup for Ibuprofen release experiments.

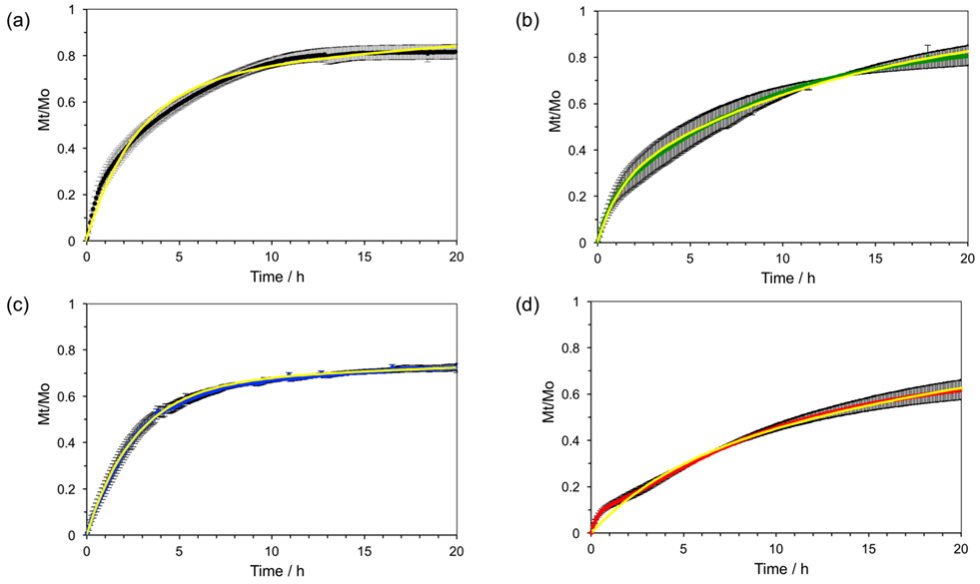

Figure S8. Fitting of the Ibuprofen release profiles from (a) MSN (black), (b) Ph-MSN(green), (c) PhEt-MSN(blue) and (d) Ph-PMO(red) to the 3-parameter thermodynamic model. Fittings are the yellow lines, black lines around each colored datapoint are the error bars consisting of 2 standard deviations from three separate release experiments from each material.

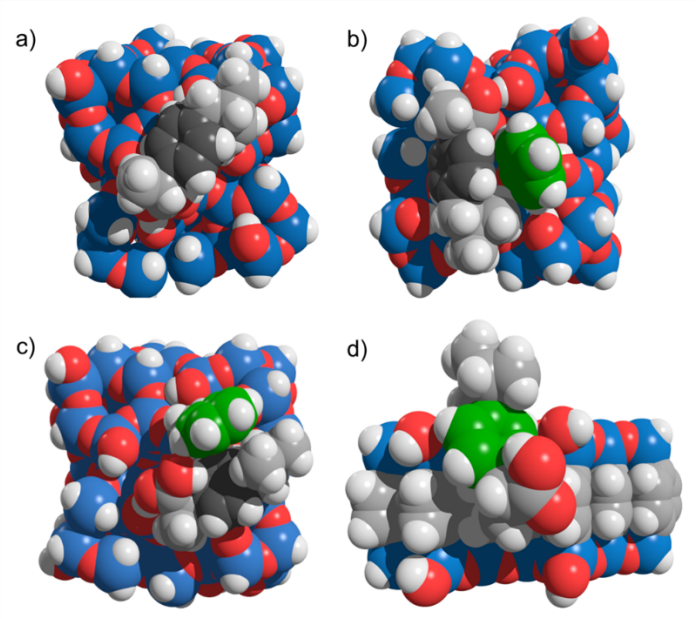

Figure S9. Optimized structures of Ibuprofen adsorbed on the surfaces of (a) MSN, (b) Ph-MSN, (c) PhEt-MSN, and (d) Ph-PMO.

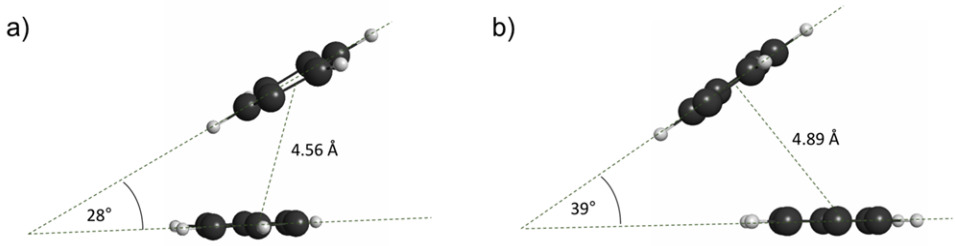

Figure S10. Relative positions of the aromatic ring of Ibuprofen with respect to the interacting aromatic ring in (a) Ph-MSN, (b) PhEt-MSN

References

1. Slowing, I. I.; Vivero-Escoto, J. L.; Trewyn, B. G.; Lin, V. S.-Y., Mesoporous silica nanoparticles: structural design and applications. *J. Mater. Chem.* **2010,** *20* (37), 7924 - 7937.

2. Aznar, E.; Oroval, M.; Pascual, L.; Murguía, J. R.; Martínez-Máñez, R.; Sancenón, F., Gated Materials for On-Command Release of Guest Molecules. *Chem. Rev.* **2016,** *116* (2), 561-718.

3. Tarn, D.; Ashley, C. E.; Xue, M.; Carnes, E. C.; Zink, J. I.; Brinker, C. J., Mesoporous Silica Nanoparticle Nanocarriers: Biofunctionality and Biocompatibility. *Acc. Chem. Res.* **2013,** *46* (3), 792-801.

4. Slowing, I. I.; Vivero-Escoto, J. L.; Wu, C.-W.; Lin, V. S. Y., Mesoporous silica nanoparticles as controlled release drug delivery and gene transfection carriers. *Adv. Drug Deliv. Rev.* **2008,** *60* (11), 1278-1288.

5. Vallet-Regí, M.; Balas, F.; Arcos, D., Mesoporous Materials for Drug Delivery. *Angew. Chem., Int. Ed.* **2007,** *46* (40), 7548-7558.

6. Argyo, C.; Weiss, V.; Bräuchle, C.; Bein, T., Multifunctional Mesoporous Silica Nanoparticles as a Universal Platform for Drug Delivery. *Chem. Mater.* **2013,** *26* (1), 435-451.

7. Gao, W.; Chan, J. M.; Farokhzad, O. C., pH-Responsive Nanoparticles for Drug Delivery. *Molecular Pharmaceutics* **2010,** *7* (6), 1913-1920**.**

8. Tukappa, A.; Ultimo, A.; de la Torre, C.; Pardo, T.; Sancenón, F.; Martínez-Máñez, R., Polyglutamic Acid-Gated Mesoporous Silica Nanoparticles for Enzyme-Controlled Drug Delivery. *Langmuir* **2016,** *32* (33), 8507-8515.

9. Zhao, Y.; Trewyn, B. G.; Slowing, I. I.; Lin, V. S. Y., Mesoporous Silica Nanoparticle-Based Double Drug Delivery System for Glucose-Responsive Controlled Release of Insulin and Cyclic AMP. *J. Am. Chem. Soc.* **2009,** *131* (24), 8398-+.

10. Mortera, R.; Vivero-Escoto, J.; Slowing, II; Garrone, E.; Onida, B.; Lin, V. S. Y., Cell-induced intracellular controlled release of membrane impermeable cysteine from a mesoporous silica nanoparticle-based drug delivery system. *Chem. Commun.* **2009,** (22), 3219-3221.

11. Vivero-Escoto, J. L.; Slowing, I. I.; Wu, C.-W.; Lin, V. S.-Y., Photoinduced Intracellular Controlled Release Drug Delivery in Human Cells by Gold-Capped Mesoporous Silica Nanosphere. *J. Am. Chem. Soc.* **2009,** *131* (10), 3462-3463.

12. Martín-Saavedra, F. M.; Ruíz-Hernández, E.; Boré, A.; Arcos, D.; Vallet-Regí, M.; Vilaboa, N., Magnetic mesoporous silica spheres for hyperthermia therapy. *Acta Biomaterialia* **2010,** *6* (12), 4522-4531.

13. Vivero-Escoto, J. L.; Slowing, II; Lin, V. S. Y., Tuning the cellular uptake and cytotoxicity properties of oligonucleotide intercalator-functionalized mesoporous silica nanoparticles with human cervical cancer cells HeLa. *Biomater.* **2010,** *31* (6), 1325-1333.

14. Slowing, I. I.; Vivero-Escoto, J. L.; Zhao, Y.; Kandel, K.; Peeraphatdit, C.; Trewyn, B. G.; Lin, V. S. Y., Exocytosis of Mesoporous Silica Nanoparticles from Mammalian Cells: From Asymmetric Cell-to-Cell Transfer to Protein Harvesting. *Small* **2011,** *7* (11), 1526-1532.

15. Slowing, I.; Trewyn, B. G.; Lin, V. S. Y., Effect of Surface Functionalization of MCM-41-Type Mesoporous Silica Nanoparticles on the Endocytosis by Human Cancer Cells. *J. Am. Chem. Soc.* **2006,** *128* (46), 14792-14793.

16. Pan, L.; He, Q.; Liu, J.; Chen, Y.; Ma, M.; Zhang, L.; Shi, J., Nuclear-Targeted Drug Delivery of TAT Peptide-Conjugated Monodisperse Mesoporous Silica Nanoparticles. *J. Am. Chem. Soc.* **2012,** *134* (13), 5722-5725.

17. Tsai, C.-P.; Chen, C.-Y.; Hung, Y.; Chang, F.-H.; Mou, C.-Y., Monoclonal antibody-functionalized mesoporous silica nanoparticles (MSN) for selective targeting breast cancer cells. *J. Mater. Chem.* **2009,** *19* (32), 5737-5743.

18. Tu, J.; Wang, T.; Shi, W.; Wu, G.; Tian, X.; Wang, Y.; Ge, D.; Ren, L., Multifunctional ZnPc-loaded mesoporous silica nanoparticles for enhancement of photodynamic therapy efficacy by endolysosomal escape. *Biomater.* **2012,** *33* (31), 7903-7914.

19. Lu, J.; Liong, M.; Li, Z.; Zink, J. I.; Tamanoi, F., Biocompatibility, Biodistribution, and Drug-Delivery Efficiency of Mesoporous Silica Nanoparticles for Cancer Therapy in Animals. *Small* **2010,** *6* (16), 1794-1805.

20. Chen, F.; Hong, H.; Zhang, Y.; Valdovinos, H. F.; Shi, S.; Kwon, G. S.; Theuer, C. P.; Barnhart, T. E.; Cai, W., In Vivo Tumor Targeting and Image-Guided Drug Delivery with Antibody-Conjugated, Radiolabeled Mesoporous Silica Nanoparticles. *ACS Nano* **2013,** *7* (10), 9027-9039.

21. Lee, J. E.; Lee, N.; Kim, T.; Kim, J.; Hyeon, T., Multifunctional Mesoporous Silica Nanocomposite Nanoparticles for Theranostic Applications. *Acc. Chem. Res.* **2011,** *44* (10), 893-902.

22. Doadrio, J. C.; Sousa, E. M. B.; Izquierdo-Barba, I.; Doadrio, A. L.; Perez-Pariente, J.; Vallet-Regi, M., Functionalization of mesoporous materials with long alkyl chains as a strategy for controlling drug delivery pattern. *J. Mater. Chem.* **2006,** *16* (5), 462-466.

23. Mitran, R.-A.; Matei, C.; Berger, D., Correlation of Mesoporous Silica Structural and Morphological Features with Theoretical Three-Parameter Model for Drug Release Kinetics. *J. Phys. Chem. C* **2016,** *120* (51), 29202-29209.

24. Delle Piane, M.; Corno, M.; Pedone, A.; Dovesi, R.; Ugliengo, P., Large-Scale B3LYP Simulations of Ibuprofen Adsorbed in MCM-41 Mesoporous Silica as Drug Delivery System. *J. Phys. Chem. C* **2014,** *118* (46), 26737-26749.

25. Delle Piane, M.; Vaccari, S.; Corno, M.; Ugliengo, P., Silica-Based Materials as Drug Adsorbents: First Principle Investigation on the Role of Water Microsolvation on Ibuprofen Adsorption. *J. Phys. Chem. A* **2014,** *118* (31), 5801-5807.

26. Azaïs, T.; Tourné-Péteilh, C.; Aussenac, F.; Baccile, N.; Coelho, C.; Devoisselle, J.-M.; Babonneau, F., Solid-State NMR Study of Ibuprofen Confined in MCM-41 Material. *Chem. Mater.* **2006,** *18* (26), 6382-6390.

27. Babonneau, F.; Yeung, L.; Steunou, N.; Gervais, C.; Ramila, A.; Vallet-Regi, M., Solid State NMR Characterisation of Encapsulated Molecules in Mesoporous Silica. *Journal of Sol-Gel Science and Technology* **2004,** *31* (1), 219-223.

28. Brás, A. R.; Merino, E. G.; Neves, P. D.; Fonseca, I. M.; Dionísio, M.; Schönhals, A.; Correia, N. T., Amorphous Ibuprofen Confined in Nanostructured Silica Materials: A Dynamical Approach. *J. Phys. Chem. C* **2011,** *115* (11), 4616-4623.

29. Guenneau, F.; Panesar, K.; Nossov, A.; Springuel-Huet, M.-A.; Azais, T.; Babonneau, F.; Tourne-Peteilh, C.; Devoisselle, J.-M.; Gedeon, A., Probing the mobility of ibuprofen confined in MCM-41 materials using MAS-PFG NMR and hyperpolarised-129Xe NMR spectroscopy. *Phys. Chem. Chem. Phys.* **2013,** *15* (43), 18805-18808.

30. Brás, A. R.; Noronha, J. P.; Antunes, A. M. M.; Cardoso, M. M.; Schönhals, A.; Affouard, F.; Dionísio, M.; Correia, N. T., Molecular Motions in Amorphous Ibuprofen As Studied by Broadband Dielectric Spectroscopy. *J. Phys. Chem. B* **2008,** *112* (35), 11087-11099.

31. Brás, A. R.; Fonseca, I. M.; Dionísio, M.; Schönhals, A.; Affouard, F.; Correia, N. T., Influence of Nanoscale Confinement on the Molecular Mobility of Ibuprofen. *J. Phys. Chem. C* **2014,** *118* (25), 13857-13868.

32. Zeng, L.; An, L.; Wu, X., Modeling Drug-Carrier Interaction in the Drug Release from Nanocarriers. *J. Drug Delivery* **2011,** *2011*, 370308.

33. Zeng, L.; Wu, X., Modeling the sustained release of lipophilic drugs from liposomes. *Applied Physics Letters* **2010,** *97* (7), 073701.

34. Ugliengo, P.; Sodupe, M.; Musso, F.; Bush, I. J.; Orlando, R.; Dovesi, R., Realistic Models of Hydroxylated Amorphous Silica Surfaces and MCM-41 Mesoporous Material Simulated by Large-scale Periodic B3LYP Calculations. *Adv. Mater.* **2008,** *20* (23), 4579-4583.

35. Coasne, B.; Ugliengo, P., Atomistic Model of Micelle-Templated Mesoporous Silicas: Structural, Morphological, and Adsorption Properties. *Langmuir* **2012,** *28* (30), 11131-11141.

36. Singappuli-Arachchige, D.; Manzano, J. S.; Sherman, L. M.; Slowing, I. I., Polarity Control at Interfaces: Quantifying Pseudo-solvent Effects in Nano-confined Systems. *ChemPhysChem* **2016,** *17* (19), 2982-2986.

37. Kokubo, T.; Kushitani, H.; Sakka, S.; Kitsugi, T.; Yamamuro, T., Solutions able to reproduce in vivo surface-structure changes in bioactive glass-ceramic A-W3. *Journal of Biomedical Materials Research* **1990,** *24* (6), 721-734.

38. Grimme, S.; Antony, J.; Ehrlich, S.; Krieg, H., A consistent and accurate ab initio parametrization of density functional dispersion correction (DFT-D) for the 94 elements H-Pu. *The Journal of Chemical Physics* **2010,** *132* (15), 154104.

39. Schmidt, M. W.; Baldridge, K. K.; Boatz, J. A.; Elbert, S. T.; Gordon, M. S.; Jensen, J. H.; Koseki, S.; Matsunaga, N.; Nguyen, K. A.; Su, S.; Windus, T. L.; Dupuis, M.; Montgomery, J. A., General atomic and molecular electronic structure system. *Journal of Computational Chemistry* **1993,** *14* (11), 1347-1363.

40. Martinez, U.; Pacchioni, G., Interaction of CO, CO2 and CH4 with mesoporous organosilica: Periodic DFT calculations with dispersion corrections. *Microporous Mesoporous Mater.* **2010,** *129* (1), 62-67.

41. Comotti, A.; Bracco, S.; Valsesia, P.; Ferretti, L.; Sozzani, P., 2D Multinuclear NMR, Hyperpolarized Xenon and Gas Storage in Organosilica Nanochannels with Crystalline Order in the Walls. *J. Am. Chem. Soc.* **2007,** *129* (27), 8566-8576.

42. Shoemaker, J. R.; Gordon, M. S., SIMOMM: An Integrated Molecular Orbital/Molecular Mechanics Optimization Scheme for Surfaces. *J. Phys. Chem. A* **1999,** *103* (17), 3245-3251.

43. Mao, K.; Kobayashi, T.; Wiench, J. W.; Chen, H.-T.; Tsai, C.-H.; Lin, V. S. Y.; Pruski, M., Conformations of Silica-Bound (Pentafluorophenyl)propyl Groups Determined by Solid-State NMR Spectroscopy and Theoretical Calculations. *J. Am. Chem. Soc.* **2010,** *132* (35), 12452-12457.

44. Inagaki, S.; Guan, S.; Ohsuna, T.; Terasaki, O., An ordered mesoporous organosilica hybrid material with a crystal-like wall structure. *Nature* **2002,** *416* (6878), 304-307.

45. Zhu, X.; Cho, H.-r.; Pasupong, M.; Regalbuto, J. R., Charge-Enhanced Dry Impregnation: A Simple Way to Improve the Preparation of Supported Metal Catalysts. *ACS Catal.* **2013,** *3* (4), 625-630.

46. Jubert, A.; Legarto, M. L.; Massa, N. E.; Tévez, L. L.; Okulik, N. B., Vibrational and theoretical studies of non-steroidal anti-inflammatory drugs Ibuprofen [2-(4-isobutylphenyl)propionic acid]; Naproxen [6-methoxy-α-methyl-2-naphthalene acetic acid] and Tolmetin acids [1-methyl-5-(4-methylbenzoyl)-1H-pyrrole-2-acetic acid]. *Journal of Molecular Structure* **2006,** *783* (1), 34-51.

47. Gordijo, C. R.; Barbosa, C. A. S.; Da Costa Ferreira, A. M.; Constantino, V. R. L.; Oliveira Silva, D. d., Immobilization of Ibuprofen and Copper-Ibuprofen Drugs on Layered Double Hydroxides. *J. Pharm. Sci.* **2005,** *94* (5), 1135-1148.

48. Kandziolka, M. V.; Kidder, M. K.; Gill, L.; Wu, Z.; Savara, A., Aromatic-hydroxyl interaction of an alpha-aryl ether lignin model-compound on SBA-15, present at pyrolysis temperatures. *Phys. Chem. Chem. Phys.* **2014,** *16* (44), 24188-24193.

49. Zeng, L.; An, L.; Wu, X., Modeling Drug-Carrier Interaction in the Drug Release from Nanocarriers. *Journal of Drug Delivery* **2011,** *2011*, 15.

50. Sinnokrot, M. O.; Valeev, E. F.; Sherrill, C. D., Estimates of the Ab Initio Limit for π–π Interactions: The Benzene Dimer. *J. Am. Chem. Soc.* **2002,** *124* (36), 10887-10893.

CHAPTER 5. CONTROL OF INTERFACIAL pH IN MESOPOROUS SILICA NANOPARTICLES VIA SURFACE FUNCTIONALIZATION

Modified from a manuscript to be submitted to a journal.

Dilini Singappuli-Arachchige[1,2], Igor I. Slowing[1,2]

[1]US DOE Ames Laboratory, Ames, Iowa 50011, United States

[2]Department of Chemistry, Iowa State University, Ames, Iowa 50011, United States

Abstract

The pH at silica-water interfaces (pH_{int}) was measured by grafting a dual emission fluorescent probe (SNARF) onto the surface of mesoporous silica nanoparticles (MSN). The values of pH_{int} of SNARF-MSN suspended in water were different from the pH of the bulk solution (pH_{bulk}) measured with a pH meter. Addition of acid or base to aqueous suspensions of SNARF-MSN induced much larger changes in pH_{bulk} than pH_{int}, indicating that the interface has buffering capacity. Grafting additional organic functional groups onto the surface of SNARF-MSN controls the pH_{int} of its buffering region. The responses of pH_{int} to variations in pH_{bulk} are consistent with the acid/base properties of the surface groups as determined by their pK_a, and are affected by electrostatic interactions between charged interfacial species as evidenced by the dependence of ζ-potential on pH_{bulk}. Finally, as a proof of principle, we demonstrate that the hydrolysis rate of an acid-sensitive acetal can be controlled by adjusting pH_{int} via suitable functionalization of the MSN surface. Our findings can lead to the development of nanoreactors that protect sensitive species from adverse conditions and tune their chemical reactivity.

Introduction

As discussed in previous chapters, the properties of the mesoporous silica-water interface can differ significantly from those of the bulk solvent.[1-3] An additional property of interest is the

acidity or basicity of the interface, because proton transfer processes are involved in a large number of reactions and can affect the stability and behavior of adsorbed chemical species.[4, 5] Several groups have explored the acid-base properties of mesoporous silica-water interfaces using different approaches including electrochemical and conductivity measurements,[6, 7] permeability and adsorption of acids or bases,[8, 9] and spectroscopic methods.[10-13] Importantly, many of these studies have demonstrated that the pH at the silica-water interface is different from that of the bulk.[8, 10-12] This difference suggests the possibility of adjusting the interfacial pH to target values. Attaining such control would enable regulating pH sensitive transformations at interfaces and protecting surface species from unfavorable conditions.

The acid-base properties of silica derive from their weakly acidic silanol groups (Si-OH), which can be either isolated or H-bonded with neighboring silanols. The H-bonded silanols can belong to the same (geminal) or different (vicinal) Si atoms (Scheme 1). Ong et al. used second harmonic generation measurements to probe these groups at the silica-water interface.[14] They observed that at pH > 4 the negatively charged surface produces an electric field that polarizes the interfacial water molecules to give a frequency doubling, and used this property to track deprotonated sites. They reported that a fused silica surface contains two types of silanols with different acidities: ca. 19% with a pK_a 4.5, and 81% with a pK_a 8.5. However, the origin of this bimodal distribution was unclear. Later studies proposed that the lower pK_a corresponded to isolated silanols, and the higher to H-bonded silanols (geminal and vicinal).[15-17]

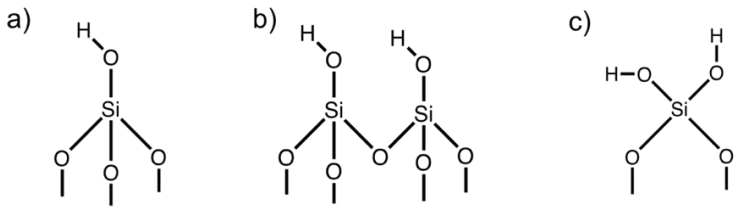

Scheme 1. Different types of silanols on silica surfaces: a) isolated b) vicinal and c) geminal.

Rosenholm et al. studied the adsorption of benzylamine from solution onto non-functionalized and carboxylic acid-modified SBA-15 as a function of pH. The adsorption isotherms were used to calculate apparent pK_a values for surface silanols and carboxylic groups.[8] They identified two types of silanols for non-modified silica ($pK_{a1} < 2$, $pK_{a2} = 8.2$) and an additional pK_a value (4.8) in the modified material, which was assigned to the surface carboxylic groups. Furthermore, they related the effective proton concentration at the pore surface to the bulk proton concentration through the expression:

$$pH_s = pH_b + \frac{2.3\Psi e}{kT} \qquad (1)$$

where Ψ is the surface potential, e is the unit charge, k is the Boltzmann constant and T is the temperature. They suggested that confinement inside the pore leads to an overlap between the electrostatic potential fields of the negative surface charges and inhibits silanol deprotonation. This results in a decreased effective acidity, i.e. a higher apparent pK_a. O'Reilly and co-workers further suggested that protons from the bulk are attracted to the densely charged silica surface thus inducing a difference between interfacial and bulk pH.[18] Teramae and co-workers studied the acid-base equilibria in a mesoporous silica densely functionalized with amine groups using adsorbed fluorescence pH indicators. The fluorescence spectra provided direct information about the molar ratios of neutral, dissociated and protonated forms of the dyes, which in turn gave information about the effective proton concentrations of their environments.[11] Their results showed a non-linear relationship between the interfacial and bulk pH values, in which large variations of the solution pH induced only small changes in the interfacial pH. Olsson and co-workers designed another method to measure pH inside the pores of SBA-15 type mesoporous silica by immobilizing a fluorescently labeled acid-sensitive protein on the material. They

showed that the pH inside the pores remained close to 7 while they varied the solution pH in the range 6-8, concluding that the pores had a buffering capacity.[12]

All these studies indicate that the pH in the vicinity of the silica surface is different from the bulk and suggest that controlling the surface chemistry of this material could be a powerful tool for adjusting the interfacial pH to desired values. Herein we demonstrate that the interfacial pH of mesoporous silica nanoparticles (MSN) can be fine-tuned by binding acidic or basic groups to its surface. We used the pH sensitive ratiometric response of the fluorescent probe Carboxy-SNARF (2-(10-(dimethylamino)-3-oxo-3H-benzo[c]xanthen-7-yl)-1,5-benzenedicarboxylic acid) to assign pH values to acid- or base-grafted mesoporous silica-water interfaces. We found that the interfacial pH is different from the pH of the bulk solution and is controlled by the pK_a of the grafted species and the ionic strength of the solution. We then show that an acetal grafted on the silica surface can be protected from an acidic environment by controlling the interfacial pH of the material.

Materials and Methods

Materials

Hexadecyltrimethylammonium bromide (CTAB), methanol, N-(3-dimethylaminopropyl)-N'-ethylcarbodiimidehydrochloride, N-hydroxysuccinimide sodium salt, 1,4-dioxane, benzyl magnesium chloride and hexane were purchased from Sigma-Aldrich and tetramethylorthosilicate (TMOS) from Aldrich. Tetraethylorthosilicate (TEOS), 3-aminopropyl trimethoxysilane, N'-[3-(trimethoxysilyl)propyl]ethylenediamine, N'-[3-(trimethoxysilyl)propyl]diethylenetriamine, and 3-(trimethoxysilyl)propylsuccinic anhydride were purchased from Gelest, Inc. NaOH, NaCl, concentrated HCl, methylene chloride, ethylacetate and acetone were purchased from Fisher Scientific. 5-(and-6)-Carboxy SNARF-1 was purchased from Invitrogen by Thermo Fisher Scientific. Pluronic P104 was supplied from

BASF chemical company. Tetrakis(trimethylsilyl)silane (TTMS) was from Aldrich and benzene-*d*6 from Cambridge Isotope Laboratories. All reagents were used as received without further purification.

Characterization

A Rigaku-Ultima 4 X–ray diffractometer equipped with Cu Kα radiation (40 kV, 44 mA) was used to record XRD patterns over the range of 1–5 2θ degrees. A Micromeritics Tristar surface area and porosity analyzer was used to measure nitrogen sorption isotherms. The surface areas and pore size distributions were calculated using the Brunauer-Emmett-Teller (BET) and Barrett-Joyner-Halenda (BJH) methods respectively. Elemental analyses of different MSN samples were done by triplicate on a Perkin Elmer 2100 series II CHNS analyzer, using acetanilide as calibration standard and combustion and reduction temperatures of 925 °C and 640 °C respectively. Diffuse Reflectance Infrared Fourier Transform (DRIFT) measurements were done using a Bruker Vertex 80 FT-IR spectrometer equipped with a HeNe laser and photovoltaic MCT detector and OPUS software. Solution phase ^{1}H NMR spectra were collected on Bruker Avance III 600 spectrometer, using TTMS as the standard. Fluorescence spectra were acquired on a Cary Eclipse fluorescence spectrophotometer. Excitation wavelength was set at 488 nm, both excitation and emission slit widths were set at 5 nm. Positive ion mode mass spectra (MS) were obtained using an Agilent QTOF 6540 mass spectrometer. The instrument was operated in the 4 GHz HRes mode. Accurate mass measurements were achieved by constantly infusing a calibrant (masses 121.0508 and 922.0098).

Synthesis of MCM-41 type Mesoporous Silica Nanoparticles (MSN)

CTAB (1.0 g, 2.74 mmol) was dissolved in deionized water (480 mL) in a round bottom flask followed by addition of 2M NaOH (3.5 mL, 7.0 mmol). The solution was continuously stirred for one hour at 80 °C. Tetraethylorthosilicate (TEOS, 5.0 mL, 22.6 mmol) was then added

dropwise over 5 min to the CTAB solution. Magnetic stirring was continued for additional 2 h at 80 °C. The solution was filtered, washed with abundant water and methanol. CTAB template was removed by calcination of dry solid at 550 °C for 6 h with a rate of 2 °C/min. The material was characterized by nitrogen physisorption isotherms and XRD patterns (Figure S1).

Synthesis of SBA-15 type MSN (MSN-10)

Pluronic P104 (7.0 g) was mixed with 4 M HCl (109 mL, 0.44 mol) and deionized water (164 mL). After stirring for 1 h at 55 °C, tetramethylorthosilicate (TMOS, 10.6 mL, 0.072 mol) was added and stirred for an additional 24 h. The resulting mixture was subjected to a hydrothermal treatment for 24 h at 150 °C in a high-pressure reactor. Upon cooling to room temperature, the white solid was collected by filtration, washed with abundant methanol and air dried. The surfactant pluronic P104 was removed by calcination at 550 °C for 6 h with a rate of 2 °C/min. This material was termed MSN-10. The material was characterized by nitrogen physisorption isotherms and XRD patterns (Figure S1).

Synthesis of functionalized SNARF-MSN/MSN-10

5-(and-6)-Carboxy SNARF-1 (1 mg, 2.2 μmol) was added to excess N,N'-dicyclohexylcarbodiimide (3 mg, 15 μmol) in methylene chloride (0.5 mL) followed by N-hydroxysuccinimide (3 mg, 26 μmol). The reagents were stirred at 25 °C for 24 h. Aminopropyltrimethoxysilane in acetone (30 mM, 0.100 mL) was added to the mixture and continued stirring at 25 °C for another 24 h. The solvent was removed under reduced pressure, resultant SNARF-AP-TMS was redissolved in acetone, an aliquot of the solution (1.1 mM, 1.0 mL) was added to pre-calcined MSN or MSN-10 (1.0 g) and ground until seemingly dry. The material was then heated in a microwave reactor at 100 °C for 30 min, washed with water until supernatant showed no fluorescence and vacuum dried overnight. The resultant materials were termed SNARF-MSN and SNARF-MSN-10 respectively. SNARF-MSN was then impregnated

with different organosilanes via incipient wetness. Organosilanes dissolved in acetone (1M, 0.100 mL) were added to SNARF-MSN (0.100 g) separately and ground until seemingly dry. The material was then heated in a microwave reactor at 100 °C for 30 min, washed with water and vacuum dried overnight. The target loadings were 1 mmol/g for all materials, except for SA/DAP-SNARF-MSN that had 0.5 mmol/g target loading for each group. The materials were washed with water and vacuum dried overnight. The materials were characterized by DRIFT spectroscopy and elemental analysis.

Synthesis of SNARF-AP

5-(and-6)-Carboxy SNARF-1 (0.25 mg, 0.55 μmol) was added to excess N,N'-dicyclohexylcarbodiimide (0.75 mg, 3.75 μmol) in methylene chloride (0.125 mL) followed by N-hydroxysuccinimide (0.75 mg, 6.5 μmol). The reagents were stirred at 25 °C for 24 h. Propylamine in acetone (75 mM, 0.010 mL) was added to the mixture and continued stirring at 25 °C for another 24 h. The resultant SNARF-AP was separated via thin layer chromatography using ethylacetate:hexane (3:1) as the mobile phase. The silica layer was scratched, and SNARF-AP was extracted to ethanol. The solvent was removed under reduced pressure. The product was characterized by DRIFT spectroscopy and mass spectrometry.

Titrations of functionalized SNARF-MSN/MSN-10 and SNARF-AP

Functionalized SNARF-MSN materials and SNARF-MSN-10 were suspended in water (5 mg/mL, 5.0 mL) and titrated with aqueous HCl (5 mM) and aqueous NaOH (5 mM) separately. At each addition of acid/base, the pH of solution was measured using a pH meter and fluorescence spectra of the suspension was recorded using Cary Eclipse fluorescence spectrophotometer. SNARF-AP (0.3 mg) was added to aqueous NaOH (5 mM) and titrated against aqueous HCl (5 mM). At each addition of acid/base, the pH of solution was measured using a bench-top pH meter and fluorescence spectra of the suspension was recorded using Cary

Eclipse fluorescence spectrophotometer. The fluorescence intensity ratio (588 nm/635 nm) was plotted against the measured solution pH.

Silanol quantification of MSN, MSN-10

The MSN materials were treated at 100 °C under vacuum in a Schlenk line overnight to remove any physisorbed water. Dibenzyl magnesium dioxane was prepared as reported.[19] All MSN materials (10.0 mg) were mixed with excess dibenzyl magnesium dioxane (100 mg) under N_2 atmosphere, followed by addition of TTMS in C_6D_6 (0.01 M, 0.6 mL). After 20 h, the amount of released toluene was quantified via ^{1}H NMR.

Synthesis of functionalized MSN-PNB

A solution of 5,6-epoxyhexyltriethoxysilane in ethanol (0.5 mL, 0.4 M) was added to pre-calcined MSN (500 mg) and ground until seemingly dry. The material was then heated in a microwave reactor at 100 °C for 2 h, washed with water and vacuum dried. The resultant material was suspended in water (10 mL) followed by addition of H_2SO_4 (0.5 mL, 0.1 M). The mixture was heated at 85 °C for 3 h, washed with water and vacuum dried. The resultant product was re-suspended in ethanol (30 mL), followed by addition of *p*-nitrobenzaldehyde (0.40 mmol, 60 mg) and H_2SO_4 (0.5 mL, 0.1 M). The mixture was then heated at 85 °C for 5 h, washed with ethanol and vacuum dried. The resultant MSN-PNB was characterized by DRIFT-IR and elemental analysis. The PNB acetal loading in the material was 0.02 mmol/g.

MSN-PNB was then impregnated with 3-(trimethoxysilyl)propylsuccinic anhydride and N'-[3 (trimethoxysilyl)propyl]diethylenetriamine via incipient wetness: the organosilanes dissolved in anhydrous ethanol (1M, 0.070 mL) were added to MSN-PNB (0.070 g) separately and ground until seemingly dry. The material was then heated in a microwave reactor at 100 °C for 30 min, washed with ethanol and vacuum dried overnight. All the materials were characterized by elemental analysis and DRIFT spectroscopy. Both propyl-succinic anhydride

and diethylenetriamine loadings were 0.7 mmol/g each as determined by elemental (C,H,N) analysis.

Hydrolysis of PNB acetal

Functionalized MSN-PNB samples (25.0 mg each) were introduced into a dialysis membrane (Spectrum Labs, MW cutoff = 12-14 kDa) and immersed into an aqueous HCl solution of pH 5 (10.0 mL). The intact aqueous solution was continuously circulated through a quartz flow cuvette, and the absorption band at 274 nm was monitored for 7 h via UV-vis spectroscopy, taking scans every 5 min. Three separate release experiments were performed for each material, and the results were averaged. The data were fitted to a first order model.

Results and Discussion

Synthesis of functionalized SNARF-MSN and SNARF-AP

Carboxy-SNARF-1 (C-SNARF-1) is one of the most widely used dual emission pH responsive fluorescent probes in the family of Seminapthorhodafluors (SNARFs).[12, 20] We first reacted C-SNARF-1 (2.2 μmol) with 3-aminopropyltrimethoxysilane (AP-TMS, 3 μmol) via dicyclohexylcarbodiimide /N-hydroxysuccinimide (DCC/NHS) coupling (25 °C, 24 h). The resultant SNARF-AP-TMS was grafted onto pre-calcined mesoporous silica nanoparticles (MSN). The material was termed SNARF-MSN. Then, we produced a set of surface-functionalized materials by grafting organosilanes with groups of different pK_a values onto SNARF-MSN (Scheme 2, Table S1).

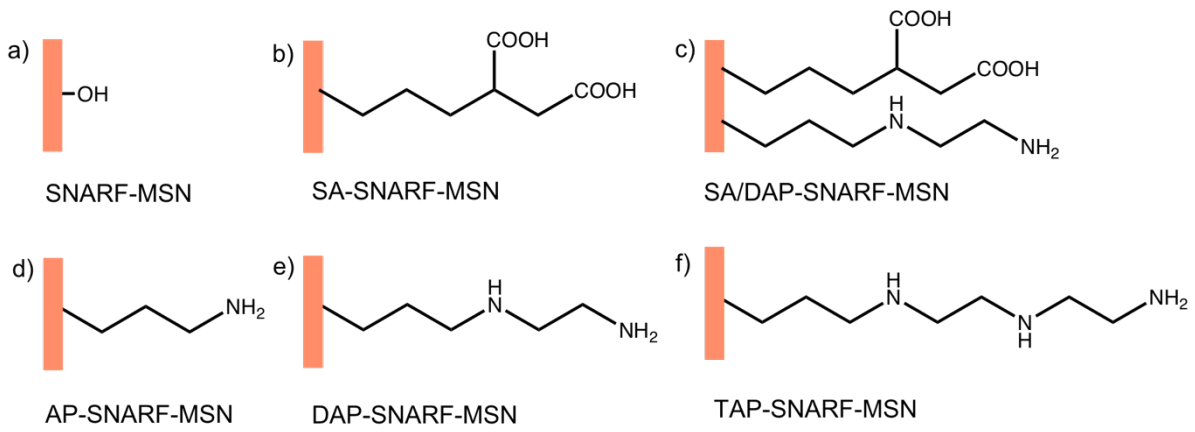

Scheme 2. Structures of the functional groups added to the surface of SNARF-MSN.

Successful grafting of the groups was verified by DRIFT spectroscopy and elemental analysis (Table S1, Figures S2). Characteristic features in the IR spectra include C-H stretching bands in the range 2850-2950 cm^{-1} and C-H bending modes in the range 1440-1560 cm^{-1} for all samples, vibration bands attributed to C-N stretching at 1365 cm^{-1} for AP-SNARF-MSN, DAP-SNARF-MSN, TAP-SNARF-MSN and SA/DAP-SNARF-MSN, C=O stretching at 1725 cm^{-1} and C-O stretching at 1380 cm^{-1} for both SA-SNARF-MSN and SA/DAP-SNARF-MSN. Elemental analysis revealed the group loadings for functionalized SNARF-MSN were in the range 0.7-0.8 mmol/g for all samples and the bifunctional SA/DAP-SNARF-MSN had 0.4 mmol/g and 0.3 mmol/g loading for each group respectively.

We also coupled C-SNARF-1 with propyl amine via DCC/NHS reaction (25 °C, 24 h) to produce SNARF-AP, and used it to build a calibration plot of fluorescence intensity ratios (I_{588}/I_{635}) versus solution pH. This compound was characterized by FTIR (Figure S3). C-SNARF-1 and SNARF-AP both showed characteristic IR bands for OH stretch (3100-3700 cm^{-1}), C-H stretch (2850-3000 cm^{-1}), aromatic C=C stretch (1300-1500 cm^{-1}), C-O stretch (1074 cm^{-1}) and =C-H bend (735-870 cm^{-1}). C-SNARF-1 showed a broad band centered around 1640 cm^{-1}, which likely corresponds to the overlapping bands of the C=O stretches of the two carboxylic

groups. SNARF-AP showed characteristic amide bands (absent in C-SNARF) that include amide I band corresponding to amide C=O stretch (1697 cm^{-1}), amide II band corresponding to N-H bend (1617 cm^{-1}), amide III band corresponding to C-N stretch and N-H in plane deformation (1207 cm^{-1}) and amide IV band corresponding to in plane amide C=O bend and C-C stretch (764 cm^{-1}).[21] In addition, mass spectra showed the parent peak of SNARF at m/z=454 $[M-H]^+$ and AP-SNARF at m/z= 495 $[M-H]^+$ (Figure S4). These results confirmed that the AP modification of C-SNARF was successful.

Calibration curve for pH_{int}

The protonated and deprotonated forms of the SNARF-AP showed two fluorescence emission maxima (588 nm and 635 nm, respectively) when excited at 488 nm (Figure 1a). Thus, the ratio of the fluorescence intensities at these wavelengths (I_{588}/I_{635}) provides a measure of the pH of the probe's environment.[12] To construct a calibration plot, we titrated an aqueous solution of SNARF-AP in NaOH (5 mM, 5 mL) with aqueous HCl (5 mM). The fluorescence spectra and the pH of the solution (measured with a pH meter) were collected following each addition of the titrant (Figure 1b). The sigmoidal plot showed a decrease in intensity ratio (I_{588}/I_{635}) with increasing pH, which is consistent with previous reports of free and bound SNARF.[20] The linear range of the plot is limited to fluorescence intensity ratios between 0.2 and 2.0, corresponding to solution pH values of 9.3 to 6.5 respectively (Figures 1b, S5). The regression equation of the linear plot was used to calculate the pH at the interface of aqueous suspensions of SNARF-modified MSN. Hereafter, the pH of the bulk solution is termed pH_{bulk} and the pH at the silica-water interface is termed $pH_{int.}$

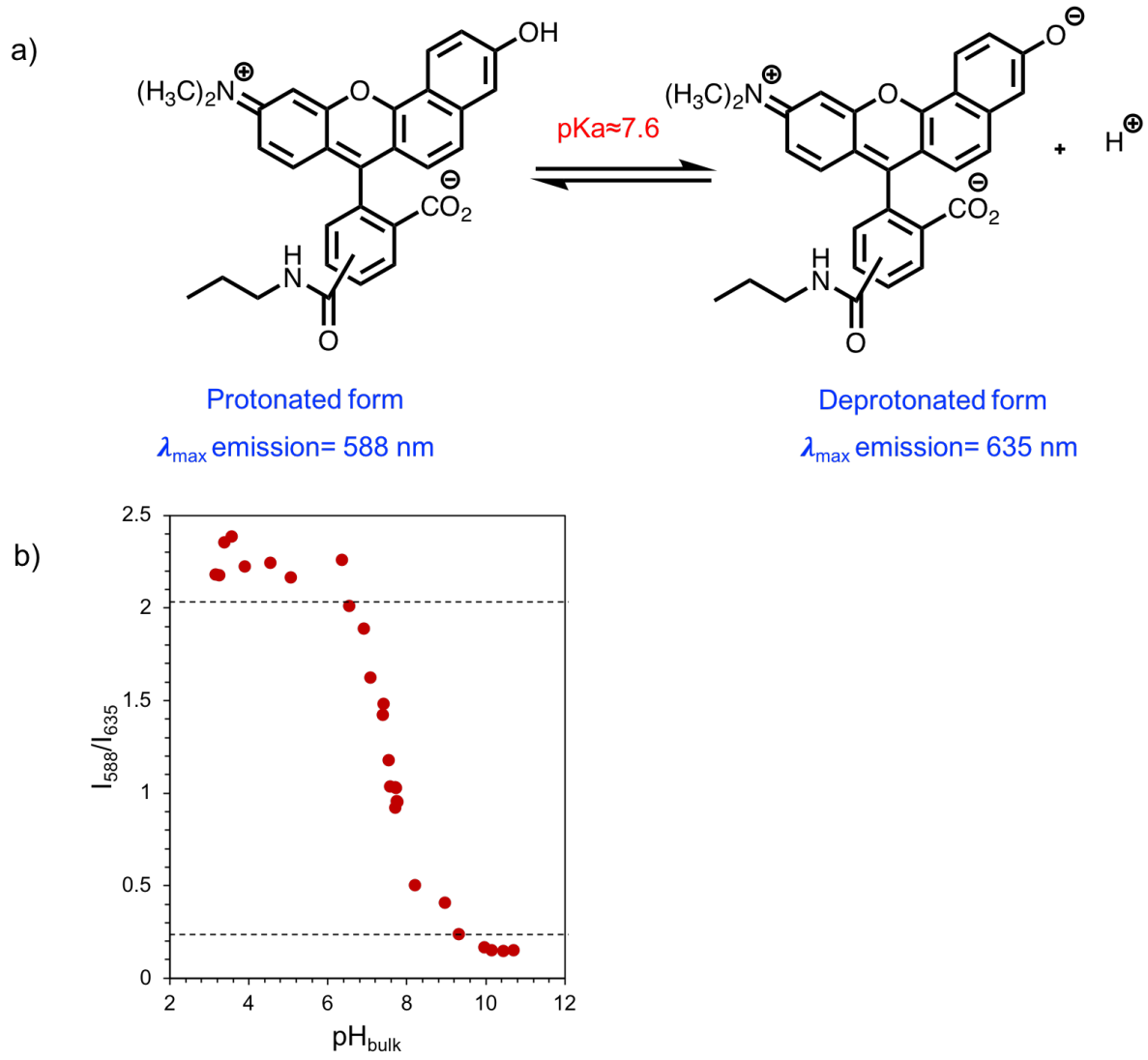

Figure 1. a) Protonated and deprotonated states of SNARF-AP.12 b) Titration curve of SNARF-AP displaying the change of I588/I635 as a function of pHbulk.

Acid-Base titrations of non-functionalized and functionalized SNARF-MSN materials

The aqueous suspensions of functionalized-SNARF-MSN materials (5.0 mg/mL) were titrated with HCl (5.0 mM) or NaOH (5.0 mM) solutions. Each titrant addition was followed by pH_{bulk} measurement (using a pH meter) and recording of the fluorescence spectrum (Figure S6). The I_{588}/I_{635} decreased with increasing pH_{bulk} for all of the samples (Figure S7). Data analysis was restricted to fluorescence intensity ratios in the linear region of the SNARF-AP calibration (I_{588}/I_{635} = 2.0 – 0.2), corresponding to interfacial pH (pH_{int}) values in the range 6.5 to 9.3 (Figure

S5). Consistent with previous reports all pH_{int} were different from pH_{bulk}.[11] Interestingly, the relationship between both pH values was not linear and varied with the nature of the functional groups in the materials (Figure 2a). Two regions can be identified in Figure 2a for all of the samples: one at low pH_{bulk} where the interface is less acidic than the bulk ($pH_{int} > pH_{bulk}$), and one at high pH_{bulk} where the interface is less basic than the bulk ($pH_{int} < pH_{bulk}$). Importantly, variations in pH_{int} were significantly smaller than those in pH_{bulk}: for a bulk pH change of 6 units the pH_{int} change was only ca. 1.5 units for all the functionalized SNARF-MSN materials. This suggests that all the interfaces were buffered. Furthermore, the buffering effect varied with the type of functionality in the materials.

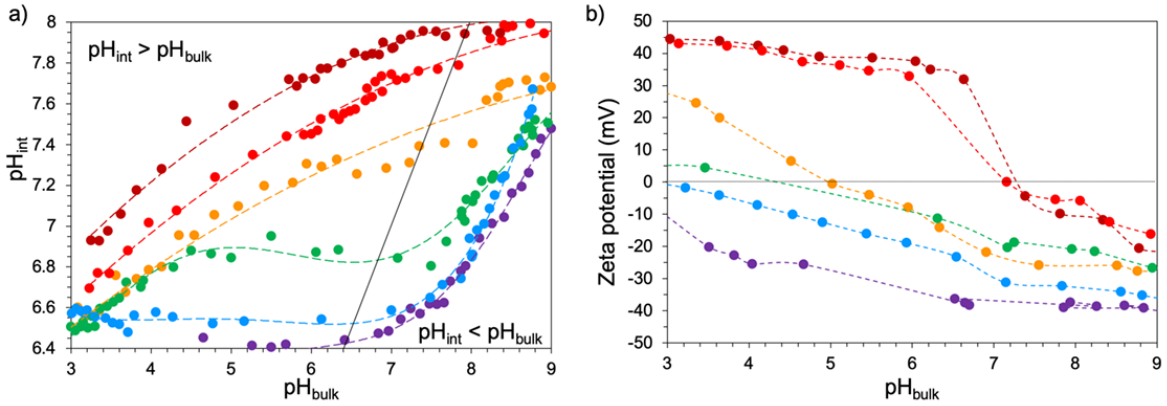

Figure 2. a) Variation of a) pH_{int} and b) ζ-potential with pH_{bulk} for functionalized SNARF-MSN. The diagonal in a) corresponds to values where $pH_{int} = pH_{bulk}$. Discontinuous lines in a) are only visual aids. TAP-SNARF-MSN (burgundy), DAP-SNARF-MSN (red), AP-SNARF-MSN (orange), SA/DAP-SNARF-MSN (green), SNARF-MSN (blue), SA-SNARF-MSN (purple).

In general, for any given pH_{bulk} value pH_{int} increased in the order SA-SNARF-MSN $\lesssim$ SNARF-MSN < SA/DAP-SNARF-MSN < AP-SNARF-MSN < DAP-SNARF-MSN < TAP-SNARF-MSN (Table S1). This trend corresponds with the type of functional acid/base groups in the material: while SA groups increased the acidity of the interface, amine groups made it more basic. pH_{int} also increased with the number of amine groups in the organic chain (AP < DAP <

TAP). A combination of SA and DAP groups gave pH_{int} values in between those of the acid and base functionalized materials. Notably, the shapes of the pH_{bulk} versus pH_{int} curves are different for acidic than for basic groups. The shapes of these curves indicate that: 1) pH_{int} of the materials with acidic surfaces (SA-SNARF-MSN and SNARF-MSN) has little variation in the acid pH_{bulk} region (pH_{bulk} 3 – 7, i.e. a buffer behavior), but a sharper response to pH_{bulk} in the basic region (pH_{bulk} >7); and 2) pH_{int} of the materials with basic groups (AP-, DAP- and TAP-SNARF-MSN) display larger variation in the acidic pH_{bulk} regime, that tends to plateau in the basic pH_{bulk} region. Interestingly, SA/DAP-SNARF-MSN having both acidic and basic groups showed a more complex behavior, with steeper pH_{int} changes in the acid and basic regions (pH_{bulk} < 4.5 and >7.5 respectively), and a buffering zone of nearly constant pH_{int} in between. These results may be understood by considering the acid-base equilibria of the surface groups (Figure S8) and the effect of surface charge on the activity of ions at the interface according to the Debye-Hückel theory.

Interfacial acid-base equilibria of functionalized SNARF-MSN

Because SNARF loading is too small (1 μmol/g) compared to the number of silanols and functional groups in the materials (ca. 3.0 and 0.8 mmol/g respectively) the contribution of SNARF protonation/deprotonation equilibrium to pH_{int} can be neglected. Therefore, the only relevant acid-base equilibria in the materials are the protonation/deprotonation of silanols and surface organic groups.

When titrating the silanols in SNARF-MSN from low to high pH, the surface charge of the material becomes increasingly negative due to silanoxy ion formation. The development of anionic groups on the surface is evidenced by the continuous drop in the ζ-potential of the material (from 0 to -35 mV) when pH_{bulk} is varied from 2 to 9 (Figure 2b). The silanol loading in MSN, measured by reaction with benzylmagnesium bromide, is 3.0 mmol/g, corresponding to a

surface density of 1.9 groups/nm^2 (surface area of SNARF-MSN: 941 m^2/g). This result is at the lower end of typical values reported in the literature (1.7 to 4 groups/nm^2),[22] variations in silanol densities are related to synthetic method and sample history. This density corresponds to average inter-silanol distances of ca. 0.8 nm, which are much smaller than the Debye radius for aqueous solutions of electrolytes at the titrant concentration (4.3 nm at 5 mM).[23] Thus, the proximity between silanol groups inhibits their dissociation due to the strong coulombic repulsion between the resulting silanoxy anions (Figure 3a). This shift in equilibrium implies a lower H^+ activity at the interface compared to the bulk and explains the $pH_{int} > pH_{bulk}$ observed in the acidic region of the titration curve (pH_{bulk} 3 – 7). In contrast, in the basic region $pH_{int} < pH_{bulk}$, with both pH increasing at comparable rates (although pH_{int} is lagged). The different behavior of pH_{int} in the basic region is attributed to dissociation of the more weakly acidic H-bonded silanols (pK_a 8.5) along with silanoxy anion stabilization via charge screening by Na^+ counterions from the titrant (Figure 3b). According to the Gouy-Chapman-Stern theory, the difference in potential between the charged surface and the bulk liquid induces migration of ions towards the SNARF-MSN particles to form an electric double layer, thereby establishing a higher cation concentration at the interface than the bulk.[18, 24] A similar behavior is observed for SA-SNARF-MSN. However, because of its lower pK_a (4.2 versus 4.5 for isolated silanols) the buffered region appears at a slightly lower pH.

The effect of basic groups on the pH_{int} of functionalized SNARF-MSN is much more dramatic than that of the succinic acid groups. In the acidic region (pH_{bulk} <7) amine groups in AP-, DAP- and TAP-SNARF-MSN act as proton scavengers and become alkylammonium cations as evidenced by the positive ζ-potentials of the materials (Figure 2b). The densely charged surface is stabilized by ion pair formation with silanoxy groups and screening by

chloride counterions from the titrant (Figure 4a). Thus, the free [H^+] is lower at this interface than at the solvent-silica interface of SNARF-MSN or SA-SNARF-MSN, and the bulk solution ($pH_{int\ AP\text{-}SNARF\text{-}MSN} > pH_{int\ SNARF\text{-}MSN} > pH_{bulk}$). Rising the pH_{bulk} leads to a decrease in ζ-potentials to reach neutrality at pH_{bulk} 5, 7.1 and 7.3 for AP-, DAP- and TAP-SNARF-MSN, respectively. These points of zero charge (PZC) vary as a function of the number of N atoms in the organic groups (AP << DAP < TAP) and the pK_a of the corresponding alkylammonium ions. For these materials the drop in ζ-potential is a combination of alkylammonium and silanol deprotonation corresponding to loss of positive and gain of negative surface charges, respectively. It is noteworthy that the first ammonium group in TAP is as acidic as the isolated silanols (pK_a 4.5).[25] At the PZC the number of protonated alkylammonium groups matches the number of deprotonated silanoxy groups on the functionalized SNARF-MSN surfaces. The rate of increase in pH_{int} for these materials is lower than pH_{bulk}, and drops steadily suggesting that a plateau may be reached at $pH_{bulk} > 8$. The decreasing pH_{int} sensitivity to the addition of base titrant suggests that the incoming OH^- are neutralized by H^+ from alkylammonium surface groups, while Na^+ take over as counterions for silanoxy stabilization (Figure 4b). The combination of silanoxy stabilization and alkylammonium deprotonation also results in increasingly negative ζ-potentials.

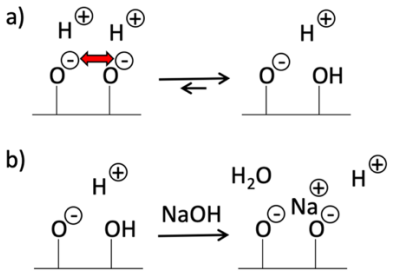

Figure 3. a) Inhibition of silanol dissociation at low pH due to charge repulsion, and b) enhancement of silanol dissociation at high pH (reaction with NaOH) due to charge screening by Na+ counterions.

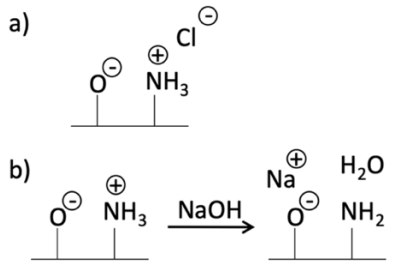

Figure 4. a) Amine protonation decreases the effective [H+] in the acidic region of the titration curve, the resulting ammonium ions are stabilized by silanoxy or Cl- counterions. b) Added base has little effect on pHint because it is neutralized via deprotonation of the surface ammonium ions.

The dependence of pH_{int} of SA/DAP-SNARF-MSN on pH_{bulk} appears as a combination of those of the individual SA- and DAP-SNARF-MSN materials. The behavior in the low pH region ($pH_{bulk} < 4.5$) is dominated by the basic component (DAP) with a small excess of protonated alkylammonium groups indicated by the slightly positive ζ-potential. In this first regime pH_{int} is higher than pH_{bulk} likely due to stabilization of protonated alkylammonium by carboxy, silanoxy and chloride counterions. Furthermore, the rate of pH_{int} increase with pH_{bulk} is the same as that of the amine functionalized SNARF-MSN materials. Upon reaching the PZC (pH_{bulk} ~4.5) the pH_{int} becomes invariant at ca. 6.9 over a range of 3 pH_{bulk} units (4.5 – 7.5). In this regime, the interface behaves like a traditional buffer due to coexistence of acidic (carboxylic, silanol) and basic (amine) groups with pK_a spanning from 4.2 to 7.5. At higher pH, the behavior resembles that of acidic MSN materials, with a sharp increase in pH_{int} trailing pH_{bulk} by about one unit, and the silanoxy and carboxy surface charges stabilized via screening by Na^+ counterions from the titrant.

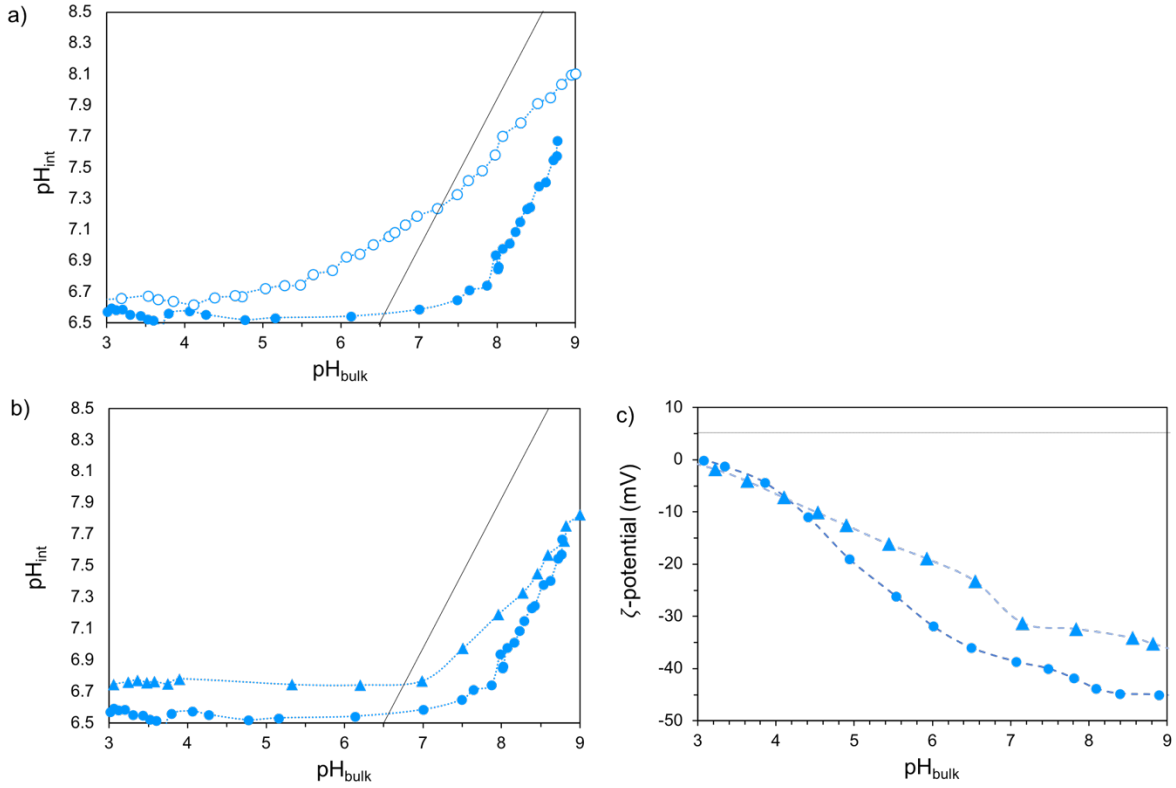

Figure 5. a) Effect of ionic strength on the dependence of pH_{int} on pH_{bulk} for SNARF-MSN. Titration of the material in water (filled circles) and 1M NaCl solution (empty circles). Variation of b) pH_{int} and c) ζ-potential with pH_{bulk} for SNARF-MSN (blue circles) and SNARF-MSN-10 (blue tringles).

The above discussion suggests that coulombic interactions at the MSN surface play a critical role in regulating pH_{int}. Indeed, increasing the ionic strength of the solution by adding NaCl (1M) to the solvent results in even larger differences between pH_{int} and pH_{bulk} for SNARF-MSN over all the titration range (Figure 5a, S9). The higher ionic strength leads to lower H^+ activities at the interface (i.e. higher pH_{int}) consistent with the Debye-Hückel theory. Importantly, increasing the ionic strength of the solution decreases the material's capacity to resist pH_{int} changes in the 4.5 – 7 pH_{bulk} regime. However, the change in pH_{int} (ca. 0.5 units) is still much smaller than that of the bulk.

Increasing the pore width from 2.5 nm (SNARF-MSN) to 7.1 nm (SNARF-MSN-10) results in larger differences between pH_{int} and pH_{bulk} (Figure 5b, S9). For pH region (3-7), there is an upward shift of the SNARF-MSN-10 curve compared to SNARF-MSN. The differences in pH_{int} between both materials should be a combination of their different silanol densities (SNARF-MSN 1.9 groups/nm^2 and SNARF-MSN-10 3.2 groups/nm^2), and the differences in space available for double layer formation.[10] For $pH_{bulk} > 7$, pH_{int} increased for both suggesting that the increasing number of negative charges on the surface are effectively shielded by the counter ions. This is supported by the changes in ζ-potential of the material as a function of pH_{bulk} (Figure 5c). The drop in ζ-potential is steeper for SNARF-MSN compared to SNARF-MSN-10.

Hydrolysis of PNB-acetal

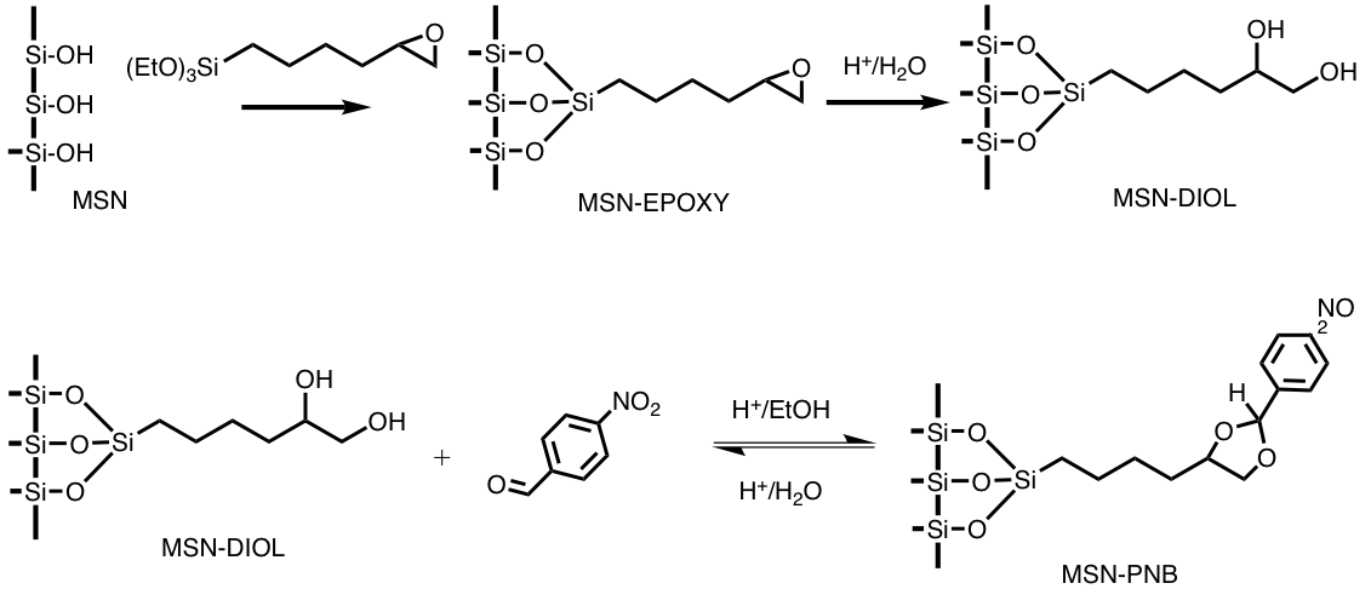

Scheme 2. Synthesis of MSN-PNB.

To evaluate the buffering activity of the functionalized MSN-water interfaces we examined their capacity for inhibiting the hydrolysis of an acetal in aqueous HCl. We synthesized a parent material with *p*-nitrobenzaldehyde moiety bound to a surface organic group

via an acetal linkage (MSN-PNB, Scheme 2). The material was then further grafted with acidic and basic silanes to produce the corresponding SA-MSN-PNB and TAP-MSN-PNB. All materials were characterized by DRIFT spectroscopy (Figure S10). All the materials showed the characteristic NO_2 stretching signals (1525 cm^{-1} and 1350 cm^{-1}) confirming the incorporation of the target molecule. Importantly, the carbonyl stretch (1700 cm^{-1}) of *p*-nitrobenzaldehyde was absent in all synthesized materials. In contrast, a control sample prepared by physically adsorbing *p*-nitrobenzaldehyde on MSN showed characteristic IR bands for C=O stretch (1700 cm^{-1}) along with the two NO_2 stretching signals (1525 cm^{-1} and 1350 cm^{-1}) (Figure S10). These observations suggested the successful formation of the acetal linkage. Elemental analysis indicated the *p*-nitrobenzaldehyde loading in the parent MSN-PNB sample was 0.02 mmol/g.

The MSN-PNB samples (25.0 mg each) were then immersed in an aqueous solution with pH_{bulk} adjusted to 5 (10.0 mL) at 25 °C to induce the hydrolysis of the acetal. The production of *p*-nitrobenzaldehyde was tracked by measuring the absorbance at 274 nm (Figure 6). In spite of having the same pH_{bulk} the rates of *p*-nitrobenzaldehyde production varied between the different MSN-PNB materials. Because the rate of acetal hydrolysis decreases with increasing pH,[26] this result suggests that the pH in the immediate environment of the immobilized acetal (i.e. pH_{int}) is different for each material. Indeed, the rates of hydrolysis decreased in the order SA-MSN-PNB > MSN-PNB > TAP-MSN-PNB, which correspond to increasing pH_{int} of the materials (for pH_{bulk} = 5, the corresponding pH_{int} are <6.5, 6.5 and 7.5 respectively, Figure 2), confirming that the pH of the local environment was effectively regulated by the surface chemistry of the materials.

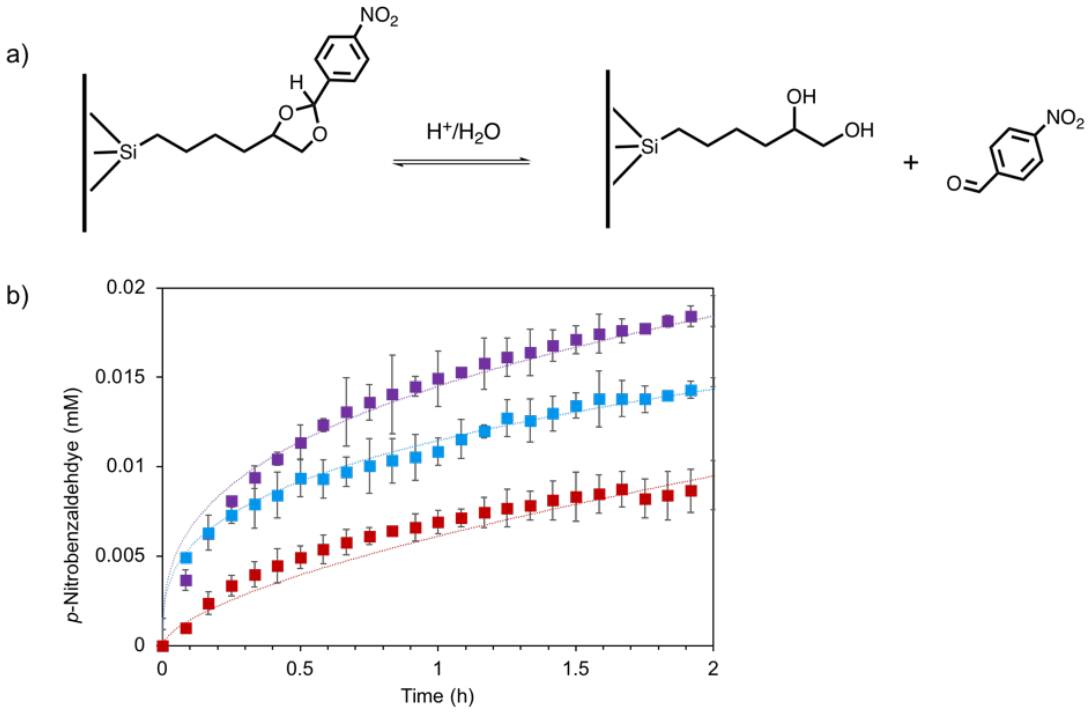

Figure 6. a) Hydrolysis of p-nitrobenzaldehyde acetal from the materials under acidic conditions. b) p-Nitrobenzaldehyde produced from SA-MSN-PNB (purple), MSN-PNB (blue), and TAP-SNARF-MSN (burgundy) vs time. Dotted lines are only visual aids.

Conclusions

We tuned the pH_{int} at mesoporous silica-water interface by grafting acid/base functional groups with different pK_a values on MSN pore surfaces. We quantified the pH_{int} inside these functionalized MSN pores via aminopropyl modified pH sensitive fluorescence probe attached on the silica surface. A calibration curve was constructed using fluorescence intensity ratio (I_{588}/I_{635}) of the probe at different pH_{bulk}. The trendline for the linear potion of the graph was used to assign pH_{int} values for functionalized silica pores.

We observed two different regions for pH_{int} versus pH_{bulk} plot for different functionalized MSN samples, i.e. $pH_{int} > pH_{bulk}$ and $pH_{int} < pH_{bulk}$. The proximity of silanol groups on MSN

surface inhibit their acid dissociation due to strong coulombic repulsion forces. Therefore, for acidic MSN (SA-SNARF-MSN and SNARF-MSN), $pH_{int} > pH_{bulk}$ in the acidic region of the titration curve. In the basic region, silanoxy anions can be stabilized via Na^+ counterions during the titration and $pH_{int} < pH_{bulk.}$ This was evident by the ζ-potential dropping to more negative values with increasing pH_{bulk}. For basic AP-, DAP- and TAP-SNARF-MSN samples, amine groups can take up H^+ ions and form ammonium-silanoxy ion pairs on surface. The positive charges can further be screened via chloride ions during titration in the acidic region. Therefore, the pH_{int} was even higher than the acidic MSN samples. Increasing pH_{bulk} led to deprotonation of alkylammonium and silanol groups, evidenced by positive ζ-potential values dropping to negative values. The acid/base bifunctional SA/DAP-SNARF-MSN behaved as a combination of individual SA- and DAP-SNARF-MSN materials. In addition, we demonstrated that increasing the ionic strength of the solution or increasing the pore width resulted in a lower H^+ activity at the interface.

We evaluated the buffering property of the functionalized MSN materials via their capacity to inhibit the hydrolysis of a surface bound acetal. We showed that by increasing pH_{int} within silica pores, we could reduce the hydrolysis of acetal regardless that the bulk medium is acidic. Being able to tune and control the interfacial pH can lead to potential applications of these materials as nanoreactors with the ability to protect chemical species and enzymes in harsh conditions.

Acknowledgements

This research is supported by the U.S. Department of Energy, Office of Basic Energy Sciences, Division of Chemical Sciences, Geosciences, and Biosciences, through the Ames Laboratory Catalysis Science program. The Ames Laboratory is operated for the U.S. Department of Energy by Iowa State University under Contract No. DE-AC02-07CH11358.

Supplemental Tables and Figures

Table S1. Properties of surface functional groups.

Group	pK_a[a]	pH_{int} at $pH_{bulk}=7$[b]	Point of Zero Charge[c]	Group loading[d] (mmol/g)
SA	4.2, 5.6	6.5	2.5	0.7
None (-SiOH)	4.5	6.6	3	-
SA:DAP		6.8	4.5	0.4:0.3
Amine (AP)	10.5	7.3	6	0.8
Ehtylenediamine (DAP)	7.5, 10.3	7.7	7.2	0.8
Diethylenetriamine (TAP)	4.4, 9.2, 10.0	7.9	7.4	0.7

a pKa values from CRC handbook of chemistry and physics. Haynes, W. M., Lide, D. R., & Bruno, T. J., 2016-2017, 97th Edition / Boca Raton, Florida: CRC Press.
b Obtained from the plot of pHint vs pHbulk (Figure 2a).
c Obtained from the plot of zeta potential vs pHbulk (Figure 2b).
d Calculated using %C and %N (for amine functional groups) from elemental analysis.

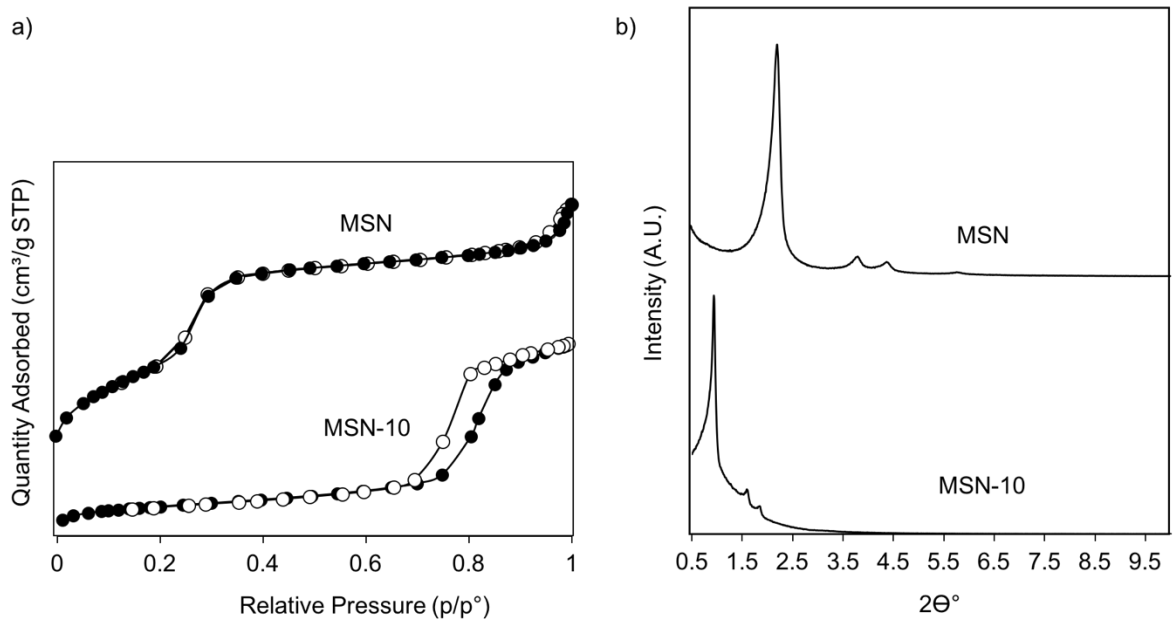

Figure S1. a) Nitrogen sorption isotherms and b) XRD patterns of parent MSN and MSN-10 samples.

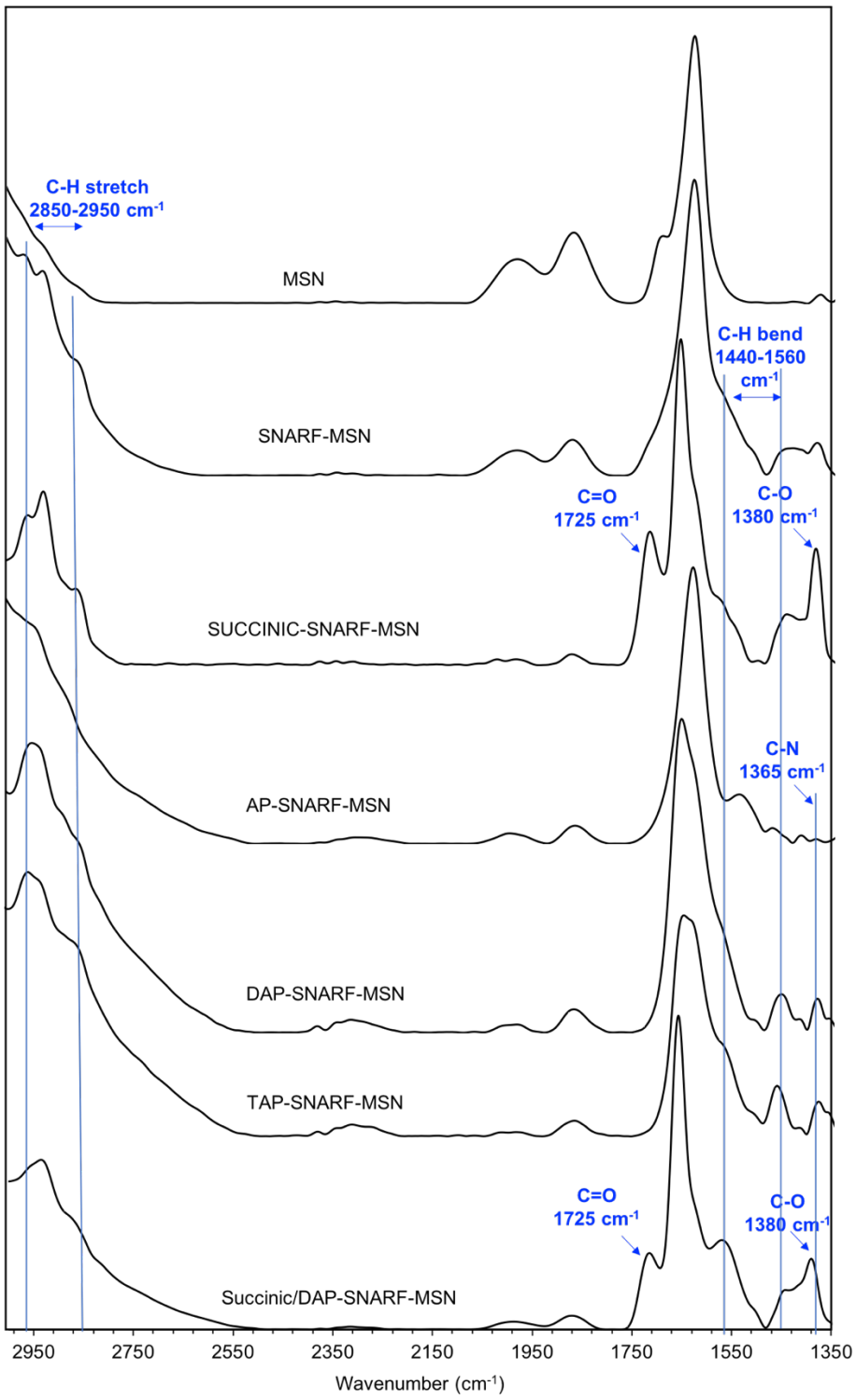

Figure S2. DRIFT spectra of functionalized-SNARF-MSN.

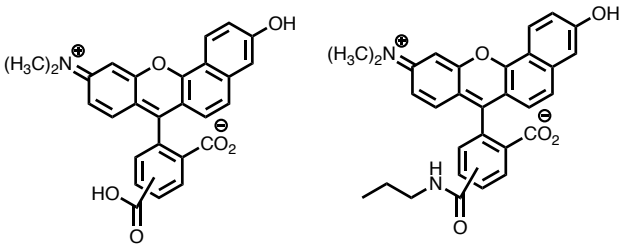

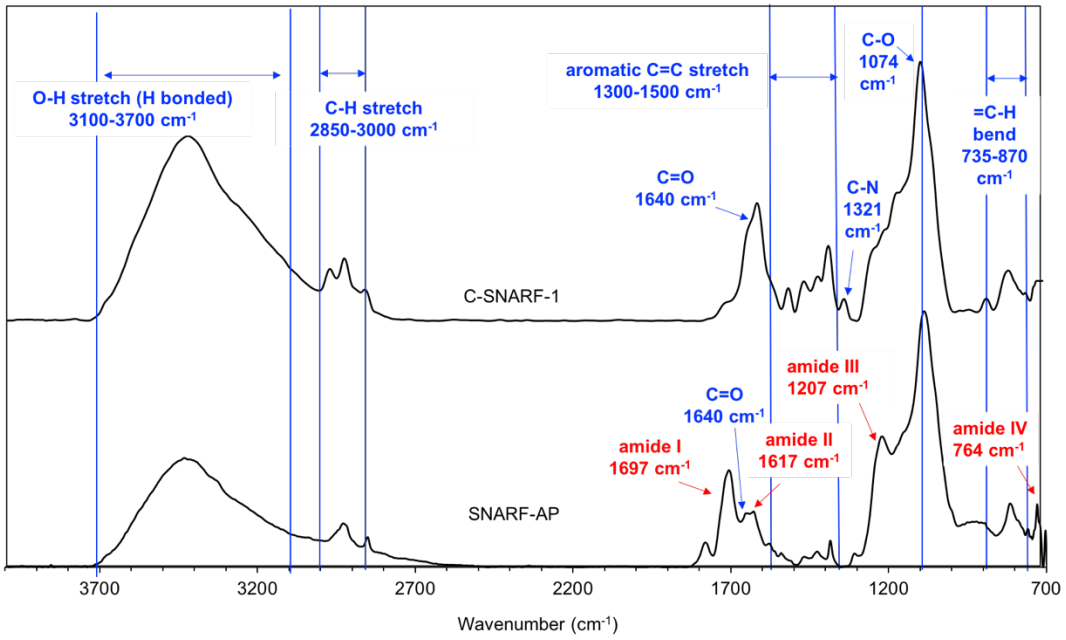

Figure S3. Structures and DRIFT spectra of C-SNARF-1 and SNARF-AP.

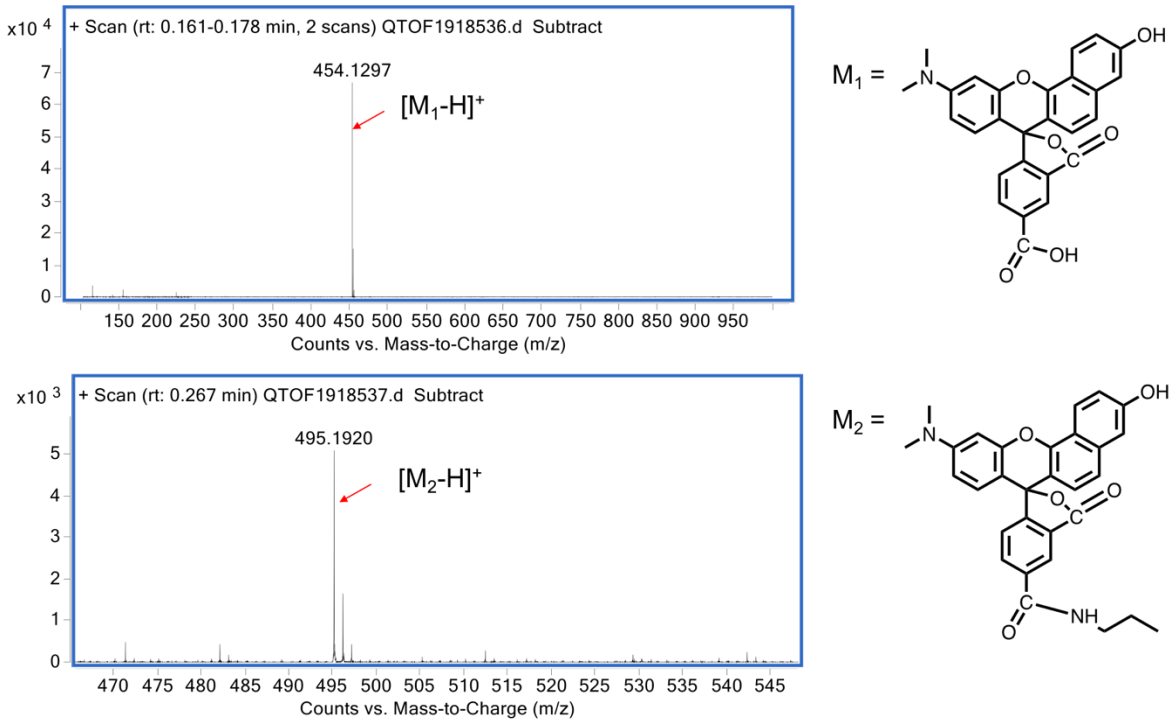

Figure S4. Mass spectra of C-SNARF-1 and SNARF-AP.

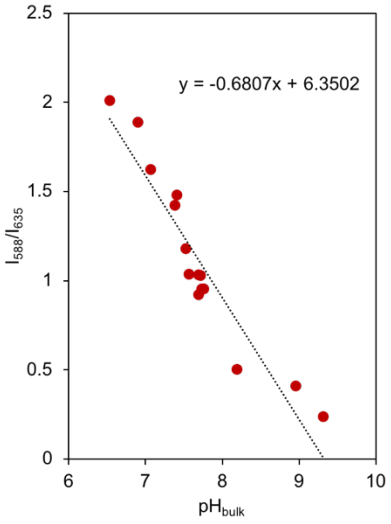

Figure S5. Calibration plot of SNARF-AP response to pH.

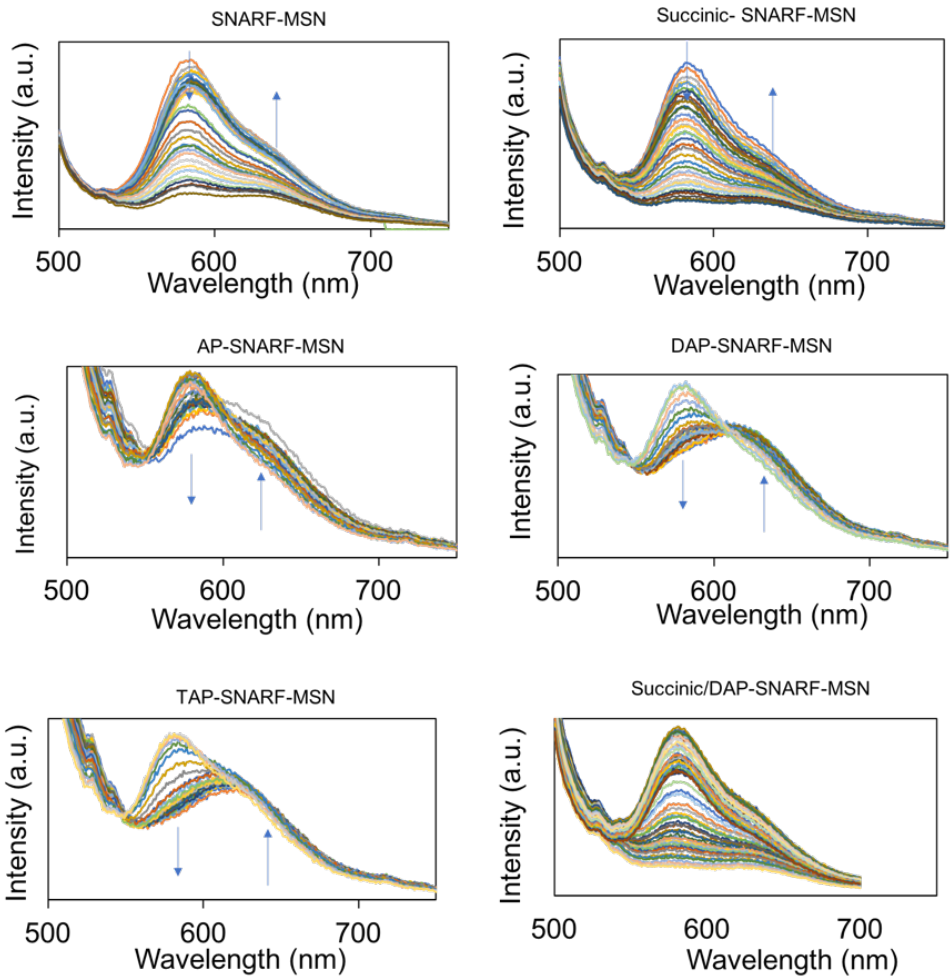

Figure S6. Fluorescence spectra of different functionalized SNARF-MSN.

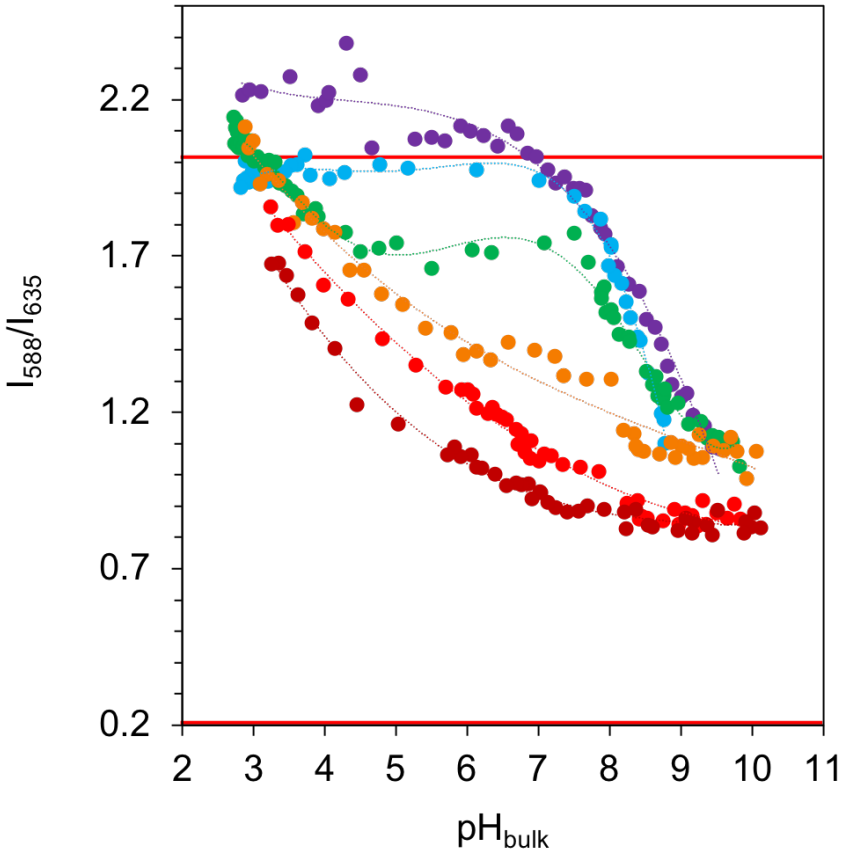

Figure S7. The plot of I_{588}/I_{635} versus pH_{bulk} for different MSN samples. TAP-SNARF-MSN (burgundy), DAP-SNARF-MSN (red), AP-SNARF-MSN (orange), SA/DAP-SNARF-MSN (green), SNARF-MSN (blue), SA-SNARF-MSN (purple). Dotted lines are only visual aids.

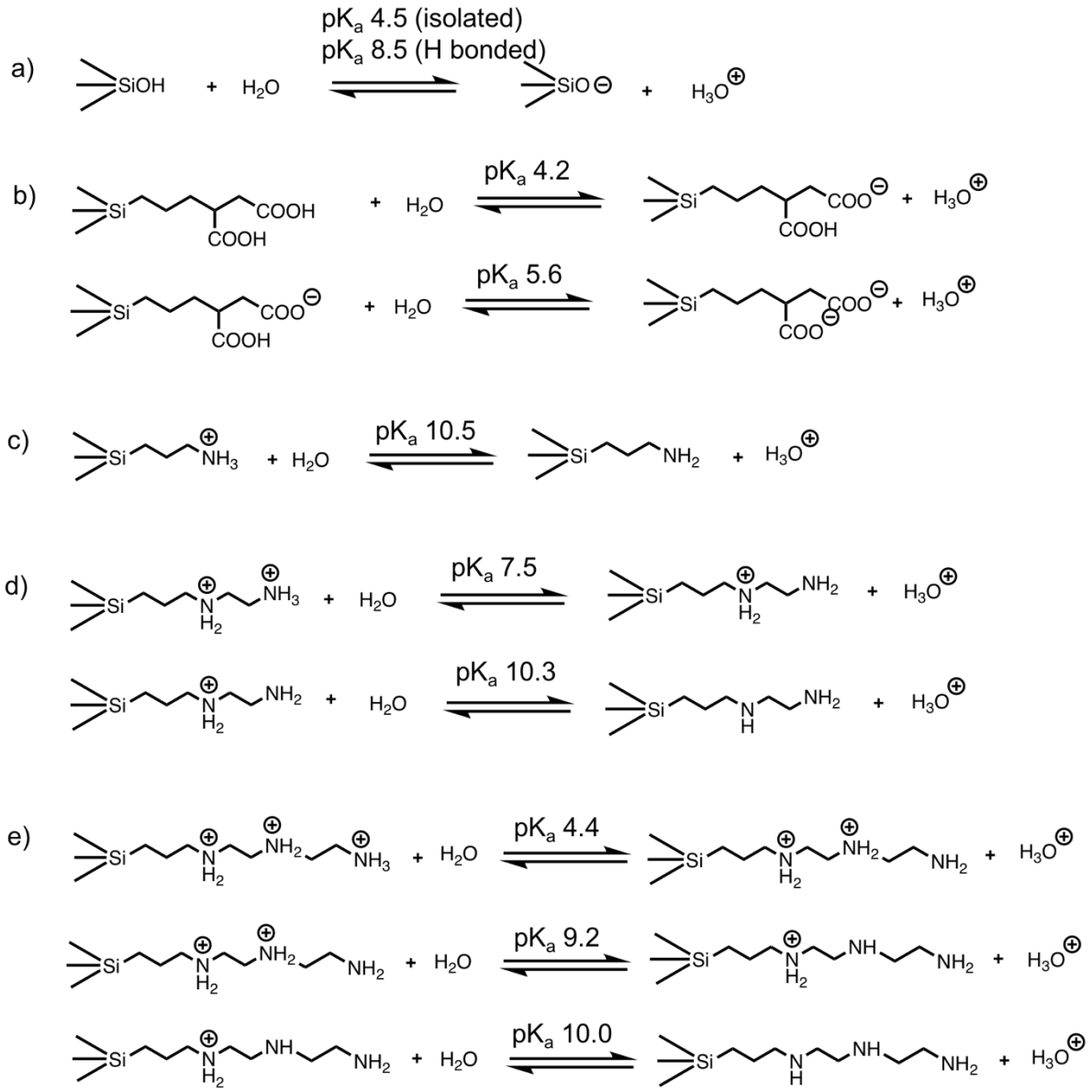

Figure S8. Different acid-base equilibria on functionalized MSN surfaces.

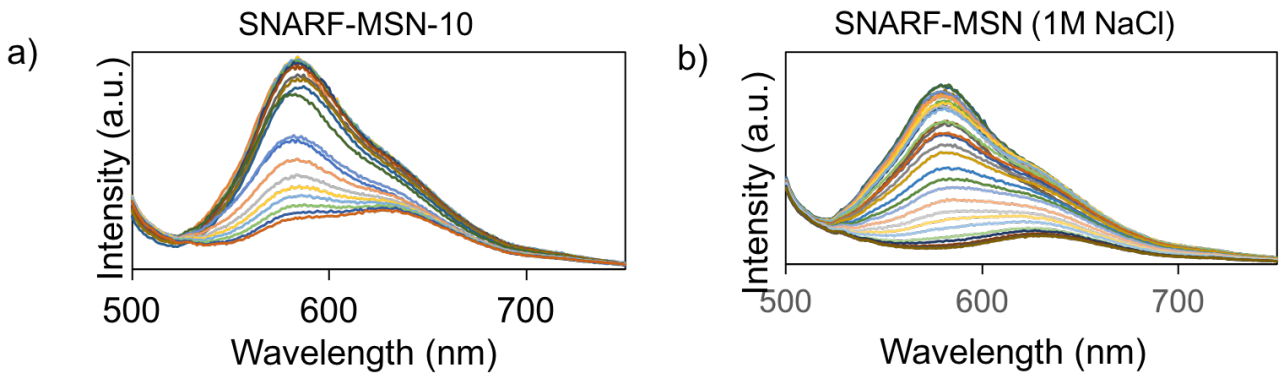

Figure S9. Fluorescence spectra of SNARF-MSN-10 in water and SNARF-MSN in 1M NaCl.

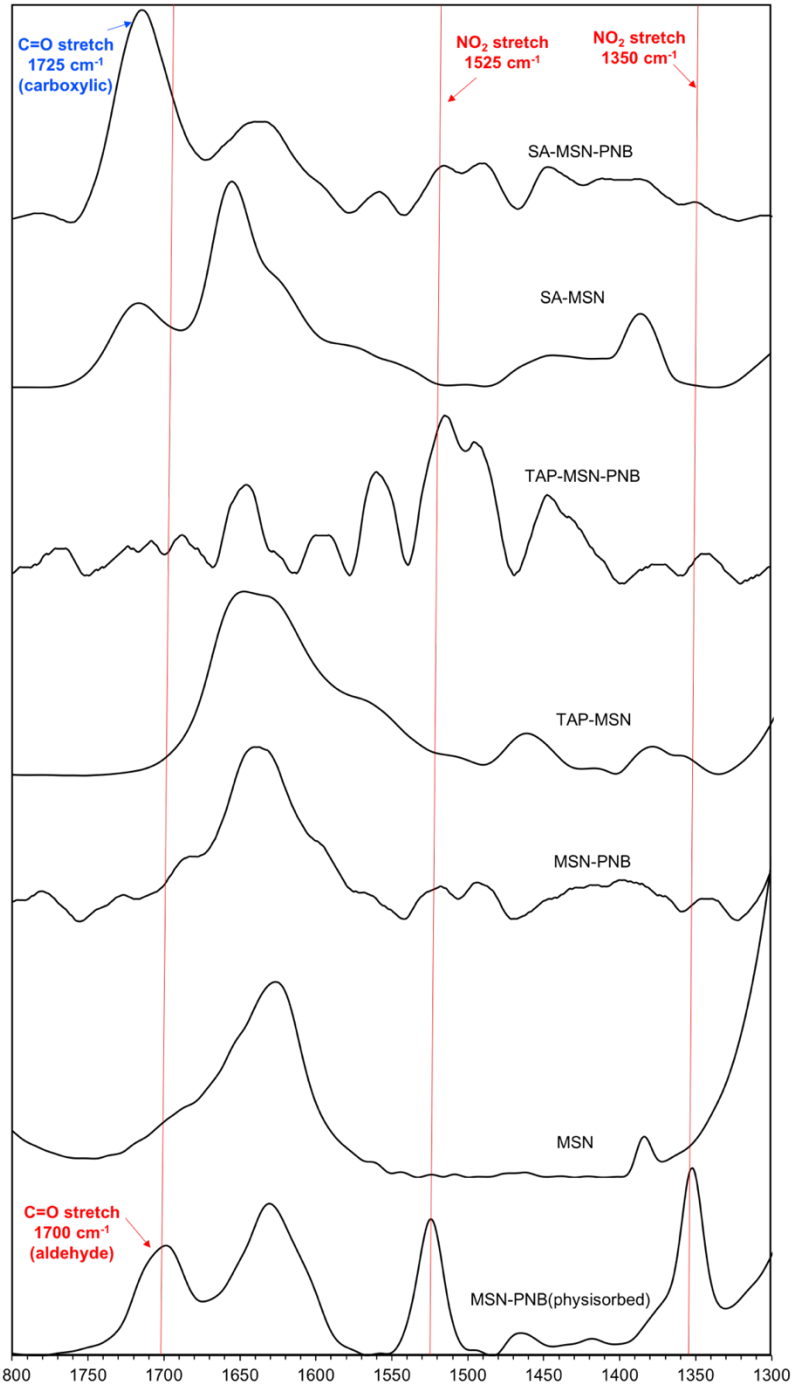

Figure S10. DRIFT spectra of functionalized MSN-PNB.

References

1. Singappuli-Arachchige, D.; Manzano, J. S.; Sherman, L. M.; Slowing, I. I., Polarity Control at Interfaces: Quantifying Pseudo-solvent Effects in Nano-confined Systems. *ChemPhysChem* **2016,** *17* (19), 2982-2986.

2. Singappuli-Arachchige, D.; Kobayashi, T.; Wang, Z.; Burkhow, S. J.; Smith, E. A.; Pruski, M.; Slowing, I. I., Interfacial Control of Catalytic Activity in the Aldol Condensation: Combining the Effects of Hydrophobic Environments and Water. *ACS Catalysis* **2019**.

3. Sebastián Manzano, J.; Singappuli-Arachchige, D.; Parikh, B. L.; Slowing, I. I., Fine-tuning the release of molecular guests from mesoporous silicas by controlling the orientation and mobility of surface phenyl substituents. *Chem. Eng. J.* **2017**.

4. Wang, W.; Park, R. Y.; Meyer, D. H.; Travesset, A.; Vaknin, D., Ionic Specificity in pH Regulated Charged Interfaces: Fe3+versus La3+. *Langmuir* **2011,** *27* (19), 11917-11924.

5. Venn, A. A.; Tambutté, E.; Holcomb, M.; Laurent, J.; Allemand, D.; Tambutté, S., Impact of seawater acidification on pH at the tissue-skeleton interface and calcification in reef corals. *Proc. Natl. Acad. Sci. U. S. A.* **2013,** *110* (5), 1634-1639.

6. Fattakhova-Rohlfing, D.; Wark, M.; Rathouský, J., Ion-Permselective pH-Switchable Mesoporous Silica Thin Layers. *Chem. Mater.* **2007,** *19* (7), 1640-1647.

7. Fujita, S.; Koiwai, A.; Kawasumi, M.; Inagaki, S., Enhancement of Proton Transport by High Densification of Sulfonic Acid Groups in Highly Ordered Mesoporous Silica. *Chem. Mater.* **2013,** *25* (9), 1584-1591.

8. Rosenholm, J. M.; Czuryszkiewicz, T.; Kleitz, F.; Rosenholm, J. B.; Lindén, M., On the Nature of the Brønsted Acidic Groups on Native and Functionalized Mesoporous Siliceous SBA-15 as Studied by Benzylamine Adsorption from Solution. *Langmuir* **2007,** *23* (8), 4315-4323.

9. Gao, Q.; Xu, W.; Xu, Y.; Wu, D.; Sun, Y.; Deng, F.; Shen, W., Amino Acid Adsorption on Mesoporous Materials: Influence of Types of Amino Acids, Modification of Mesoporous Materials, and Solution Conditions. *J. Phys. Chem. B* **2008,** *112* (7), 2261-2267.

10. Kovaleva, E. G.; Molochnikov, L. S.; Antonov, D. O.; Tambasova Stepanova, D. P.; Hartmann, M.; Tsmokalyuk, A. N.; Marek, A.; Smirnov, A. I., Proton Activity in Nanochannels Revealed by Electron Paramagnetic Resonance of Ionizable Nitroxides: A Test of the Poisson–Boltzmann Double Layer Theory. *J. Phys. Chem. C* **2018,** *122* (35), 20527-20538.

11. Yamaguchi, A.; Namekawa, M.; Kamijo, T.; Itoh, T.; Teramae, N., Acid−Base Equilibria inside Amine-Functionalized Mesoporous Silica. *Anal. Chem.* **2011,** *83* (8), 2939-2946.

12. Thörn, C.; Carlsson, N.; Gustafsson, H.; Holmberg, K.; Åkerman, B.; Olsson, L., A method to measure pH inside mesoporous particles using protein-bound SNARF1 fluorescent probe. *Microporous Mesoporous Mater.* **2013,** *165*, 240-246.

13. Shenderovich, I. G.; Buntkowsky, G.; Schreiber, A.; Gedat, E.; Sharif, S.; Albrecht, J.; Golubev, N. S.; Findenegg, G. H.; Limbach, H.-H., Pyridine-15N A Mobile NMR Sensor for Surface Acidity and Surface Defects of Mesoporous Silica. *J. Phys. Chem. B* **2003,** *107* (43), 11924-11939.

14. Ong, S.; Zhao, X.; Eisenthal, K. B., Polarization of water molecules at a charged interface: second harmonic studies of the silica/water interface. *Chem. Phys. Lett.* **1992,** *191* (3,Äì4), 327-335.

15. Dong, Y.; Pappu, S. V.; Xu, Z., Detection of Local Density Distribution of Isolated Silanol Groups on Planar Silica Surfaces Using Nonlinear Optical Molecular Probes. *Anal. Chem.* **1998,** *70* (22), 4730-4735.

16. Lorenz, C. D.; Crozier, P. S.; Anderson, J. A.; Travesset, A., Molecular Dynamics of Ionic Transport and Electrokinetic Effects in Realistic Silica Channels. *J. Phys. Chem. C* **2008,** *112* (27), 10222-10232.

17. Leung, K.; Nielsen, I. M. B.; Criscenti, L. J., Elucidating the Bimodal Acid−Base Behavior of the Water−Silica Interface from First Principles. *J. Am. Chem. Soc.* **2009,** *131* (51), 18358-18365.

18. O'Reilly, J. P.; Butts, C. P.; I'Anso, I. A.; Shaw, A. M., Interfacial pH at an Isolated Silica−Water Surface. *J. Am. Chem. Soc.* **2005,** *127* (6), 1632-1633.

19. Noller, C. R.; White, W. R., The Composition of Grignard Reagents as Determined by Precipitation with Dioxane. *Journal of the American Chemical Society* **1937,** *59* (7), 1354-1356.

20. Chen, Y.-C.; Ostafin, A.; Mizukami, H., Synthesis and characterization of pH sensitive carboxySNARF-1 nanoreactors. *Nanotechnol.* **2010,** *21* (21), 215503.

21. Suchkova, G. G.; Maklakov, L. I., Amide bands in the IR spectra of urethanes. *Vibrational Spectroscopy* **2009,** *51* (2), 333-339.

22. Trébosc, J.; Wiench, J. W.; Huh, S.; Lin, V. S. Y.; Pruski, M., Solid-State NMR Study of MCM-41-type Mesoporous Silica Nanoparticles. *Journal of the American Chemical Society* **2005,** *127* (9), 3057-3068.

23. Kohonen, M. M.; Karaman, M. E.; Pashley, R. M., Debye Length in Multivalent Electrolyte Solutions. *Langmuir* **2000,** *16* (13), 5749-5753.

24. Xiao, X.-D.; Vogel, V.; Shen, Y. R., Probing the proton excess at interfaces by second harmonic generation. *Chem. Phys. Lett.* **1989,** *163* (6), 555-559.

25. De Stefano, C.; Giuffrè, O.; Sammartano, S., Protonation Constants of Ethylenediamine, Diethylenetriamine, and Spermine in NaCl(aq), NaI(aq), (CH3)4NCl(aq), and (C2H5)4NI(aq) at Different Ionic Strengths and t = 25 °C. *Journal of Chemical & Engineering Data* **2005,** *50* (6), 1917-1923.

26. Anderson, E.; Fife, T. H., Carboxyl group participation in acetal hydrolysis. Hydrolysis of disalicyl acetals. *Journal of the American Chemical Society* **1973,** *95* (19), 6437-6441.

CHAPTER 6. GENERAL CONCLUSIONS

This dissertation demonstrated the feasibility of functionalizing MSN surfaces to control specific properties of the silica-water interface. Surface functionalization created local environments inside silica pores that differ from the bulk medium. Solvatochromic probes were used to measure the local polarity at the silica-water interface. Initially, it was shown that the interfacial dielectric properties could be precisely controlled by the nature and density of organic groups on the silica surface and their interactions with water. For instance, the interfacial polarity was proportional to the dipole moment of surface groups at a fixed loading. In addition, combining groups with different dipole moments gave interfacial polarity values that were an average of the monofunctional materials. The correlation between surface functionalization and interfacial polarity enables designing surfaces with target dielectric properties to control chemical processes at interfaces. For example, pore polarity tuning is a useful tool for the rational design of advanced materials in catalysis and drug delivery.

This dissertation outlined the effect of interfacial polarity on catalyzing important chemical reactions (e.g. aerobic oxidation of furfuryl alcohol, aldol condensation, Henry reaction, vinylogous aldol reaction). A large number of reactions need organic solvents that have significant undesired effects on health and environment. Controlling interfacial polarity via surface functionalization creates local environments within mesopores that mimic organic solvents. Therefore, the organic reactions can be driven inside the pores, while having water as the bulk reaction medium. For example, we demonstrated that the yield of furfural from aerobic oxidation of furfuryl alcohol increased with decreasing interfacial polarity. This was due to the stabilization of the transition state of the rate determining step in low dielectric media compared to polar media. The reaction yields were controlled by tuning the interfacial polarity while

performing the reaction in bulk water. This strategy can potentially be used in industry to drive organic reactions in water which is an economical and an environmentally friendly solvent.

In addition to controlling local dielectric properties, this thesis outlined the design of an enzyme-like heterogeneous system to regulate the access of solvent molecules to the active sites for assisting a catalytic conversion. C-C bond forming reactions such as the aldol condensation catalyzed by aminopropyl-modified MSN need low polar media to avoid the deactivation of surface amine groups via ion pair formation with surface silanols. However, the reaction also needs water to hydrolyze inhibitory imines that are formed on the surface. These inhibitory species limit the availability of catalytic amine groups. Therefore, the reaction can be executed in either hexane or water. The enzyme-like system that we designed optimizes the performance of the catalyst by including both: a low polarity local environment and accessibility to water. We tuned the local dielectric environment around the amine groups via hexyl modification of the MSN surface, and performed the reaction in water to enable hydrolysis of imine species. Importantly, in our system low dielectric media and water can be combined at the silica-water interface to enhance the performance of a heterogeneous catalyst, which is not possible in a homogeneous catalytic system. This strategy can be utilized to design catalytic surfaces with desired properties for different reactions.

This dissertation also demonstrated that non covalent interactions at the silica-water interface can be controlled by adjusting the orientation and mobility of surface groups. We controlled the desorption of ibuprofen molecules from silica pores by modifying the silica surface with different phenyl-containing species. We used rigid upright phenyl groups, phenyl rings attached to surface via mobile ethylene linkers and phenyl groups co-planar to the surface. The ibuprofen release was monitored using a home-made setup consisting of a dialysis bag with

drug loaded materials immersed in simulated body fluid and a quartz flow cuvette to circulate the solution. The resulting release profiles were studied using an adsorption-diffusion model. Kinetic and thermodynamic parameters that describe the differences between aromatic guest-surface interactions in the materials were extracted from the model. Ibuprofen released faster from non-functionalized MSN than all phenyl bearing materials. The materials with conformationally locked surface groups (rigid phenyl groups and coplanar phenyl groups) showed stronger interactions with the guest moelcules evidenced by negative ΔG of adsorption. The materials with conformationally flexible phenyl groups attached via mobile ethylene linkers and bare MSN showed comparatively weeker interactions as evidenced by positive ΔG of adsorption. The system was further studied using DFT calculations. The differences in the strength of adsorption of guest molecules to the surface were attributed to variations in the efficiency of π-π stacking interactions between aromatic rings of guest molecule and the surface groups. The type and geometry of the interactions controlled the adsorption and desorption behavior of guest molecules within silica pores. Carefully tuning the extent of guest-surface interactions allows designing drug delivery systems for potential therapeutic applications.

Finally, functionalizing the silica surface with acid/base groups of different pK_a allowed tuning the pH at the solid-liquid interface. Being able to control the interfacial pH is important to study phenomena that involve proton transfer. A pH sensitive fluorescent probe grafted on the MSN surface allowed measuring interfacial pH values and proved that the interfacial pH was different from the measured bulk pH. We showed that the interfacial pH was controlled by protonation/deprotonation equilibria of surface functional groups and by electrostatic interactions on the MSN surface. We further showed that increasing ionic strength or pore widths of the materials can lead to lower proton activity at the interface. In addition, we demonstrated that by

decreasing local acidity, we could protect an acetal bound to the MSN surface from being hydrolyzed.

In summary, the outlined work demonstrated that it is possible to use surface functionalization to produce local environments inside silica pores that are different than the bulk solvent. Being able to tune the properties of those local environments is important for potential applications of these materials in advanced catalytic and drug delivery systems.